UNIVERSITY OF CRETE
SCHOOL OF MEDICINE
GRADUATE PROGRAMME IN NEUROSCIENCES
POIRAZI LAB

DIPLOMA THESIS

Computational modeling of the trisynaptic circuit DG/CA3/CA1

CHATZISAVVAS ALEXANDROS

Diploma Thesis Supervisor: PANAYIOTA POIRAZI

HERAKLION
2022

Examination Committee

Poirazi Panayiota

Research Director

Charalampopoulos Ioannis

Assistant Professor

Venihaki Maria

Associate Professor

Acknowledgments

First of all, I would like to thank my supervisor, Dr. Panayiota Poirazi, for her patience and the trust she showed to me during the whole time of my presence in the lab. She passed on me her knowledge, and with her guidance, she helped me to overcome any obstacles and become a better scientist, but most of all, a better person. I also want to show my gratitude to the other members of the lab for making the atmosphere friendly and warm, and for their precious help when I was needing it.

Especially, I want to thank Dr. Kiriaki Thermos for always being available to hear my concerns and advise me properly. Finally, there are not enough words to thank my family and friends for their support during all these years of my journey.

This work was supported by the NIH grant No 1R01MH124867-01 “Experimental and modeling investigations into microcircuit, cellular and subcellular determinants of hippocampal ensemble recruitment to contextual representations” (PIs: Losonczy and Poirazi).

CURRICULUM VITAE

Alexandros Chatzisavvas

Personal Information

Nationality:	Greek
Date/Place of Birth:	30/11/1995, Ptolemaida, Greece
Military obligations:	Fulfilled
E-mail:	achatzisavvas@yahoo.com

Education

2019-present **M.Sc in Neuroscience**, School of Medicine, University of Crete, Heraklion, Greece

2013-2017 **B.Sc in Molecular Biology and Genetics Department**, Health Sciences School, Democritus University of Thrace, Alexandroupolis, Greece
Grade: 7.45/10.0
Diploma Thesis: ***'Transition state identification via Q-T diagrams: application to the CLN025 peptide'***

2010-2013 **Secondary Education**, General High School of Ptolemaida, Kozani, Greece
Grade: 17.4/20.0

Research Experience & Employment History

2021-present **Master Thesis in Poirazi lab**, Institute of Molecular Biology & Biotechnology (IMBB), Foundation of Research and Technology-Hellas (FORTH), Greece
Title: ***'Computational modeling of the hippocampal DG/CA1/CA2/CA3 circuits'***

2020 **Lab Rotation in Poirazi lab**, Institute of Molecular Biology & Biotechnology (IMBB), Foundation of Research and Technology-Hellas (FORTH), Greece
Title: ***'Computational modeling of hippocampal circuits'***
Grade: 10/10, **Supervisor: Panayiota Poirazi**

2020 **Lab Rotation in Clinical Chemistry lab**, School of Medicine University of Crete, Greece
Title: ***'Study of the effect of neurosteroids on inflammatory pain and obesity'***
Grade: 9.8/10, **Supervisor: Maria Venihaki**

2020	**Project award contract at the University of Western Macedonia**, Greece *Title: **'Carrying out scientific examinations of laboratory diagnosis and confirmation as well as laboratory surveillance of cases of infection by the new coronavirus COVID-19 (SARS-CoV-2)'***
2018-2019	**Corporal (OR-4) of Military Police,** Special Units of Hellenic Army, Hellenic Army, Greece *I was chosen to serve in the military police unit, where I was trained on Military Police school, graduated successfully, and was responsible to a group of eighteen people.* *- I was chosen to serve as honorary personal driver and guard of the Brigadier.*
2016	**Internship in Structural and Computational Biology lab,** Department of Molecular Biology and Genetics, Democritus University of Thrace, Greece **Supervisor: Nicholas M. Glykos**.

Seminars and Workshops

2021	Online Summer School of NMA-Computational Neuroscience
2021	32nd National Conference of the Hellenic Neurological Society, Thessaloniki, Greece
2021	Federation of European Neuroscience Societies (FENS) Committee for Higher Education and Training (CHET) Webinar "Brain Development and Neuropsychiatric Disorders"
2019	Hellenic Bioinformatics Conference "Precision Medicine, Biodiversity & Genomic Biology", Foundation of Research and Technology-Hellas (FORTH), Heraklion, Greece
2019	28th Conference of Hellenic Society for Neuroscience, Foundation of Research and Technology-Hellas (FORTH) Heraklion, Greece
2017	68th National Conference of the Hellenic Biochemistry and Molecular Biology Society, Athens, Greece

2016	Scientific Event by Histology-Embryology's lab of Democritus University of Thrace, Alexandroupoli, Greece
2016	Software skills training run jointly by Software Carpentry and Aristotle University of Thessaloniki, Thessaloniki, Greece
2016	Symposium of the Obstetrics University and Gynecology Clinic of the Democritus University of Thrace and the Hellenic Society of Ultrasound in Obstetrics and Gynecology on "Perinatal Infections", Alexandroupoli, Greece
2015	"Identifying genes for complex disorders: Population Genetic Structure, Genomewide Association Studies, and Pathway Analysis", Department of Molecular Biology and Genetics, Educational Workshop, Democritus University of Thrace, Alexandroupoli, Greece

Awards/ Scholarships

2009-2010	1st place at the School Chess Championship (Secondary school) Northwest Macedonia and qualification in the 8th Panhellenic School Championship (Secondary school)

Language Skills

Greek: Native Speaker **English:** B2 (University of Michigan)

IT Skills

Programming Languages: Python, Perl, C, R
Bioinformatics tools: PLINK, EIGENSOFT, DAVID, PANTHER, TOPPGENE

Laboratory skills & techniques

Mouse handling:	Basic techniques for handling and reproduction of wild-type and mutant mice
Cell culture techniques:	Handling (Isolation, passage, plating, etc) of primary human adipocytes and mice macrophages
Molecular techniques:	RNA isolation, cDNA synthesis, and real-time qPCR from tissue and cell samples, protein isolation, purification, quantification, and western blot analysis, ELIZA immunoassay

Pathogen related techniques: Bacterial cultures (for bacteria propagation), determination of bacterial load

Driving Licence

06/2018-06/2033	European driving license holder, Category B
01/2019	Driving Licence for military vehicles, Category B

Interests

Hiking, Trailing, Biking, Sightseeing, Playing Chess

ABSTRACT

The Hippocampus plays a key role in numerous brain processes such as episodic memory formation and recall, and spatial navigation. Multiple streams of previously unrelated information converge to the hippocampal circuits where important mnemonic functions such as pattern separation and pattern completion take place. Some of the primary hippocampal areas include the DG, CA3, and CA1, which comprise the so-called trisynaptic pathway, a closed processing loop with bidirectional connections with higher cortical areas. Computational modeling has been extensively utilized to understand how hippocampal network dynamics are linked to behavior since such studies often require experiments that are restricted by technical limitations. However, most currently available Hippocampus models are often overly simplistic, ignoring key neuronal and network properties. Importantly, they overlook the implications of active dendritic mechanisms to network-level functions. For this reason, we developed a simplified yet biologically plausible network model of the trisynaptic pathway, which was extensively validated against experimental data. Our network model accurately reproduces many essential cellular and network functions, along with their contribution to pattern separation and pattern completion. To our knowledge, this is the first hippocampal model of the complete trisynaptic pathway that also incorporates active dendritic properties and highly sophisticated connectivity. Hence, our model offers a flexible experimentation platform for exploring how single-cell properties, such as dendritic computations and plasticity, or neuronal network properties like inhibition and network connectivity affect hippocampal dynamics and well-known memory processes.

Keywords: Computational Modeling; CA1; CA3; Dendrites; Dendritic spikes; Dentate Gyrus; Hippocampus; Interneurons; Pattern Completion; Pattern Separation; Principal cells

ΠΕΡΙΛΗΨΗ

Ο ιππόκαμπος διαδραματίζει βασικό ρόλο σε πολλές εγκεφαλικές διεργασίες, όπως ο σχηματισμός και η ανάκληση της επεισοδιακής μνήμης και η χωρική πλοήγηση. Πολλαπλές ροές προηγουμένως ασύνδετων πληροφοριών συγκλίνουν στα κυκλώματα του ιππόκαμπου, όπου λαμβάνουν χώρα σημαντικές μνημονικές λειτουργίες όπως ο διαχωρισμός και η ολοκλήρωση μοτίβων. Ορισμένες από τις πρωταρχικές περιοχές του ιππόκαμπου περιλαμβάνουν την DG, την CA3 και την CA1, οι οποίες αποτελούν τη λεγόμενη τρισυναπτική οδό, έναν κλειστό βρόχο επεξεργασίας με αμφίδρομες συνδέσεις με ανώτερες περιοχές του φλοιού. Η υπολογιστική μοντελοποίηση έχει χρησιμοποιηθεί εκτενώς για την κατανόηση του τρόπου με τον οποίο η δυναμική του δικτύου του ιππόκαμπου συνδέεται με τη συμπεριφορά, δεδομένου ότι τέτοιες μελέτες απαιτούν συχνά πειράματα που περιορίζονται από τεχνικούς περιορισμούς. Ωστόσο, τα περισσότερα διαθέσιμα σημερινά μοντέλα ιππόκαμπου είναι συνήθως υπερβολικά απλουστευτικά, αγνοώντας βασικές νευρωνικές και δικτυακές ιδιότητες. Είναι σημαντικό ότι παραβλέπουν τις επιπτώσεις των ενεργών δενδριτικών μηχανισμών στις λειτουργίες σε επίπεδο δικτύου. Για το λόγο αυτό, αναπτύξαμε ένα απλουστευμένο αλλά βιολογικά σχετικό μοντέλο της τρισυναπτικής οδού, το οποίο επικυρώθηκε εκτενώς με πειραματικά δεδομένα. Το μοντέλο μας αναπαράγει με ακρίβεια πολλές βασικές κυτταρικές και σε επίπεδο δικτύου λειτουργίες, μαζί με τη συμβολή τους στον διαχωρισμό και την ολοκλήρωση των μοτίβων. Εξ όσων γνωρίζουμε, αυτό είναι το πρώτο μοντέλο ιππόκαμπου της πλήρους τρισυναπτικής οδού, που ενσωματώνει επίσης ενεργές δενδριτικές ιδιότητες και ιδιαίτερα εξελιγμένη συνδεσιμότητα. Ως εκ τούτου, το μοντέλο μας προσφέρει μια ευέλικτη πλατφόρμα πειραματισμού για τη διερεύνηση του τρόπου με τον οποίο οι ιδιότητες μεμονωμένων κυττάρων, όπως οι δενδριτικοί υπολογισμοί και η πλαστικότητα, ή οι ιδιότητες νευρωνικών δικτύων, όπως η αναστολή και η συνδεσιμότητα του δικτύου, επηρεάζουν τη δυναμική του ιππόκαμπου και τις γνωστές διαδικασίες μνήμης.

CONTENTS

ABBREVIATIONS

5-HT: 5-hydroxytryptamine

A/C: associative/commissural

AdEx: Adaptive Exponential

AMPARs: α-amino-3-hydroxy-5-methyl-4-isoxazolepropionic acid receptors

ANN: Artificial neural network

BCs: basket cells

BiC: Bistratified cell

CA1: cornu-ammonis 1

CA2: cornu-ammonis 2

CA3: cornu-ammonis 3

CA4: cornu-ammonis 4

CAdEx: Conductance Adaptive Exponential

CR: calretinin

DA: dopamine

DG: dentate gyrus

EC: entorhinal cortex

F-I curves: Frequency-Current curves

gcl: granule cell layer

GABARs: γ-aminobutyric acid receptos

GCs: granule cells

hBD: hilar basal dendrite

HD: Hamming distance

HIPP: hilar-perforant-path-associated

HPCC: high-performance computing cluster

iml: inner molecular layer

IS-INs: interneuron-specific interneurons

LEC: lateral entorhinal cortex

LTP: long-term potentiation

ml: molecular layer

mml: middle molecular layer

Machine learning: ml

Mamm: Supramammillary

MCs: mossy cells

MEC: medial entorhinal cortex

MF: Mossy Fibres

Mg^{2+}: magnesium ions

NA: noradrenaline

NMDARs: N-methyl-D-aspartate receptors

oml: outer molecular layer

OLM: oriens lacunosum moleculare cell

pcl: polymorphic cell layer

pcl: pyramidal cell layer

PP: Perforant Path

PV^{+}: parvalbumin-positive

s: sigmoidal function

sl-m: stratum lacunosum-moleculare

sl: stratum lucidum

so: stratum oriens

sr: stratum radiatum

SC: Schaffer Collaterals

SST^{+}: somatostatin-expressing

STDP: spike-timing-dependent plasticity

vCA3: ventral CA3

V-I curves: voltage-current curves

VIP: Vasoactive intestinal peptide/calretinin-expressing type 3 interneuron-specific cell

1. Introduction

1.1 Hippocampus

Historically, the intriguing case of patient H.M. and his anterograde amnesia after his bilateral temporal lobe resection (Scoville & Milner, 1957), the discovery of neurons encoding spatial position, the place cells (O'Keefe & Dostrovsky, 1971), and the activity-dependent long-term potentiation (LTP) of synapses (Bliss & Lomo, 1973) in the hippocampus have drawn the focus of many researchers. All these, along with its many functions, e.g., memory storage and recall, the presence of special features, such as adult neurogenesis, and its involvement in many diseases, like Alzheimer's, made the hippocampus *"a neural Rosetta Stone"* as Andersen et al. (2007) stated. It encodes knowledge of things, people, events, places, both spatial and non-spatial forms of explicit or declarative memory and time during episodic events (Basu & Siegelbaum, 2015). As for the memories, the hippocampus stores them independently of each other, applies old memories into new contexts, and retrieves them from a few cues (Yassa & Stark, 2011). These functions can be achieved through some computations such as pattern separation or pattern completion (Kowalski et al., 2016). All this attention from the scientific community has driven the enrichment of its anatomical, physiological, and functional data, allowing the modeling of this structure (Cutsuridis et al., 2010).

All mammals have a hippocampus, which is part of the hippocampal formation along with the entorhinal cortex (EC), subiculum, presubiculum, parasubiculum, and dentate gyrus (DG). It consists of two hippocampi, one in each hemisphere, it is located in the allocortex and is part of the limbic system (**fig. 1**). The hippocampi can be broken down into three sub-regions, cornu-ammonis 1 (CA1), CA2, and CA3. According to Lorente de Nó, it is supposed to be a fourth one, CA4 or hilus, but many consider it part of the DG (Andersen et al., 2007). As the information flows from DG to CA3 to CA1, scientists refer to the hippocampus as the trisynaptic circuit.

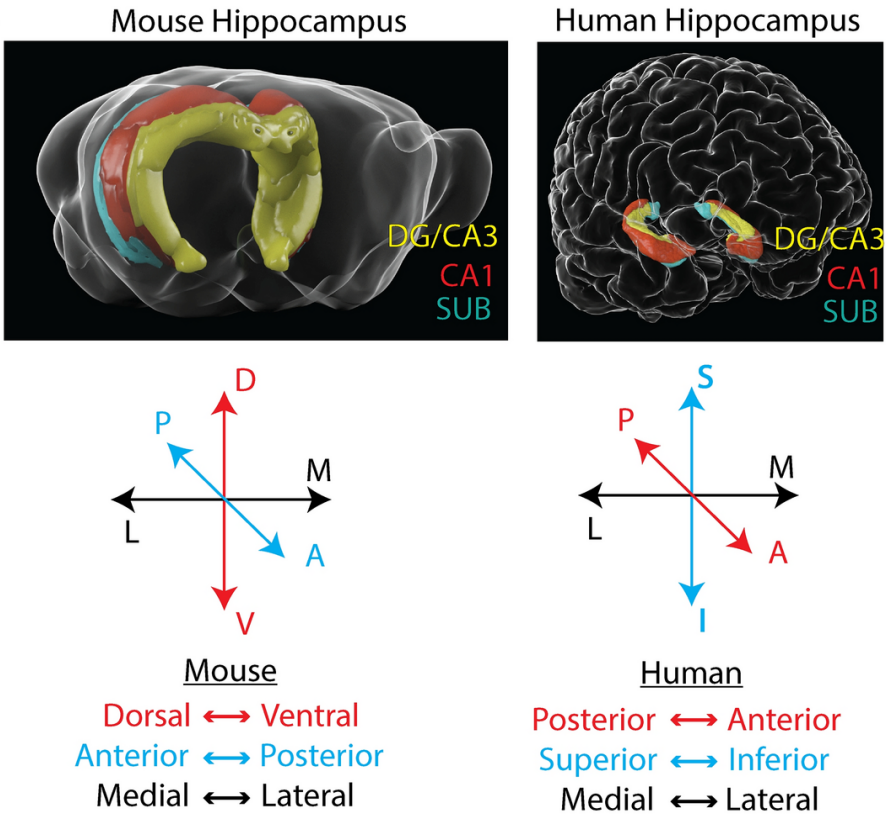

Figure 1. Three-dimensional representations of the mouse and human hippocampus showing the relative locations of the DG/CA3 (yellow), CA1 (red), and SUB (green). The longitudinal hippocampal axis (red in axes chart) in mice is oriented dorsoventrally, whereas the human longitudinal axis is rotated into the anterior-posterior axis. In addition, the anterior/posterior (septo-temporal; blue color) axis in mice is oriented in the superior-inferior direction in humans. (Adapted from Bienkowski et al., 2021)

The classical trisynaptic circuit consists of three consecutive projections, the projection from EC to DG via the Perforant Path (PP), the projection from DG to CA3 via the Mossy Fibres (MF), and the projection from CA3 to CA1 via the Schaffer Collaterals (SC) (**fig. 2**) (Andersen et al., 2007). Nowadays, the trisynaptic circuit is considered outdated and it has been updated with noncanonical connections, such as CA3 backprojection to DG, EC direct projection to CA1, and the interplay of Subiculum with the CA1 and EC (**fig. 3**) (Xu et al., 2016). The main aim of this research is to simulate the trisynaptic circuit using dendrites, and their active mechanisms, to get a grasp of their role on hippocampal processes. Another goal is to enrich it with up-to-date (noncanonical) connections, i.e., CA3-to-DG backprojection and direct EC-to-CA1 inputs.

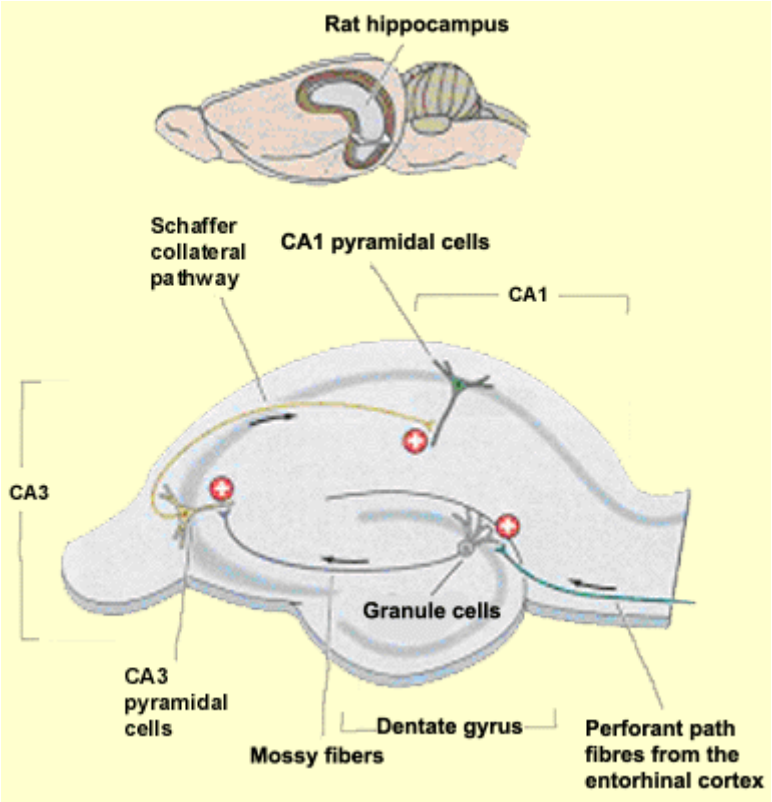

Figure 2. The Trisynaptic loop**.**

(Figure from https://thebrain.mcgill.ca/flash/a/a_07/a_07_cl/a_07_cl_tra/a_07_cl_tra.html)

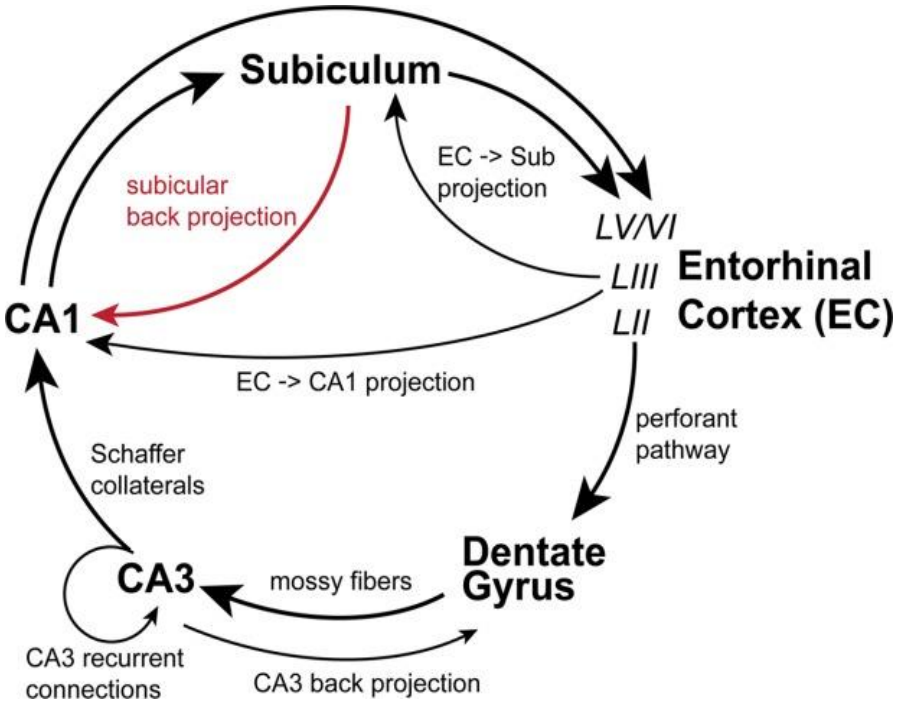

Figure 3. Canonical hippocampal circuitry and the noncanonical subicular-CA1 pathway. The diagram depicts the noncanonical and canonical circuitry of the hippocampal formation. Evidence herein describes noncanonical backprojections from the subiculum to CA1 (red

line). Feedforward and unidirectional canonical projections are depicted as black lines with large directional arrows. The trisynaptic circuit connections are made up of layer II (LII) EC projections to the DG via the PP, projections of the dentate GCs to area CA3 pyramidal neurons via mossy fibers, and CA3 projections to area CA1 pyramidal neurons via SC. CA1 transfers excitatory information out of the hippocampus proper via direct projections to deep layers (layers V and VI, LV/VI) of the EC or the subiculum. CA2 is described in the text but is not depicted in this diagram. Additional excitatory projections within the hippocampal formation include layer III (LIII) entorhinal neurons projections to CA1 and the subiculum (the temporoammonic pathway), and local recurrent collaterals of CA3 pyramidal cells onto other CA3 pyramidal cells. Also, the backprojection of CA3 pyramidal neurons to the DG has been described. (Figure from Xu et al., 2016)

1.2 Dentate gyrus

The DG includes two major types of neurons, the principal or glutamatergic neurons, and the interneurons. The principal neurons are the granule cells (GCs) and the mossy cells (MCs), whereas some of the best-studied interneurons are the basket cells (BCs) and the hilar-perforant-path-associated (HIPP) cells. The DG is divided into three layers, 1) the molecular layer (ml), 2) the granule cell layer (gcl), and 3) the polymorphic cell layer (pcl) or hilus. These layers contain, respectively, 1) the GC's dendrites and the fibers of the EC, 2) the bodies of the GCs and some interneurons, and 3) different types of neurons, like the MCs or the HIPP cells (Amaral et al., 2007). Furthermore, the ml is divided into three sub-layers, the outer molecular layer (oml), the middle molecular layer (mml), and the inner molecular layer (iml) (**fig. 4**) (Scharfman, 2016).

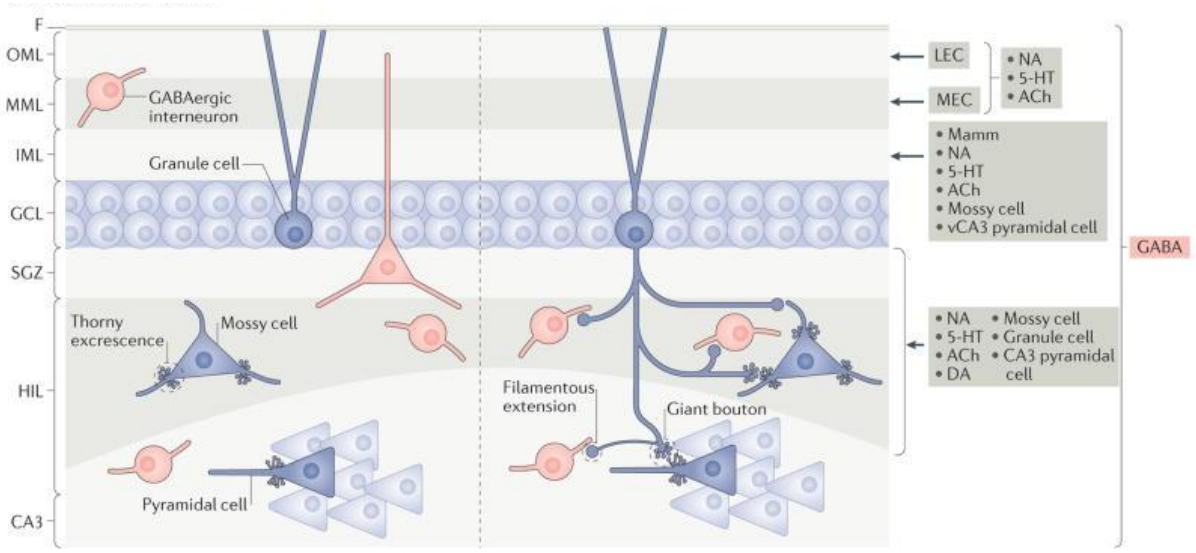

Figure 4. The layers of the DG are shown. The sources of major afferent inputs are shown on the right (red box indicates the GABAergic input and grey boxes indicate inputs from other neurotransmitters). GABAergic interneurons innervate all layers. The lateral entorhinal cortex (LEC) and the medial entorhinal cortex (MEC) innervate the outer oml and the middle mml, respectively. Supramammillary (Mamm), cholinergic, mossy cell and ventral CA3 (vCA3) pyramidal cell axons innervate the iml. The oml and mml also receive inputs from the brainstem (including noradrenergic and 5-hydroxytryptamine (5-HT; also known as serotonin) inputs) and from basal forebrain cholinergic neurons. The HIL receives diverse inputs, including the axons of GCs, DG GABAergic neurons, MCs, CA3 pyramidal cells, neuromodulatory inputs from the brainstem (such as noradrenaline (NA), 5-HT, and dopamine (DA)) and basal forebrain cholinergic neurons. The efferents from the DG to other areas arise mainly from GCs that project to the HIL and CA3. The granule cell axon, called a mossy fibre, is complex. It makes giant boutons that innervate thorny excrescences of MCs and pyramidal cells and small boutons that arise from hilar collaterals and filamentous extensions from the giant boutons, The small boutons primarily contact interneurons but also form contacts on distal dendrites of MCs. ACh, acetylcholine; F, fissure; SGZ, subgranular zone. (Adapted from Scharfman, 2016)

The DG is well known for its role in pattern separation and its adult neurogenesis ability. Due to its vast amount of GCs, it outnumbers the afferent populations, i.e., almost a ratio of 5 to 1 in comparison with the input neurons of the EC. Along with the low activity of the GCs, ~2 - 5 % of the total population, these findings suggest the sparse encoding and the orthogonalization of the information leading to pattern separation of closely related information (Christian et al., 2020; Mao et al., 2017). Adult neurogenesis has been observed in the olfactory bulb and the DG. In the DG, adult neurogenesis has been shown to help pattern separation by inhibiting the mature GCs and therefore improving the sparse encoding (Drew et al., 2016)

1.3 Cornu Ammonis 3 (CA3)

The CA3 region is located between the DG and the CA2/CA1 region. This region consists of two groups of cells, like the DG, the principal cells, and the inhibitory cells. This region is divided into four layers, with each layer having its unique properties. Firstly, the reference layer will be the pyramidal cell layer (pcl), and as the name indicates, it contains the somata of the principal cells, the pyramidal cells. Deeper exists the stratum oriens (so), a layer containing the basal dendrites of the pyramidal cells, efferents from the other pyramidal cells, and the bodies of many interneurons. Just above the pcl is a thin layer that contains the MF, the stratum lucidum (sl). The most superficial layer is the stratum lacunosum-moleculare (sl-m), which contains afferents from other regions, like the EC, the distal dendrites of the pyramidal cells, and the somata of some interneurons. Between the sl-m and the sl is the stratum radiatum (sr), which contains the oblique dendrites of the pyramidal cells and efferents from the other pyramidal cells (**fig. 5**) (Andersen et al., 2007).

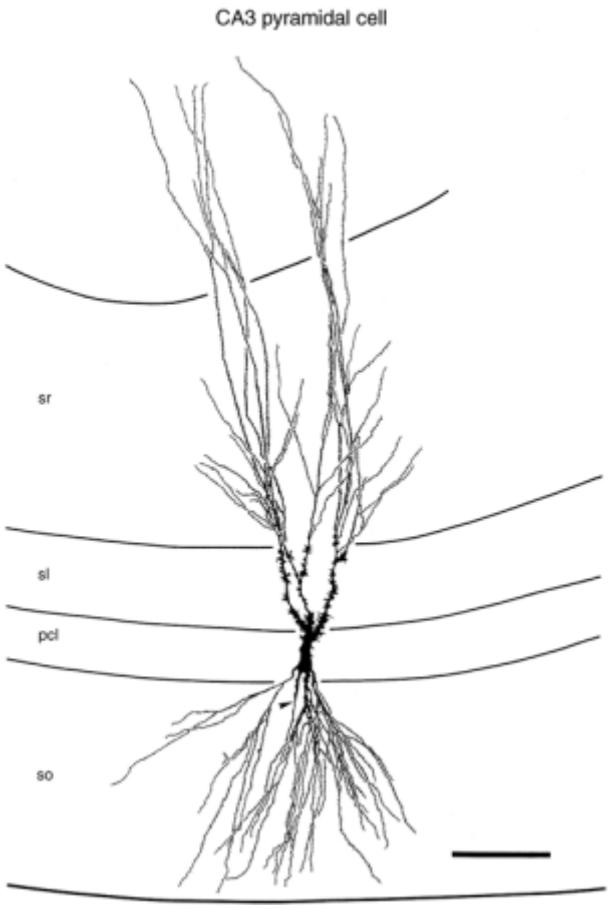

Figure 5. Camera lucida drawing of a CA3 pyramidal neuron located in the midportion of the field. As this neuron lies outside the zone of the infrapyramidal mossy fiber bundle, most of the thorny excrescences are located on the proximal apical dendrites. The axon of this neuron is indicated by an arrowhead. Bar 100 m. (Adapted from Ishizuka et al., 1995.)

There are electrophysiological data that prove the occurrence of pattern separation and pattern completion in CA3 (Rebola et al., 2017). Some theoretical models support the idea that the CA3 region exhibits the ability to perform pattern separation with the main explanation of the strong inputs from the DG, that already perform pattern separation. This idea, combined with the existence of the backprojections from the CA3 to the DG, could help explain episodic learning, but empirical data are needed to support this (Kassab & Alexandre, 2018). Lee et al. (2015) suggested a gradient along the proximal-distal axis from pattern separation in proximal CA3 to pattern completion in distal CA3, supporting the idea that CA3 is not a homogenous network with consistent properties.

One of the best-studied functions of the CA3 area is its involvement in memory storage through pattern completion. Pattern completion is the ability to recall a memory by observing only a part of the information that was present during the learning phase. The high number of recurrent synapses of the CA3 pyramidals provides a good template for the storage and retrieval of associative memories. A

schematic representation of the CA3 region's afferents and efferents, and their role, is shown in Figure 6.

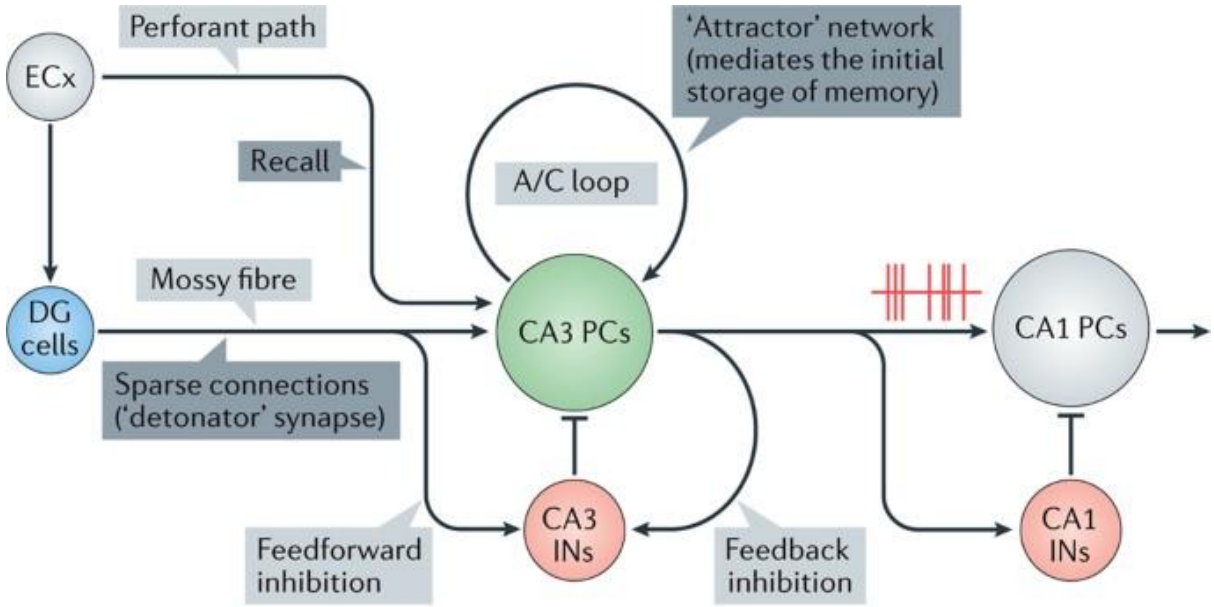

Figure 6. CA3 circuits and their proposed role in memory shows the different elements of CA3 circuits and their hypothesized involvement in memory encoding and recall. The extensive excitatory interconnections between CA3 pyramidal cells (PCs) — known as the associative/commissural (A/C) loop — are proposed to work as an attractor network, in which associative memories are stored and recalled through pattern completion. MF originating from the DG provide sparse and powerful excitatory connections (known as 'detonator' synapses) to CA3 PCs; these connections are proposed to assist in the encoding of new patterns of activity (representing new memories) in CA3 through pattern separation. The direct connections from the ECx to CA3 are thought to provide the cues for retrieval (recall) of information from CA3, especially when incomplete information is provided. Feedforward inhibition via CA3 interneurons (INs) strongly controls information transfer between DG and CA3 depending on the pattern of presynaptic activity and may be involved in the precision of memory. Inhibitory loops in CA3 control the generation of oscillatory activities and are amenable to substantial structural plasticity upon learning. Within the hippocampus, the main outputs from the CA3 region (illustrated by the red schematic trace) are the axons of CA3 PCs, which make contact with CA1 PCs and CA1 INs. (Figure from Rebola et al., 2017)

1.4 Cornu Ammonis 1 (CA1)

CA1 is the border of the hippocampus adjacent to the subiculum. This region has a similar cytoarchitecture to the CA3, but some neuron groups have different electrophysiological properties and morphology, e.g., the pyramidal cells (**fig. 7**). It consists of 1) the pcl, which contains the somata of the pyramidal cells, 2) the so, which contains the basal dendrites of the pyramidals, and the SC afferents, 3) the sr,

which contains the oblique dendrites of the pyramidals and SC afferents, and lastly 4) the sl-m, which contains the distal dendrites of the pyramidals and EC afferents (Andersen et al., 2007).

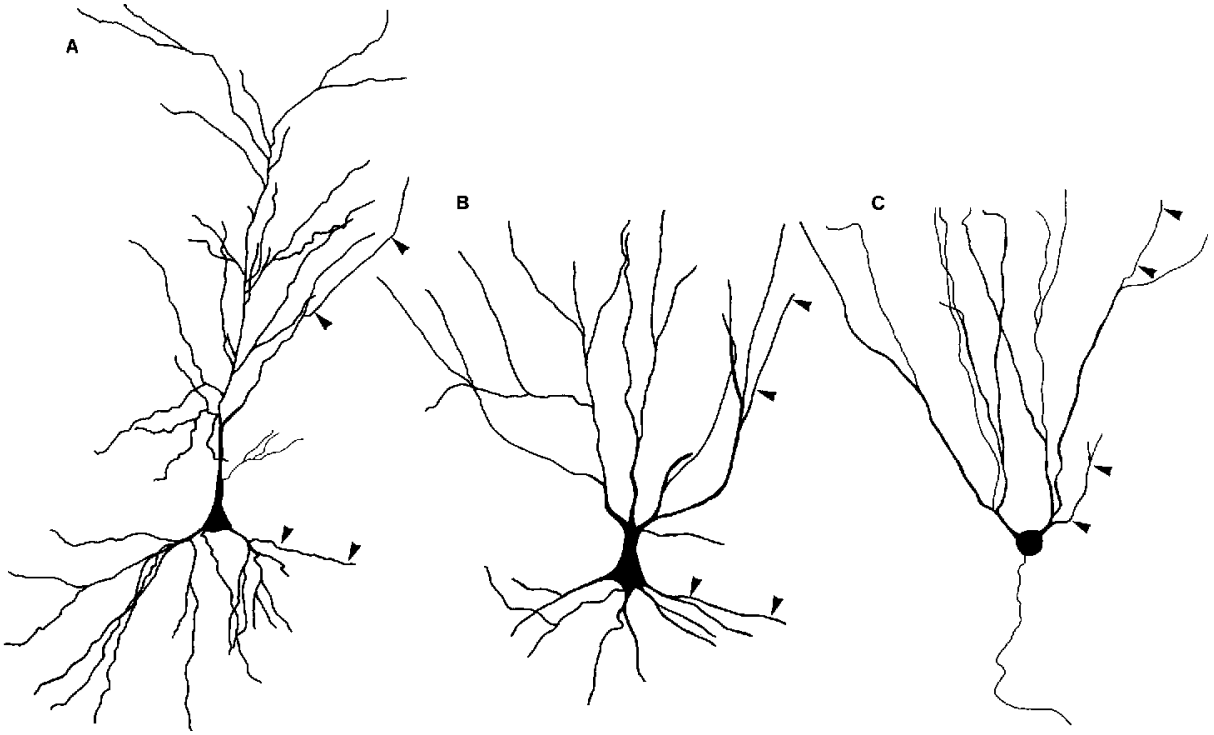

Figure 7. Camera lucida tracings (x 1250) of a representative CA1 pyramidal cell (A), CA3 pyramidal cell (B), and DG granule cell (C). (Adapted from Gould et al., 1990)

Sending excitatory and inhibitory projections to neighborhood structures, CA1 is the main output of the hippocampus. One of these receptive regions is the layer V of the EC, which sends projections into the EC layers II/III, completing this way the loop EC-hippocampus-EC. it has been proposed that the parallel inputs to CA1 from the trisynaptic circuit and the direct EC pathway act as a comparison mechanism of the stored information with direct spatial and nonspatial sensory information from the EC, leading to discrimination of new contexts (Basu & Siegelbaum, 2015). In general, CA1 is engaged in cognitive tasks such as spatial processing, learning, and memory (Bezaire et al., 2016).

1.5 Dendrites

Dendrites are thin neuronal protrusions that receive the vast majority of synaptic inputs and propagate them towards the soma. Early studies portrayed dendrites simply as passive propagators of synaptic currents. However, recent studies suggest that dendrites can operate semi-independently from the soma, greatly increasing the computational capacity of neurons (Bassett et al., 2020; Johnston et al., 1996). Their passive cable properties and the presence of dendritic voltage-gated ion channels

can greatly impact how synaptic information is translated into neuronal output (Spruston & Häusser, 2016). Moreover, dendrites allow multiple input integration sites with unique properties (depending on local morphological features and ion channel content) to coexist within a single neuron. Dendrites, depending on their morphology, their ratios of ion channels, and their ability to produce dendritic spikes, i.e., sodium, calcium, or NMDA spikes (**fig. 8**), can alter the linear summation of the synaptic inputs to supra-linear or sub-linear summation, and induce LTP (Papoutsi, Kastellakis, et al., 2014).

Dendritic mechanisms may last from just a few milliseconds to hundreds of milliseconds, leading to complex computations such as input amplification/segregation, coincidence detection, and parallel nonlinear processing (Poirazi & Papoutsi, 2020). Furthermore, the positioning of synapses across dendrites plays an important role. Functionally related synapses usually form anatomical clusters, promoting computational efficiency and memory storage capacity by increasing the probability of dendritic spike initiation (Kastellakis et al., 2015).

Computational and experimental studies suggest that dendritic properties can greatly influence several mnemonic functions across different brain areas For example, dendrites affect pattern separation by modulating their excitability through ion channels (Oulé et al., 2021) and by increasing the sparsity of the EC inputs in different segments, which leads to a lower probability of temporal coincidence that is needed to activate the GCs (Chavlis et al., 2017). Moreover, it has been shown that decreasing AMPAR stability, the main glutamatergic receptor on dendrites, in the GCs affects pattern separation and pattern completion (Robert et al., 2020). Non-linear dendrites in an abstract hippocampal model improved memory storage and recall capacity (Kaifosh & Losonczy, 2016). Another computational study showed that NMDARs increase persistent activity in the prefrontal cortex (pfc), improving short-term memory (Papoutsi, Sidiropoulou, et al., 2014).

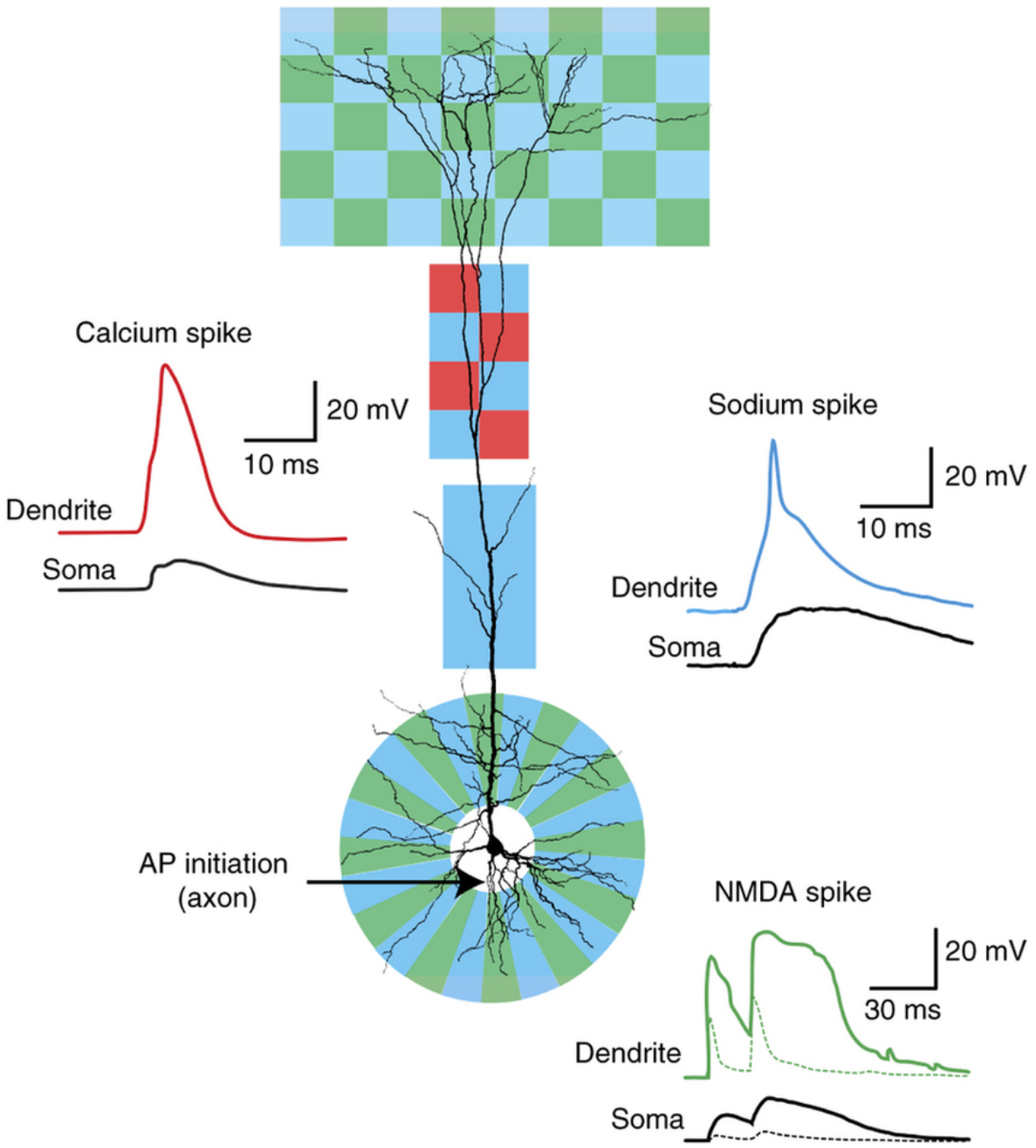

Figure 8. Location dependence of dendritic spike generation. Examples are shown of dendritic sodium (blue), calcium (red), and NMDA (green) spikes evoked by synaptic stimulation during simultaneous recordings from the soma (black), apical (blue, red), and basal (green) dendrites of a layer 5 pyramidal neuron. Dotted lines indicate the effect of blocking NMDA receptors. Colored boxes and circles superimposed onto the morphology of a cortical layer 5 pyramidal neuron indicate the dendritic regions in which these different spikes are usually generated. (Adapted from Stuart & Spruston, 2015)

1.6 Computational models

Neuroscience can be studied from different angles, either experimentally, by measuring various aspects of the brain, or theoretically, by constructing models that mimic the brain. Computational models provide a theoretical framework in which

experimental findings can be collected and integrated to infer the critical features of neuronal behavior at various levels. Models have the advantage to allow the fast, systematic, exhaustive, and reversible manipulation of properties that may not be subject to direct manipulation on living tissues. In particular, models in which features, properties, or morphologic characteristics of a neuron are changed can provide mechanistic explanations for experimental observations by identifying the key determinants of a specific phenomenon. Hypothesis-driven models, by the integration of existing data, can lead to unexpected predictions that can be subsequently validated by targeted experiments (Poirazi & Papoutsi, 2020).

One of the first neuronal models, which dates back to 1952, is the Hodgkin-Huxley model. Based on the description of the electrical properties of the cellular membrane, it models the emergence of action potentials in the squid giant axon, representing the problem as an equivalent circuit diagram (Hodgkin & Huxley, 1952). In 1957, Rall extended that model to include the cable theory, which laid the foundation for models of neurons having a three-dimensional description of the cell (Rall, 1957). However, many other models can vary depending on the computational complexity and biological realism (**fig. 9**).

For example, one of the most used models is the so-called Integrate-and-Fire model, introduced by Lapicque in 1907. Thanks to its simplicity, it allows modeling big networks with relatively low computational effort. Therefore, the choice of the model to use strictly depends on the question that needs to be addressed. Various publicly available databases and simulators provide the necessary tools for modeling phenomena at the desired level of analysis (Poirazi & Papoutsi, 2020, Table 1).

For this thesis, we decided to use a simplified, biologically relevant, scaled-down model of the DG, CA3, and CA1, consisting of four different cells (GCs, BCs, MCs, and HIPP cells) for the DG, and five different cells (Pyramidal cells, BCs, Bistratified cell (BiC), Vasoactive intestinal peptide/calretinin-expressing type 3 interneuron-specific cell (VIP), oriens lacunosum moleculare cell (OLM)) for the CA1/CA3 regions. Among these, only principal neurons are provided with several compartments to simulate dendrites, while others are described as point neurons. Dendrites and their active mechanisms are of utmost importance for neuronal network behaviors since they affect neuron activity. Therefore, we could explore the role of dendrites in the network level of the hippocampus while sustaining computational efficiency. We used the Conductance Adaptive Exponential (CAdEx) integrate-and-fire model as a sufficient description of neuronal activity (Górski et al., 2021), calibrating all parameters according to experimental data. The advantage of using such a simplified approach is that, with a small number of parameters, we could significantly reduce the computational effort and increase the network's size. This last aspect is fundamental to the study of a population coding effect, such as pattern separation and pattern completion. We first calibrated the passive and active properties of all neurons, then we validated the connectivity of each sub-network,

and finally, we merged them into the trisynaptic circuit, which replicated pattern completion and pattern separation.

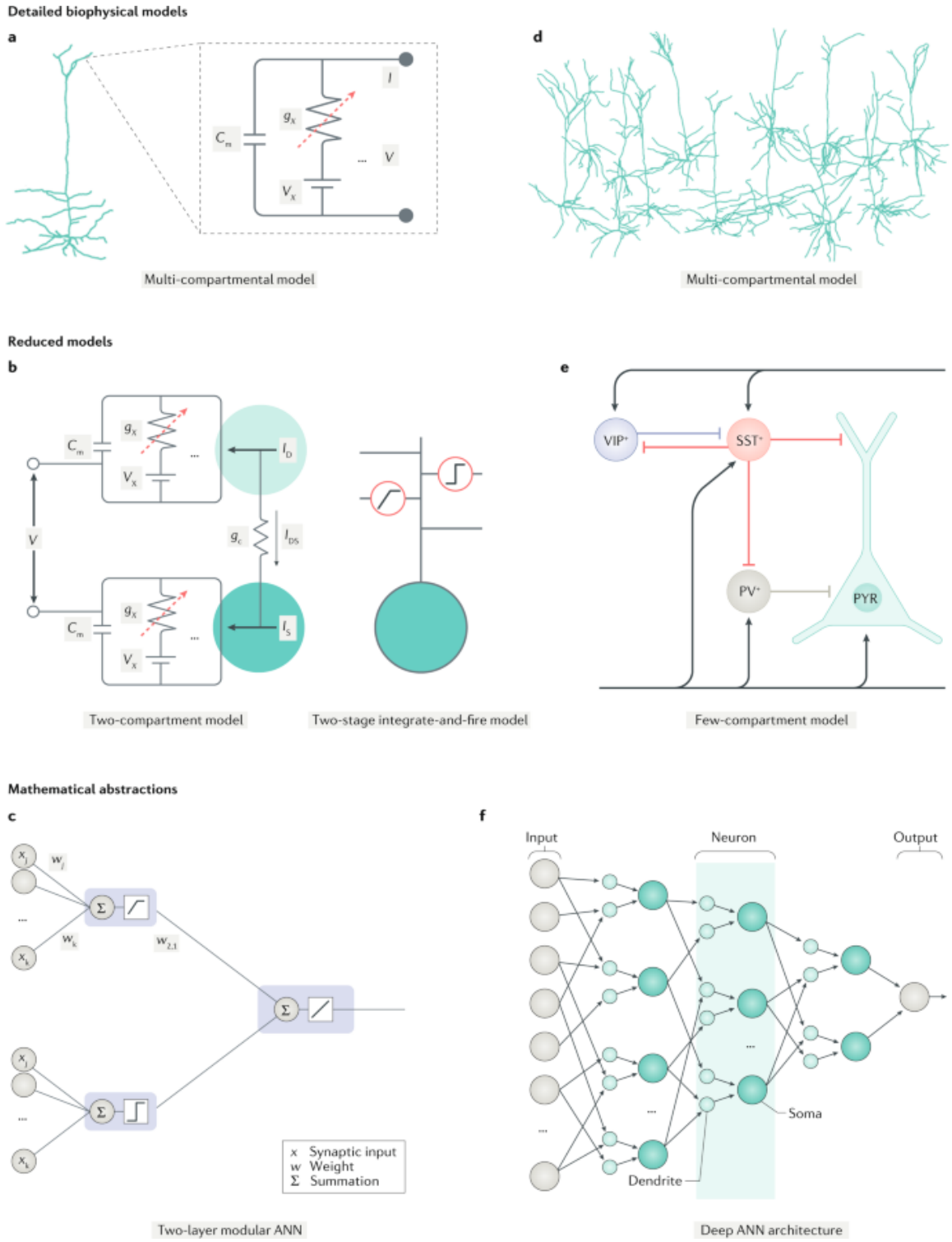

Figure 9. Levels of description in single-cell and circuit models with dendrites. a | Detailed multicompartmental models describe the morphology and biophysical properties of neurons by connecting hundreds to thousands of electrical compartments each with their conductances. These models are ideal for investigating how specific subcellular mechanisms (such as ionic conductances, receptors, and synaptic machinery) or

morphological features (for example, branch points) interact with one another and influence dendritic integration and/or neuronal output over time and/or space. These models provide mechanistic inferences that, in turn, allow for direct experimental testing of single-neuron-level computational hypotheses. However, they are computationally costly, as they have hundreds to thousands of parameters and require solving numerous differential equations to simulate current (I) and voltage (V) changes over time and space. Various algorithms have been developed for the optimization of the respective parameters. b | Examples of reduced models include simplification of multicompartmental models to just two compartments or integrate- and- fire models that use a few equations to describe the somatic and dendritic activity. These models are ideal for capturing simple features, such as the mean firing rate or the pattern of somatic output (for example, regular firing versus bursting). In such a model, the dendritic morphology and biophysics can be simplified or completely omitted. Reduced models ensure computational savings and also maintain the ability to probe the effects of selected mechanisms on neuronal output. Depending on the level of description implemented for dendrites, reduced models can account for some phenomena, such as the role of dendritic spikes in memory engrams or information binding. They are not appropriate, however, for studying the contributions of different membrane mechanisms to dendritic integration or the effect of morphological features on dendritic or neuronal output. c | Artificial neural network (ANN) abstraction of a neuron with two types of dendrites that are depicted as sigmoidal and saturating linear nodes. If the goal is not to simulate the activity of a neuron but, rather, to come up with a mathematical formalism that captures what a neuron computes, the best model can take the form of known statistical (for example, Bayesian), cascade (such as in linear–non- linear models) or other mathematical tools, such as ANNs. Theoretical models are ideal for formalizing neuronal computations and transferring insights from neuroscience to other disciplines (such as machine learning (ml) and artificial intelligence). They cannot, however, be used to identify the mechanistic underpinnings of the said computations in the neural tissue. d | Multicompartmental models of neurons can be connected to form detailed circuit models. These models can investigate network-level hypotheses and predict relevant biophysical mechanisms. e | Circuit models can be composed of different cell types that are represented by reduced compartmental or integrate- and- fire models with a small number of dendritic compartments. f | Deep ANN architectures can also consider dendrites through a structured connectivity scheme. Such architectures can be used to advance ml algorithms through the incorporation of biological features and/or to provide insights regarding potential dendritic or neuronal contributions to specific functions. Cm, specific membrane capacitance; gx, the conductance of ion x; ID, dendritic current; IS, somatic current; IDS, dendro- somatic current; red dotted arrow, voltage-gated conductance; PV+, parvalbumin-expressing; PYR, pyramidal; SST+, somatostatin expressing; VIP+, vasoactive intestinal peptide- expressing. Parts a,d adapted with permission from ref., American Physiological Society. (Adapted by Poirazi & Papoutsi, 2020)

Table 1 | **Popular modelling tools and databases**

Resource	Description	URL
Modelling tools		
NEURON	Simulator for detailed biophysical modelling	https://neuron.yale.edu/neuron/
BRIAN2	Spiking network simulator that also supports abstract dendritic modelling	https://brian2.readthedocs.io/en/stable/
GENESIS	Multilevel simulator that also supports biophysical modelling	http://genesis-sim.org/
LFPy	Enables the biophysical simulation of extracellular potentials	https://lfpy.readthedocs.io/en/latest/
OpenSourcebrain	Resource for sharing and collaboratively developing computational models of neural systems and generation of standardized models	http://opensourcebrain.org/
Trees toolbox	Morphological analysis, manipulations and artificially generated morphologies	https://www.treestoolbox.org/
Databases		
ModelDB	Repository of published models	https://senselab.med.yale.edu/modeldb/
NeuroMorpho	Repository of experimentally reconstructed single-neuron morphologies	http://neuromorpho.org/
ICGenealogy	Database of ion channel models	https://icg.neurotheory.ox.ac.uk/
Brain Observatory at the Allen Brain Institute	Provides access to the activity of different cell types of the mouse visual system	http://observatory.brain-map.org/visualcoding/
The Neocortical Microcircuit Collaboration Portal	Description of simulated microcircuit and associated NEURON models; repository of electrophysiological data; access to tools for morphological analyses and parameter optimization	https://bbp.epfl.ch/nmc-portal/welcome
Hippocampome	Portal for morphological, electrophysiological and anatomical data from the hippocampus and entorhinal cortex	http://hippocampome.org/php/index.php
MouseLight (Janelia)	Data set of whole mouse brains imaged at submicron resolution, allowing reconstructions of complete axonal arbours of individual neurons across the entire mouse brain	https://www.janelia.org/project-team/mouselight

2. Material and Methods

The hippocampal model implemented here consists of three sub-networks, those of the DG, CA3, and CA1. These models were inspired by previous works of our laboratory, i.e., DG from Chavlis et al. (2017), CA1, and CA3 from Turi et al. (2019). For computational efficiency and biological relevance, we used the mice's population of neurons for each region scaled down to a ratio of 1:500. The simulations were performed using the BRIAN 2.5.0.3 Simulator (Stimberg et al., 2019), written in python (version 3.8.5) (https://python.org), and running on high-performance computing cluster (HPCC).

2.1 Conductance adaptive exponential integrate-and-fire models (CAdEx)

The CAdEx integrate-and-fire model is a two-equation phenomenological model, which combines low computational cost and biophysical realism. It was inspired by a widely used two-variable model, the Adaptive Exponential (AdEx) integrate-and-fire model (Brette & Gerstner, 2005). These models are simplified phenomenological neuron models that require fewer free parameters than the Hodgin-Huxley formalism. The first equation of these models represents the membrane voltage, whereas the second one represents an adaptation factor allowing a wide variety of

dynamics and firing patterns, similar to biological recordings. The difference between AdEx and CAdEx is in the second variable. AdEx has the adaptation in the form of current and has linear subthreshold adaptation causing unrealistic behaviors after intense neuronal firings, instead, the adaptation in CAdEx has the form of conductance and a sigmoid dependence of subthreshold adaptation (Górski et al., 2021). We changed the equations slightly for better computational performance and these equations are as follows:

$$C\frac{dV}{dt} = g_L(E_L - V) + g_A(E_A - V) + I_S \quad (1)$$

$$\tau_A \frac{dg_A}{dt} = \frac{g_A}{1 + exp\left(\frac{V_A - V}{\Delta_A}\right)} - g_A \quad (2)$$

with after-spike reset mechanism:

$$if\ V \geq V_T\ then \begin{cases} V \rightarrow V_R \\ g_A \rightarrow g_A + \delta g_A \end{cases} \quad (3)$$

In the first equation: C is the membrane capacitance, V is the membrane voltage, g_L is the leak conductance, E_L is the reversal potential (i.e., the resting potential), g_A is the adaptation conductance, E_A is the reversal potential of the adaptation conductance, and I_S is an input current. In the second equation: τ_A is the time constant of adaptation, g_A is the adaptation conductance, $\bar{g}_A$ is the maximal subthreshold adaptation conductance, V_A is the subthreshold adaptation activation voltage, and Δ_A is the slope of subthreshold adaptation. The input resistance (R_{in}) is calculated by dividing the membrane capacitance by the leak conductance:

$R_{in} = C / g_L$ (4)

The third equation describes what happens to the model when an action potential occurs. Firstly, a condition must be satisfied for spike initiation: the membrane voltage (V) must reach or pass the threshold for action potential initiation (V_T). After a spike is fired, the membrane voltage (V) resets to a specific reset value (V_R), and the adaptation conductance (g_A) is incremented by a quantal conductance (δg_A).

All the neurons and dendrites of PCs are using these equations, with the difference that in dendrites the adaptation is always set to zero because their spiking mechanisms already incorporate adaptation.

2.2 Compartmental modeling

All of our principal neurons are modeled with a sphere for soma and cylinders for dendrites. After a full 3-D image of a neuron is attained, its modeling can begin by breaking it down into a series of cylinders with different lengths and diameters for its mathematical and computational description. For a given cylindrical compartment, the membrane resistance (R_m) is related to the area of the compartment as is the capacitance. Given a specific resistivity in Ohm-cm^2, the total resistance (R_M) is just this value divided by the area, $R_m=R_M/A$, where A is the area. The capacitance for the compartment is also proportional to the area.

There are a few rules to compute the axial resistance (Ri) between two compartments:

- If both are cylinders, we use the average of the two resistances
- If one is a sphere and the other is a cylinder, we use the cylinder's resistance

Given that we have two compartments with neuron's axial resistivity R_a Ω*cm, and length x diameter L_1 μm x D_1 μm & L_2 μm x D_2 μm, we get the following equations:

$A_1 = L_1 \times D_1 \times \pi$ μm^2 (5)
$A_2 = L_2 \times D_2 \times \pi$ μm^2 (6)
$Ri_1 = R_a \times L_1 / (\pi \times (D_1 / 2)^2$ (7)
$Ri_2 = R_a \times L_2 / (\pi \times (D_2 / 2)^2$ (8)

So, the Ri between the two compartments is equal to

$Ri = (Ri_1 + Ri_2) / 2$ (9)

This adds a current, I_{1-2} and I_{2-1} to the first and the second cylinder, respectively, to their voltage equation (**1**) and transforming them (**12**) and (**13**), respectively:

$I_{1-2} = (V_2 - V_1) /(A_1 \times Ri)$ (10)
$I_{2-1} = (V_1 - V_2) /(A_2 \times Ri)$ (11)

$$C\frac{dV_1}{dt} = g_L(E_L - V_1) + g_A(E_A - V_1) + I_S + I_{1-2} \quad (12)$$

$$C\frac{dV_2}{dt} = g_L(E_L - V_2) + g_A(E_A - V_2) + I_S + I_{2-1} \quad (13)$$

These two equations may seem identical, but the coupling strength between them is different. This way, the bigger compartments have more influence on the smaller

ones, and on the contrary, the smaller compartment has less influence on the bigger compartment (Ermentrout & Terman, 2010).

For our convenience, we will be using a general name, current $I_{coupling}$, for the currents $I_{1\text{-}2}$ and $I_{2\text{-}1}$. Therefore, equation (**1**) is transformed into a general form

$$C\frac{dV}{dt} = g_L(E_L - V) + g_A(E_A - V) + I_S + I_{coupling} \quad (14)$$

The membrane capacitance (C) and the leak conductance (g_L) differ for each compartment of all the principal neurons. These parameters are calculated according to two standard equations (**15**) (**16**) multiplied by the area of each compartment

$C = 1 \times sf\ \mu F/cm^2$ (15)
$g_L = C / \tau_m$ (16)

where sf is a scale factor that adjusts the size of the neuron's model, and τ_m is the neuron's membrane time constant.

For example, considering we want to model a spherical soma of diameter D_{soma} and area A_{soma}, the equation (**15**) (**16**) would be transformed into

$C_{soma} = C \times A_{soma}$ (17)
$g_{L\_soma} = C_{soma} / \tau_m$ (18)

Point neurons do not have dimensions, therefore, they do not have axial resistivity (R_a) and we directly put their membrane capacitance (C) parameter. Moreover, their $I_{coupling}$ is always equal to 0 pA.

2.3 Membrane Noise

The resting membrane potential of neurons from in vivo measurements (**fig. 10A**) (Malezieux et al., 2020) is completely different from the in vitro measurements (**fig. 10B**) (Sun et al., 2017). For this reason, we incorporated a colored noise current (I_{noise}) into equation (**14**) of the membrane potential, which drives into more positive values (Bono & Clopath, 2017). So equation (**14**) is transformed into

$$C\frac{dV}{dt} = g_L(E_L - V) + g_A(E_A - V) + I_S + I_{coupling} + I_{noise} \quad (19)$$

where I_{noise} is calculated by

$$\frac{\mathrm{d}I_{\mathrm{noise}}}{\mathrm{d}t} = \frac{(\mu_{\mathrm{noise}} - I_{\mathrm{noise}})}{\tau_{\mathrm{noise}}} + \xi\sigma_{\mathrm{noise}}\sqrt{\frac{2}{\tau_{\mathrm{noise}}/\mathrm{ms}}} \qquad (20)$$

In this equation: σ_{noise} is the standard deviation, μ_{noise} is the mean, τ_{noise} is the time-constant for the low-pass filtering of the noise, and ξ is Gaussian white noise with zero mean and unit s.d. (Bono & Clopath, 2017).

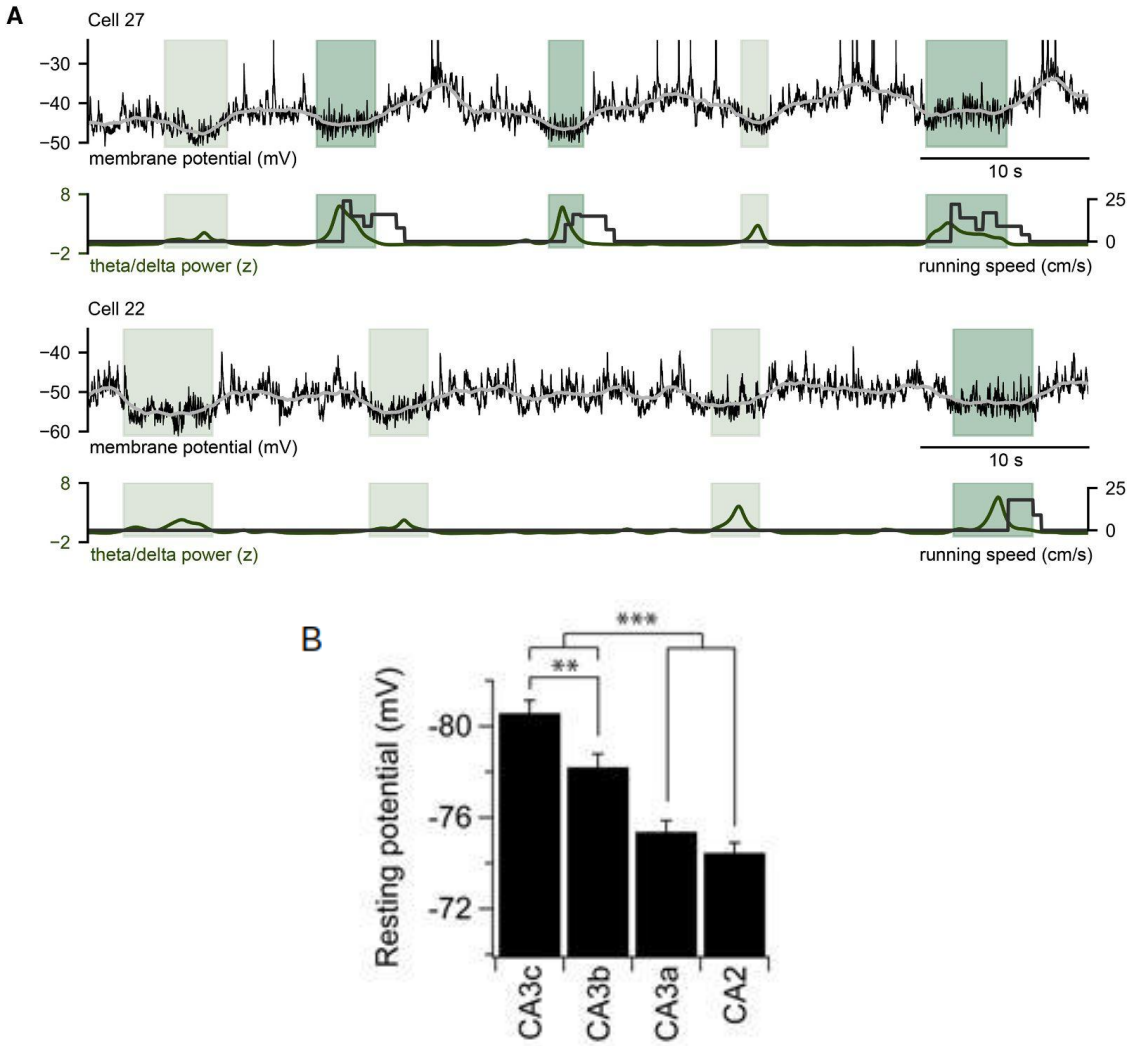

Figure 10. A) Example whole-cell recordings from two different CA3 PCs (top), with the simultaneous theta/delta power ratio of the nearby LFP and the running speed of the mouse (bottom). The gray trace superimposed on the raw membrane potential (Vm) is the smoothed Vm after spike removal, and green shading represents theta events. Spikes are truncated in the raw membrane potential traces. (Adapted from Malezieux et al., 2020) B) Mean resting membrane potential in indicated subregions. Error bars show SE. **p < 0.01, ***p < 0.001. n = 16–32 neurons per group. (Adapted from Sun et al., 2017)

2.4 Modeling synapses

For the synapses of the principal cells, we modeled the currents of three major ionotropic receptors: 1) AMPA receptors (AMPARs), 2) NMDA receptors (NMDARs), and 3) $GABA_A$ receptors (GABARs), whereas for all the other cells we modeled only the currents of AMPARs and GABARs. Across time, equation (**21**) can describe the majority of the ligand-gated ion channels, like AMPARs and GABARs, which, when they are active, display a linear current-voltage relationship.

$I_{AMPA/GABA} = g_{AMPA/GABA}(t) \times (V(t) - E_{AMPA/GABA})$ (21)

where $g_{AMPA/GABA}$ is the ohmic conductance of a channel, V is the membrane potential, and $E_{AMPA/GABA}$ is the reversal (equilibrium) potential.

However, the conductance of the NMDARs is not that simple because of the gate blockage by magnesium ions (Mg^{2+}) near the resting membrane potential. Along with the glutamate binding on the receptor, they need an electrostatic repulsion of the Mg^{2+} by the influx of positive ions caused by the opening of AMPARs. A sigmoidal function (s) can represent the fraction of NMDA channels that are unblocked:

$$s(V) = \frac{1}{1 + \eta[Mg^{2+}]_o \times e^{(-\gamma \times V)}} \quad (22)$$

where η is the sensitivity of Mg^{2+} unblock, γ is the steepness of Mg^{2+} unblock, and $[Mg^{2+}]_o$ is the concentration of extracellular Mg^{2+}. So, the equation that describes NMDAR's current is

$I_{NMDA} = g_{NMDA}(t) \times s(V) \times (V(t) - E_{NMDA})$ (23)

which is the same as the equation (**21**) with the addition of the sigmoidal function (**22**). All these currents are added in equation (**15**), but for our convenience, we will firstly include them all in a single synaptic current (I_{syn}), and then we will add this to the final equation.

$I_{syn} = I_{NMDA} + I_{AMPA} + I_{GABA}$ (24)

$$C\frac{dV}{dt} = g_L(E_L - V) + g_A(E_A - V) + I_S + I_{coupling} + I_{noise} + I_{syn} \quad (25)$$

2.5 The Dentate gyrus network

The DG was built according to previous works (Chavlis et al., 2017**;** Myers & Scharfman, 2009, 2011), using the biological relevant numbers of neurons (Buckmaster & Jongen-Rêlo, 1999; West et al., 1991) scaled down to a ratio of 1:500 and incorporates new information about connectivity. More specifically, the new connections are inhibitory synapses from the HIPP cells to other HIPP cells and BCs, so we could have a disinhibitory system and excitatory synapses from MCs to GCs for Backprojection purposes that we will describe later. These details are gathered in **Table 2** and a schematic representation (**fig. 11**).

Four major dentate neuron types were modeled, GCs, BCs, HIPP cells, and MCs. GCs because they are the principal cells of DG and MCs because they are another category of glutamatergic cells, a phenomenon not observed in other hippocampal sub-regions, and they modulate the DG network (Scharfman, 2016). BCs and HIPP cells were chosen to represent the interneurons of the DG, for the perisomatic inhibition and dendritic inhibition, respectively. This choice was made since there is not much data to model other interneurons.

Table 2. In the first column are the names of the cell types used in our model. The second column shows the biological measured numbers of these populations (Source: Dyhrfjeld-Johnsen et al., 2006), and in the third column are the numbers we used in our DG model.

Neuron's population		
Type	Biological	DG Model
Granule cells	1.000.000	2.000
Basket cells	10.000	20
HIPP cells	12.000	24
Mossy cells	30.000	60

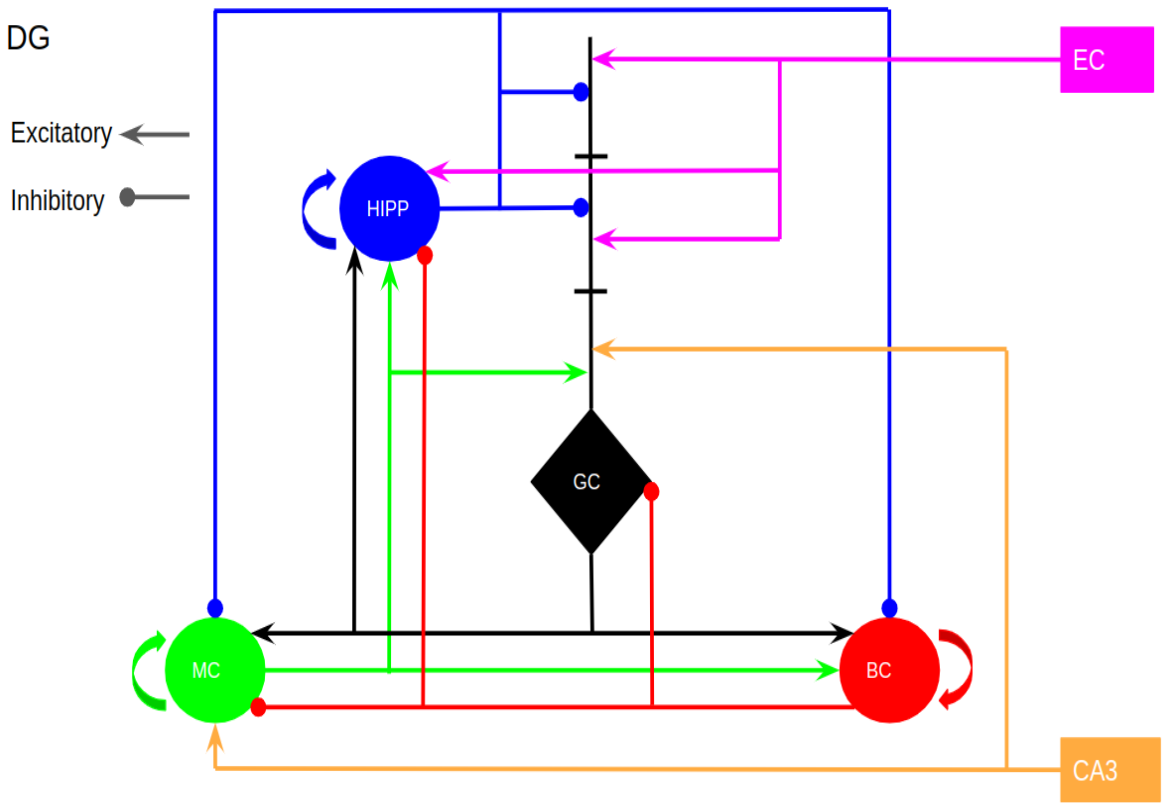

Figure 11. Schematic representation of the connections of the Dentate gyrus model. Excitatory inputs are represented by the pointy arrows. Inhibitory inputs are represented by the spheres. Recurrent synapses between the same population are represented by curved arrows.

2.5.1 Granule cells

Among the hippocampus principal cells, GCs have a characteristic morphology. Firstly, GC's cell bodies have an elliptical morph with a width of ~10 µm and a height of ~18 µm (Claiborne et al., 1990), they are densely packed in the gcl. They extend their dendrites from a big trunk into the ml, while the further they extend the thinner they become. Usually, their axon emerges from their basal pole and extends into the Hilus and CA3 region (**fig. 12A**) (Amaral et al., 2007). Usually, GCs do not have basal dendrites, but a small portion in healthy humans and monkeys, and a bigger in epileptic DG, appear to have basal dendrites (**fig. 12B**) (Becker et al., 2012; Kelly & Beck, 2017; Seress & Mrzljak, 1987). In our model, we did not include any GC with basal dendrite.

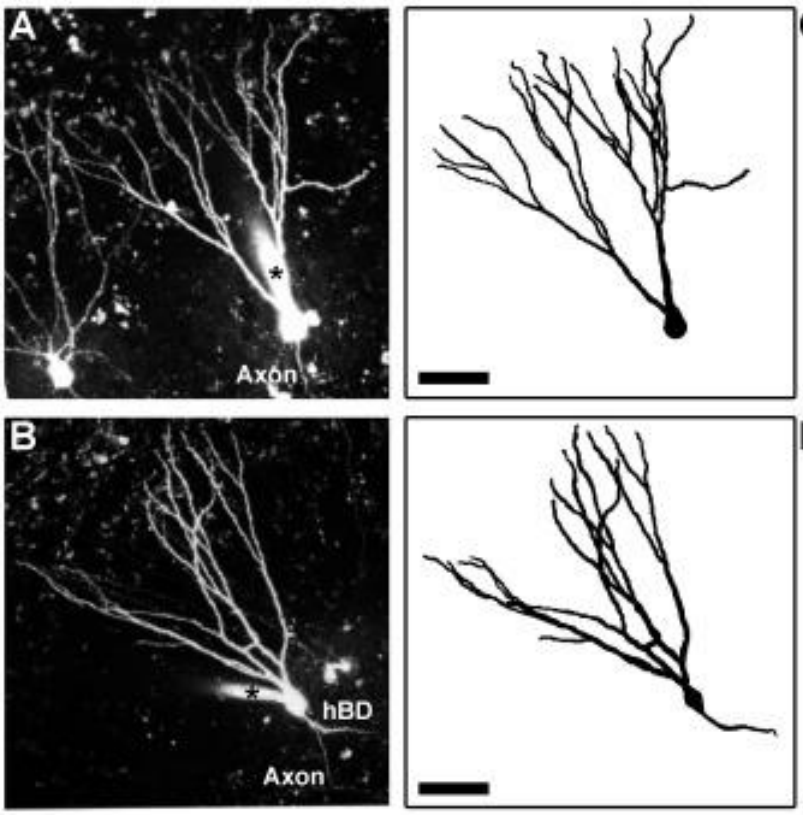

Figure 12. (A, B) Alexa-filled dentate GCs were reconstructed in confocal image stacks using Neuronstudio software. 2D-projected image stacks (left) and the corresponding reconstructed skeletons (right) are shown for a granule cell without (A) and with a hilar basal dendrite (hBD) (B). Scale bar: 50 µm. (Adapted from Becker et al., 2012)

For our model, we have built a reduced morphology of the GC using the diameter and length for each compartment from the work of Becker et al. (2012) (**fig. 13**). Our GC is made of: 1) a spherical soma, which receives inhibitory inputs from the BCs, 2) a short and big trunk sprouting from the soma, 3) a second thinner and longer trunk continuing from the first one, which receives excitatory inputs from the MCs 4) two oblique dendrites sprouting from the second trunk, and 5) two distal dendrites, each sprouting from an oblique dendrite. The oblique and distal dendrites are receiving excitatory inputs from the EC and inhibitory inputs from the HIPP cells. A cartoon along with the values of each compartment's length and diameter are presented in **Figure 14**.

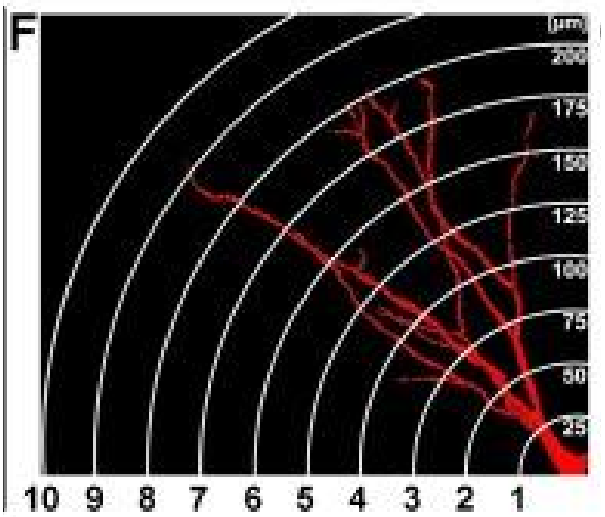

Figure 13. (F) The Sholl-analysis of the two GC populations showed a comparable complexity of the dendritic trees (distance of circles/spheres in F, 25 µm). (Adapted from Becker et al., 2012)

A

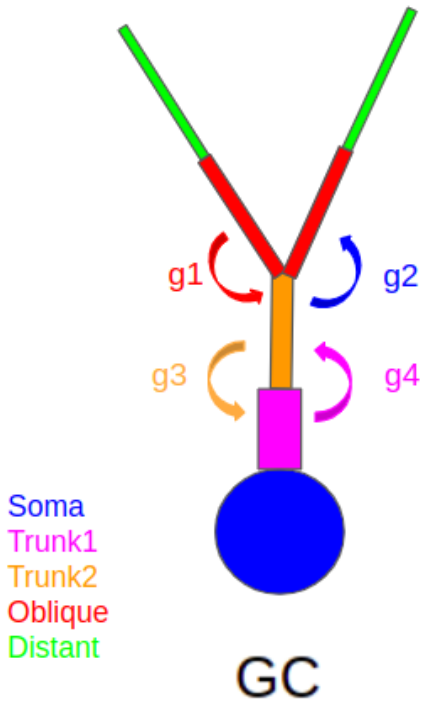

B

Compartment properties	GC
Diam_soma(um)	13
Len_trunk1 (um)	10
Diam_trunk1 (um)	4
Len_trunk2 (um)	20
Diam_trunk2 (um)	3
Len_oblique (um)	70
Diam_oblique (um)	1.1
Len_distal (um)	100
Diam_distal (um)	0.6

Figure 14. A) Representation of the granule cell model. (g1 is the $g_{coupling}$ from oblique dendrites to trunk2 with a value of 13.48 nS, g2 is the $g_{coupling}$ from trunk 2 to oblique dendrites with a value of 12 nS, g3 is the $g_{coupling}$ from trunk2 to trunk1 with a value of 20 nS, and g4 is the $g_{coupling}$ from trunk1 to trunk2 with a value of 17 nS) B) The diameters (Diam_) and lengths (Len_) of the GC model's compartments.

For the biophysical parameters of our GC model, we used the information from experimental works (Mishra & Narayanan, 2020; Vida et al., 2018) and a database containing information about the biophysical characteristics of the hippocampal neurons (**http://hippocampome.org/php/index.php**). According to equations (**25**), (**2**), and (**9**), for each compartment the distances and lengths are the same as in **Figure 14B**, the resting membrane potential (E_L) is equal to -75 mV, the axial resistivity (R_a) is equal to 194 Ω*cm, the input resistance (R_{in}) is equal to 300.95 MΩ, the membrane time constant (τ_m) is equal to 32 ms, the threshold for action potential initiation (V_T) is equal to -45 mV, the reset value (V_R) is equal to -55 mV, the time-constant for the low-pass filtering of the noise (τ_{noise}) is equal to 10 ms, the noise standard deviation (σ_{noise}) is equal to 0.5 pA, the mean (μ_{noise}) is equal to 1 pA, the scale factor (sf) is equal to 5, and for the adaptation of the soma the maximal subthreshold adaptation conductance ($\bar{g}_A$) is equal to 1.8 nS, the reversal potential of the adaptation conductance (E_A) is equal to -77.5 mV, the subthreshold adaptation activation voltage (V_A) is equal to -51 mV, the slope of subthreshold adaptation (Δ_A) is equal to 5 mV, the time constant of adaptation (τ_A) is equal to 90 ms, and the quantal conductance (δg_A) is equal to 2.9 nS. We changed slightly the backpropagating $g_{coupling}$ from “trunk1” to “trunk2”, and from “trunk2” to “oblique” dendrites, so we could achieve high backpropagate attenuation (**fig. 14A**).

2.5.2 Basket cells

In the borders between the gcl-Hilus, with a pyramidal-shaped cell body, a major GABAergic parvalbumin-positive (PV^+) group of interneurons, the BC (PV^+ BCs), exists. They got their name because they form a basket-like pericellular plexus around the cell body of GCs (**fig. 15**) (Amaral et al, 2007), targeting the somatic and perisomatic are of GCs (Kraushaar & Jonas, 2000). BCs are fast-spiking interneurons, meaning that they have high-frequency bursts of action potentials, and this was shown in in-vitro and in-vivo studies (Vida et al., 2006). This behavior provides potent inhibitory feedback to GCs, contributing this way to the DG computations (Seress & Ribak, 1990).

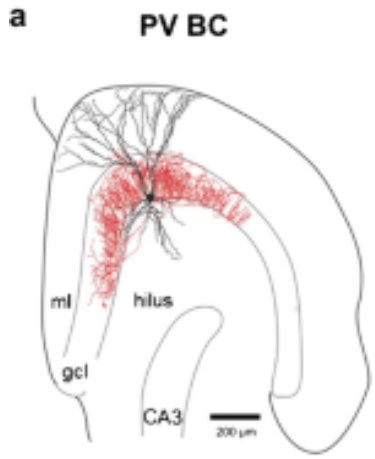

Figure 15. Morphology of the PV^+ BC. Soma and dendrites are in black and the axon is in red. (Adapted from Booker & Vida, 2018)

BCs connect, receive and send synapses, with GCs, other BCs (Booker & Vida, 2018), HIPP cells (Savanthrapadian et al., 2014), and MCs (Dyhrfjeld-Johnsen et al., 2007).

For the biophysical parameters of our BC model, we used the information from experimental works (Lübke et al., 1998) and a database containing information about the biophysical characteristics of the hippocampal neurons (**http://hippocampome.org/php/index.php**). According to equations (**25**), (**2**), the resting membrane potential (E_L) is equal to -57 mV, the input resistance (R_{in}) is equal to 53.46 MΩ, the membrane capacitance (C) is equal to 179.3 pF, the membrane time constant (τ_m) is equal to 9.96 ms, the threshold for action potential initiation (V_T) is equal to -45.2 mV, the reset value (V_R) is equal to -50 mV, the time-constant for the low-pass filtering of the noise (τ_{noise}) is equal to 15 ms, the noise standard deviation (σ_{noise}) is equal to 3 pA, the mean (μ_{noise}) is equal to 5 pA, and for the adaptation of the soma the maximal subthreshold adaptation conductance ($\bar{g}_A$) is equal to 1 nS, the reversal potential of the adaptation conductance (E_A) is equal to -59 mV, the subthreshold adaptation activation voltage (V_A) is equal to -45 mV, the slope of subthreshold adaptation (Δ_A) is equal to -10 mV, the time constant of adaptation (τ_A) is equal to 165 ms, and the quantal conductance (δg_A) is equal to 1.3 nS.

2.5.3 HIPP cells

SST^+ hilar perforant path (HIPP) cells have their somata in the pcl and they are characterized by spiny horizontal, bipolar dendrites, which expand only in the gcl (**fig. 16**). Their axon emerges from a proximal dendrite, branching at a high rate in the oml and inhibiting the oblique and distal dendrites of GCs. A small portion of their axon remains in the hilus and contacts interneurons, making a disinhibitory circuit (Booker & Vida, 2018).

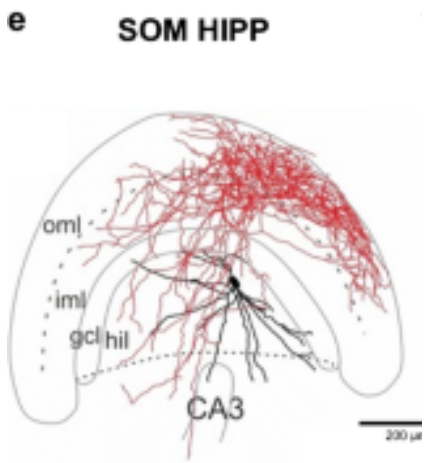

Figure 15. Morphology of the HIPP cell. Soma and dendrites are in black and the axon is in red. (Adapted from Booker & Vida, 2018)

For the biophysical parameters of our HIPP model, we used the information from experimental works (Yuan et al., 2017) and a database containing information about the biophysical characteristics of the hippocampal neurons (**http://hippocampome.org/php/index.php**). According to equations (**25**), (**2**), the resting membrane potential (E_L) is equal to -54.5 mV, the input resistance (R_{in}) is equal to 311.52 MΩ, the membrane capacitance (C) is equal to 45 pF, the membrane time constant (τ_m) is equal to 14.01 ms, the threshold for action potential initiation (V_T) is equal to -35 mV, the reset value (V_R) is equal to -45 mV, the time-constant for the low-pass filtering of the noise (τ_{noise}) is equal to 10 ms, the noise standard deviation (σ_{noise}) is equal to 3 pA, the mean (μ_{noise}) is equal to 5 pA, and for the adaptation of the soma the maximal subthreshold adaptation conductance ($\bar{g}_A$) is equal to 1 nS, the reversal potential of the adaptation conductance (E_A) is equal to -56 mV, the subthreshold adaptation activation voltage (V_A) is equal to -41 mV, the slope of subthreshold adaptation (Δ_A) is equal to 5 mV, the time constant of adaptation (τ_A) is equal to 65 ms, and the quantal conductance (δg_A) is equal to 3 nS.

2.5.4 Mossy cells

In the hilus, there is a category of neurons different from the inhibitory cells, the MCs. MCs are excitatory neurons that do not define as a component of the classical trisynaptic pathway (Hedrick et al., 2017). MCs are contacting both GCs and interneurons, and even though they send excitatory synapses to GCs, their main role is to inhibit them through interneurons (Scharfman, 2016). They are characterized by a large cell body with a triangular or multipolar shape (**fig. 16**) (Amaral et al., 1990; Scharfman, 2016). They receive excitatory inputs from GCs and CA3 pyramidals backprojection (Hedrick et al., 2017).

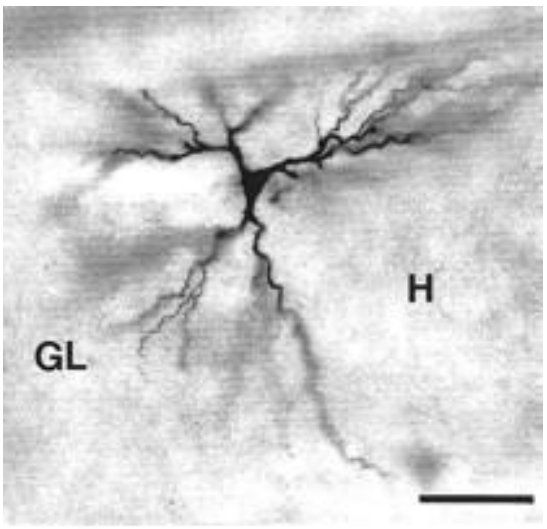

Figure 16. Morphological characteristics of hilar MCs. H, hilar region; GL, granule cell layer; Scale bar: 100 μm. (Adapted from Lübke et al., 1998)

For the biophysical parameters of our MC model, we used the information from experimental works (Lübke et al., 1998) and a database containing information about the biophysical characteristics of the hippocampal neurons (**http://hippocampome.org/php/index.php**). According to equations (**25**), (**2**), the resting membrane potential (E_L) is equal to -62 mV, the input resistance (R_{in}) is equal to 199.99 MΩ, the membrane capacitance (C) is equal to 205 pF, the membrane time constant (τ_m) is equal to 41 ms, the threshold for action potential initiation (V_T) is equal to -39 mV, the reset value (V_R) is equal to -50 mV, the time-constant for the low-pass filtering of the noise (τ_{noise}) is equal to 10 ms, the noise standard deviation (σ_{noise}) is equal to 3 pA, the mean (μ_{noise}) is equal to 5 pA, and for the adaptation of the soma the maximal subthreshold adaptation conductance ($\bar{g}_A$) is equal to 1.8 nS, the reversal potential of the adaptation conductance (E_A) is equal to -64 mV, the subthreshold adaptation activation voltage (V_A) is equal to -46 mV, the slope of subthreshold adaptation (Δ_A) is equal to 5 mV, the time constant of adaptation (τ_A) is equal to 100 ms, and the quantal conductance (δg_A) is equal to 10 nS.

2.5.5 The network

In detail, 2,000 GCs and 20 BCs are organized in 10 nonoverlapping clusters of 200 GCs and 2 BCs each to replicate the lamellar organization across the septotemporal axis of DG (Sloviter & Lømo, 2012). In each cluster, all the GCs are contacting all the BCs and vice versa. This connectivity was chosen for two reasons: 1) using the connectivity of BCs to GCs from biological measurements (Dyhrfjeld-Johnsen et al., 2007) would not be enough to facilitate inhibition to all the GCs, and 2) this way we can achieve the “winner-take-all” competition (Coultrip et al., 1992) in which only the strongest activated GCs in a cluster will remain active. By using this method, we reached a granular activity of 2-5%, the same as the theoretical and experimental estimations (Treves et al., 2008). However, 24 HIPP cells and 60 MCs do not have a

topological organization because their numbers are not enough to attain this characteristic in our model (Morgan et al., 2007). The HIPP cells send synapses to GCs in a way to contact randomly 20% of GCs (Chavlis et al., 2017), they contact other HIPP cells with a probability of 5.2% and BCs with a probability of 12.8% (Savanthrapadian et al., 2014). The MCs receive synapses from the GCs with a probability of 20% (Chavlis et al., 2017), and they send synapses back to the GCs with a probability of 3.25%. Each MC connects with every BC.

As for the input in the DG network, 200,000 EC cells (Amaral et al, 1990), scaled-down by 500 times to match the whole network cell numbers, were modeled as random Poisson inputs with the frequency of 40 Hz (Chavlis et al., 2017**,** Myers & Scharfman, 2009), in agreement with experimental data (Hafting et al., 2005). In previous experimental work, it was shown that 10% of the total 4,000 EC afferents that each GC receives are active and are needed to discharge it (McNaughton et al., 1991). With our 400 EC inputs, that would mean each GC receiving only 8 synapses, which would be insufficient for their activation. For this reason, we used a randomly determined 10% of the ECs for each GC as input. EC layer II cells are connected to the HIPP cells with a random probability of 20% (Chavlis et al., 2017**,** Myers & Scharfman, 2009).

2.6 The Cornu Ammonis networks

The CA3 and CA1 networks were built similarly for three reasons. First, CA3 and CA1 have a similar constitution of neuron populations, and in our effort to keep the whole network simple, we used the same interneuron models. Second, there is not enough data about the numbers of interneurons in the CA3 region, but there is excess data for the CA1, so we used the same proportions according to the principal neuron's number. Lastly, we experienced the same problem with the intrinsic connectivity of the CA3, so we used connectivity according to the CA1 region.

So, we will be referring to both of them as CA networks, and wherever there is the need to point more specific-region details we will be using the specific-region name. The size of CA3 pyramidals (Hosseini-Sharifabad & Nyengaard, 2007), CA1 pyramidals, and interneurons (Bezaire & Soltesz, 2013) were scaled down to a ratio of 1:500, but the interneuron's numbers of each region were multiplied so they would consist ~20% of the principal cells (**Table 3**) (Basu & Siegelbaum, 2015; Honoré et al., 2021). For the connections of the CA networks, we used data from experimental data (Bezaire et al., 2016; Bezaire & Soltesz, 2013) and scaled it down 35 times to match the reduced size of our network (**Table 4**). There are three differences between the two sub-networks: 1) CA3 pyramidals receive synapses, in the form of big boutons, from the GCs into their trunk, while CA1 pyramidals receive afferents from CA3 pyramidals into their oblique and basal dendrites, 2) CA3 pyramidals are characterized by their extensive recurrent connections (Rebola et al., 2017), while

CA1 pyramidals were shown to have low rates of recurrent synapses (Owen et al., 2021; Yang et al., 2014), and 3) CA3 region receive afferent inputs mainly from the EC layer II, while CA1 region receives afferents from EC III (Andersen et al., 2007).

Table 3. In the first column are the names of the cell types used in our model. The second column shows the biological measured numbers of these populations (Source: 1) Honore et al., 2021, 2) Basu & Siegelbaum, 2015), in the third column are the numbers we used in our CA3 model, and in the fourth column are the numbers we used in our CA1 model.

Neuron's population			
Type	Biological CA3 / CA1	CA3 model	CA1 model
PCs	200,000[1] / 311,500[2]	400	623
BCs	5,530[2]	44	66
BiCs	2,210[2]	18	26
OLMs	1,640[2]	12	20
VIPs	1,250[2]	10	15

Table 4. Connectivity matrix (number of synaptic connections) of the CA model networks.

From/to	PCs	BCs	BICs	OLMs	VIPs
EC	8	4	25	x	32
CA3	8	345	330	57	143
PC	6	36	31	203	118
BC	5	1	1	x	1
BIC	3	4	4	11	1
OLM	2	2	2	2	1
VIP	x	3	x	11	x

We modeled five major neuron groups, pyramidals, which are the principal cells (PCs), BCs, BiCs, OLMs, and VIPs. These interneurons were chosen because they

are well studied, and to be more precise, each one of them has a unique attribute. BCs interfere with the pyramidal's excitatory inputs via perisomatic inhibition, BiCs counterbalance the excitatory inputs on the basal and proximal dendrites, whilst OLMs counterbalance them on the distal dendrites of the pyramidals. VIPs act as the main disinhibitory mechanism, controlling the IN's activity. We made schematic representations for the connectivity pathways of CA3 (**fig. 17**) and CA1 (**fig. 18**) networks.

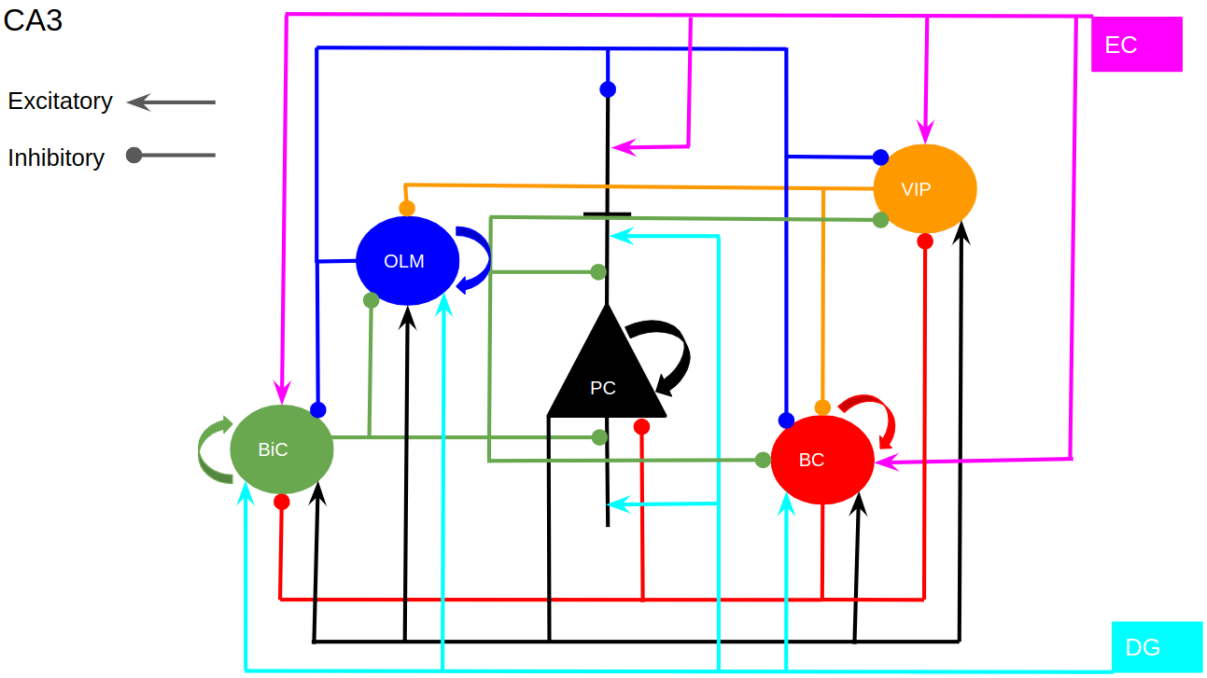

Figure 17. Schematic representation of the connections of the CA3 model. Excitatory inputs are represented by the pointy arrows. Inhibitory inputs are represented by the spheres. Recurrent synapses between the same population are represented by curved arrows.

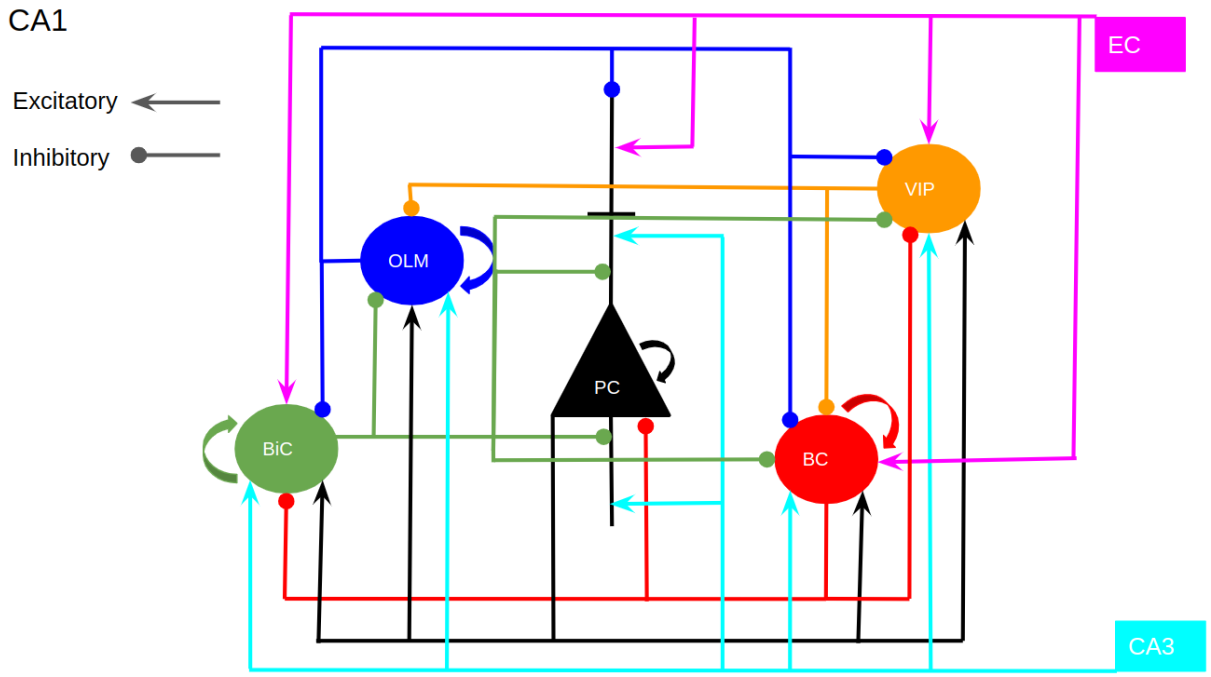

Figure 18. Schematic representation of the connections of the CA1 model. Excitatory inputs are represented by the pointy arrows. Inhibitory inputs are represented by the spheres. Recurrent synapses between the same population are represented by curved arrows.

2.6.1 CA3 pyramidal cell

CA3 pyramidal neurons are characterized by their bigger pyramid-shaped somata, compared to the CA1 pyramidals, which are located in sp and sprout basal and apical dendrites. They have basal dendrites that extend in the whole so, a short apical trunk in sl that branches into a few more secondary trunks, oblique dendrites in the sr, and distal dendrites in the sl-m. But across the whole region, CA3 pyramidal neurons differ in their organization and total dendritic length (Andersen et al., 2007)

For our model, we have built a reduced morphology of the CA3 pyramidal cell using the diameters of the CA1 pyramidal cells (Benavides-Piccione et al., 2020) with slightly bigger diameters for the soma and trunks, and CA3 pyramidal cell's lengths (**fig. 19**) (Sun et al., 2017). The model consists of 1) a big spherical soma, which receives inhibitory inputs from the BCs, 2) a trunk sprouting from the soma, which receives excitatory inputs from the GCs, 3) a second thinner and longer trunk continuing from the first one, 4) two oblique dendrites sprouting from the first trunk, 5) two distal dendrites sprouting from the second trunk, which receive excitatory inputs from the EC layer II and inhibitory inputs from the OLMs, and 6) two basal dendrites sprouting directly from the soma (**fig. 20**). The oblique and basal dendrites receive excitatory synapses from other CA3 pyramidals and inhibitory synapses from the BiCs (**fig. 17**).

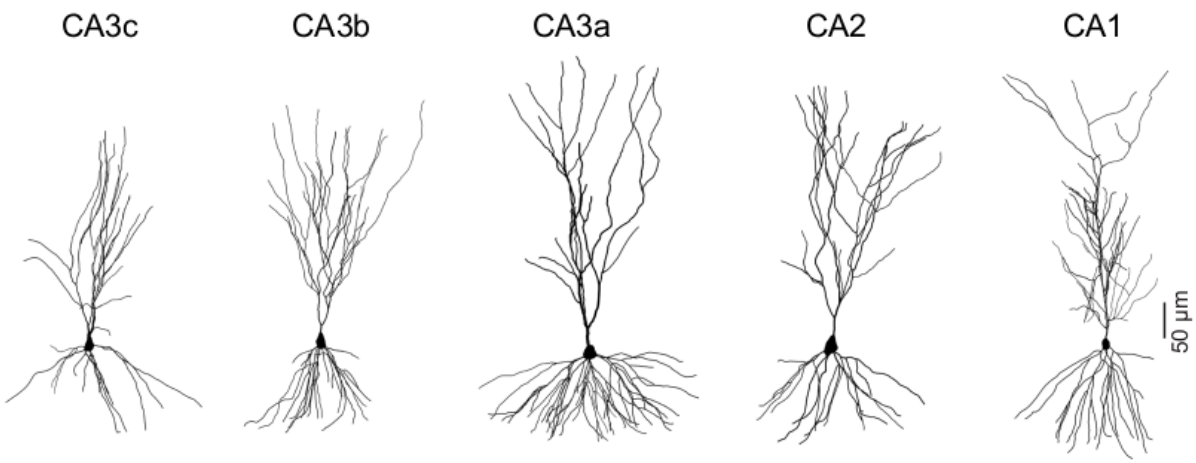

Figure 19. Representative morphology from biocytin-based reconstructions of hippocampal pyramidal neurons. (Adapted from Sun et al., 2017)

A

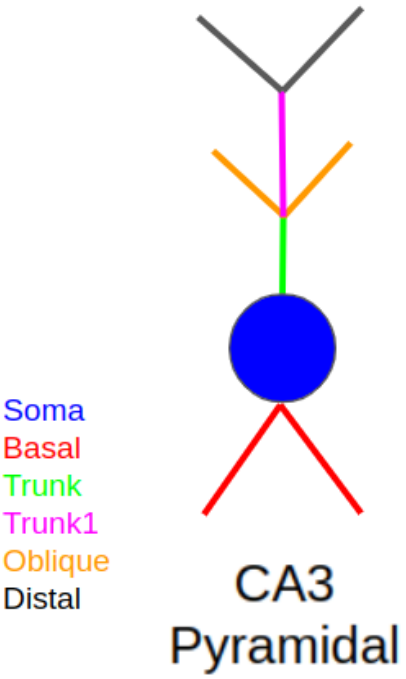

B

Compartment properties	CA3 Pyramidal
Diam_soma(um)	20
Len_basal (um)	100
Diam_basal (um)	0.68
Len_trunk (um)	75
Diam_trunk (um)	1.9
Len_oblique (um)	75
Diam_oblique (um)	0.73
Len_trunk1 (um)	100
Diam_trunk1 (um)	1
Len_distal (um)	100
Diam_distal (um)	0.72

Figure 20. A) Representation of the CA3 pyramidal cell model. B) The diameters (Diam_) and lengths (Len_) of the CA3 pyramidal model's compartments.

For the biophysical parameters of our CA3 model, we used the information from experimental work (Sun et al., 2017) and a database containing information about the biophysical characteristics of the hippocampal neurons (http://hippocampome.org/php/index.php). According to equations (**25**), (**2**), and (**9**), for each compartment the distances and lengths are the same as in **Figure 20**, the resting membrane potential (E_L) is equal to -72 mV, the axial resistivity (R_a) is equal to 192 Ω*cm, the input resistance (R_{in}) is equal to ~203 MΩ, the membrane time constant (τ_m) is equal to 36 ms, the threshold for action potential initiation (V_T) is equal to -44 mV, the reset value (V_R) is equal to -60 mV, the time-constant for the low-pass filtering of the noise (τ_{noise}) is equal to 5 ms, the noise standard deviation (σ_{noise}) is equal to 4 pA, the mean (μ_{noise}) is equal to 9 pA, the scale factor (sf) is equal to 5, and for the adaptation of the soma the maximal subthreshold adaptation conductance ($\bar{g}_A$) is equal to 1.4 nS, the reversal potential of the adaptation conductance (E_A) is equal to -75 mV, the subthreshold adaptation activation voltage (V_A) is equal to -50 mV, the slope of subthreshold adaptation (Δ_A) is equal to 5 mV, the time constant of adaptation (τ_A) is equal to 320 ms, and the quantal conductance (δg_A) is equal to 7.6 nS.

2.6.2 CA1 pyramidal cell

CA1 pyramidal neurons are similar to the CA3 ones, but they have smaller pyramid-shaped somata, which are located in sp and sprout basal and apical dendrites. Their dendrites most of the time extend in a roughly conical area. These pyramidals can be classified into two groups, one which their trunk bifurcates, after it crossed all the sr, in the sl-m, and one which their trunk bifurcates in the sr. But across the whole region, CA1 pyramidal neurons differ in their organization and total dendritic length (Andersen et al., 2007).

For our model, we have built a reduced morphology of the CA1 pyramidal cell using the diameters from the work of Benavides-Piccione et al. (2019) and lengths from **Figure 19** (Sun et al., 2017). The model consists of 1) a spherical soma, which receives inhibitory inputs from the BCs, 2) a trunk sprouting from the soma, 3) a second thinner and longer trunk continuing from the first one, 4) two oblique dendrites sprouting from the first trunk, 5) two distal dendrites sprouting from the second trunk, which receive excitatory inputs from the EC layer II and inhibitory inputs from the OLMs, and 6) two basal dendrites sprouting directly from the soma (**fig. 21**). The oblique and basal dendrites receive excitatory synapses from the CA3 pyramidals and inhibitory synapses from the BiCs. Moreover, the basal dendrites receive collateral synapses from other CA1 pyramidals (**fig. 18**).

For the biophysical parameters of our CA1 model, we used the information from experimental work (Masurkar et al., 2020) and a database containing information about the biophysical characteristics of the hippocampal neurons (http://hippocampome.org/php/index.php). According to equations (**25**), (**2**), and

(**9**), for each compartment the distances and lengths are the same as in **Figure 21**, the resting membrane potential (E_L) is equal to -64 mV, the axial resistivity (R_a) is equal to 200 Ω*cm, the input resistance (R_{in}) is equal to ~166 MΩ, the membrane time constant (τ_m) is equal to 22 ms, the threshold for action potential initiation (V_T) is equal to -44 mV, the reset value (V_R) is equal to -50 mV, the time-constant for the low-pass filtering of the noise (τ_{noise}) is equal to 15 ms, the noise standard deviation (σ_{noise}) is equal to 3 pA, the mean (μ_{noise}) is equal to 5.5 pA, the scale factor (sf) is equal to 5, and for the adaptation of the soma the maximal subthreshold adaptation conductance ($\bar{g}_A$) is equal to 2.2 nS, the reversal potential of the adaptation conductance (E_A) is equal to -69 mV, the subthreshold adaptation activation voltage (V_A) is equal to -52 mV, the slope of subthreshold adaptation (Δ_A) is equal to 5 mV, the time constant of adaptation (τ_A) is equal to 170 ms, and the quantal conductance (δg_A) is equal to 3.15 nS.

A

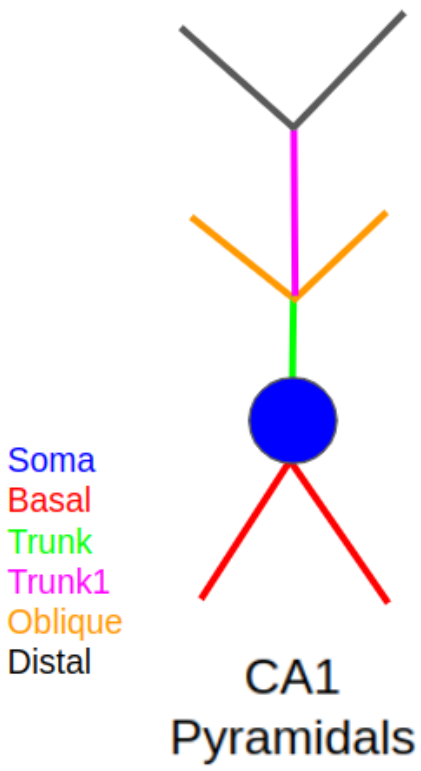

B

Compartment properties	CA1 Pyramidals
Diam_soma(um)	15
Len_basal (um)	150
Diam_basal (um)	0.68
Len_trunk (um)	75
Diam_trunk (um)	1.7
Len_oblique (um)	100
Diam_oblique (um)	0.73
Len_trunk1 (um)	125
Diam_trunk1 (um)	0.9
Len_distal (um)	100
Diam_distal (um)	0.72

Figure 21. A) Representation of the CA1 pyramidal cell model. B) The diameters (Diam_) and lengths (Len_) of the CA1 pyramidal model's compartments.

2.6.3 Basket cell

With somata inside or near the borders of the sp layer, fast-spiking PV⁺ BCs account for the major category of the CA region's BCs (**fig. 22**). They target the somata and proximal dendrites of the pyramidal neurons, other PV⁺ BCs, BiCs, and VIPs (Bezaire & Soltesz, 2013; Booker & Vida, 2018)

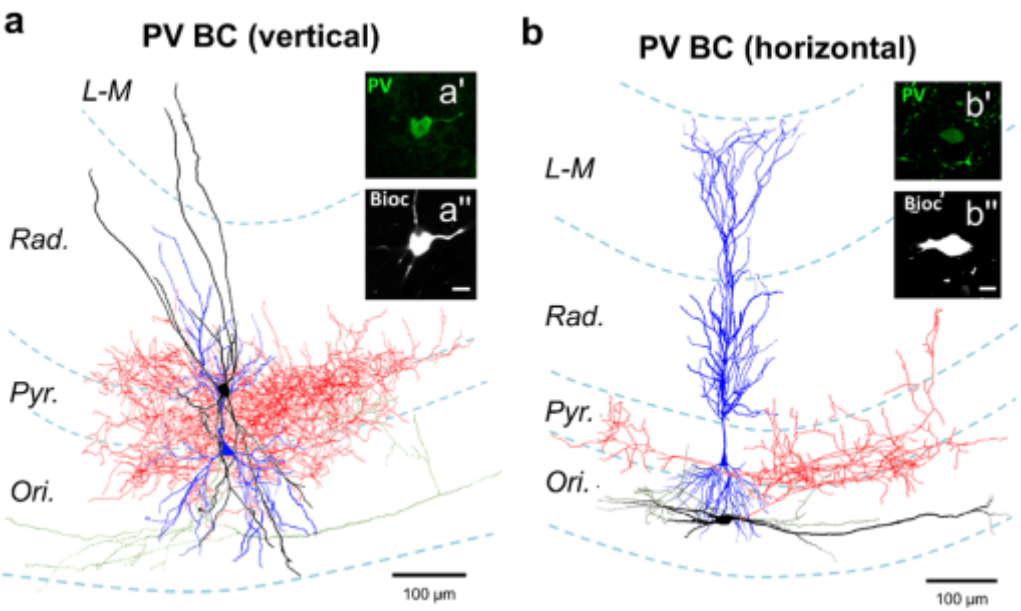

Figure 22. Example reconstructions of PV BCs. Soma and dendrites are shown as black, while the axon is shown as red. All reconstructions are shown with respect to CA1 layers: Ori, str. oriens; Pyr, str. pyramidale; Rad., str. radiatum; L-M, str. lacunosum-moleculare (Adapted from Booker & Vida, 2018)

For the biophysical parameters of our CA network's BCs model, we used the information from experimental work (Papp et al., 2013) and a database containing information about the biophysical characteristics of the hippocampal neurons (**http://hippocampome.org/php/index.php**). According to equations (**25**), (**2**), the resting membrane potential (E_L) is equal to -57 mV, the input resistance (R_{in}) is equal to ~96 MΩ, the membrane capacitance (C) is equal to 105.6 pF, the membrane time constant (τ_m) is equal to 11 ms, the threshold for action potential initiation (V_T) is equal to -38 mV, the reset value (V_R) is equal to -50 mV, the time-constant for the low-pass filtering of the noise (τ_{noise}) is equal to 10 ms, the noise standard deviation (σ_{noise}) is equal to 3 pA, the mean (μ_{noise}) is equal to 5 pA, and for the adaptation of the soma the maximal subthreshold adaptation conductance ($\bar{g}_A$) is equal to 1 nS, the reversal potential of the adaptation conductance (E_A) is equal to -59 mV, the subthreshold adaptation activation voltage (V_A) is equal to -45 mV, the slope of subthreshold adaptation (Δ_A) is equal to -10 mV, the time constant of adaptation (τ_A) is equal to 165 ms, and the quantal conductance (δg_A) is equal to 0.6 nS.

2.6.4 Bistratified cell

With dendrites across all layers, an axon that ramifies strong within the sr and so, and a soma located near the sp, the vertical BiC are SST^+ and account for 16-25% of all PV interneurons (**fig. 23**). Therefore, they inhibit the oblique and basal dendrites of the pyramidal neurons (Booker & Vida, 2018). They also contact other BiCs, BCs, VIPs, and OLMs (Bezaire & Soltesz, 2013).

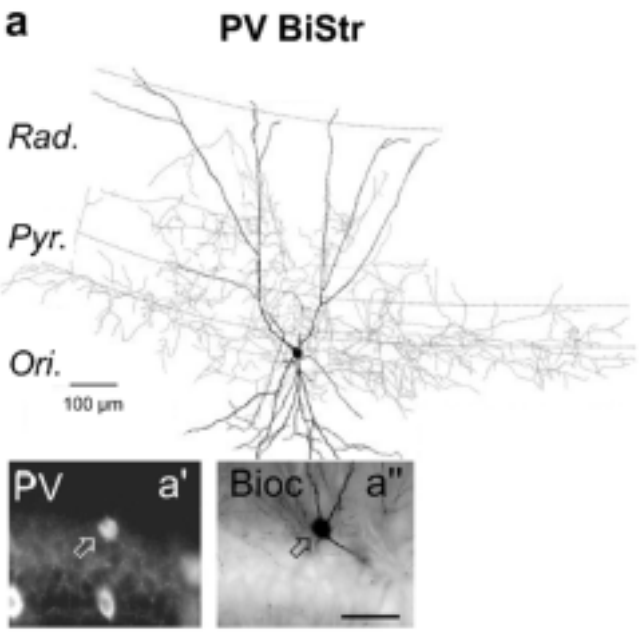

Figure 22. Example reconstruction of PV BiC. Soma and dendrites are shown as black, while the axon is shown as gray. The reconstruction is shown with respect to CA1 layers: Ori, str. oriens; Pyr, str. pyramidale; Rad., str. radiatum; L-M, str. lacunosum-moleculare. (Adapted from Booker & Vida, 2018)

For the biophysical parameters of our CA network's BiCs model, we used the information from experimental works (Bezaire et al., 2016) and a database containing information about the biophysical characteristics of the hippocampal neurons (**http://hippocampome.org/php/index.php**). According to equations (**25**), (**2**), the resting membrane potential (E_L) is equal to -67 mV, the input resistance (R_{in}) is equal to ~96 MΩ, the membrane capacitance (C) is equal to 100 pF, the membrane time constant (τ_m) is equal to 11.6 ms, the threshold for action potential initiation (V_T) is equal to -43 mV, the reset value (V_R) is equal to -58 mV, the time-constant for the low-pass filtering of the noise (τ_{noise}) is equal to 10 ms, the noise standard deviation (σ_{noise}) is equal to 3 pA, the mean (μ_{noise}) is equal to 5 pA, and for the adaptation of the soma the maximal subthreshold adaptation conductance ($\bar{g}_A$) is equal to 0.8 nS, the reversal potential of the adaptation conductance (E_A) is equal to -69 mV, the subthreshold adaptation activation voltage (V_A) is equal to -43 mV, the slope of subthreshold adaptation (Δ_A) is equal to 5 mV, the time constant of adaptation (τ_A) is equal to 18 ms, and the quantal conductance (δg_A) is equal to 0.6 nS.

2.6.5 OLM cell

Oriens lacunosum moleculare (OLM) cells are also expressing the neuropeptide soM. Their somata are located in the so/alveus border, their dendrites usually form tufts in the alveus, and their axon extends into the sl-m where it ramifies heavily (**fig. 23**). Hence, OLMs inhibit the distal dendrites of the pyramidal cells (Booker & Vida, 2018). Moreover, they send synapses into other OLMs, BCs, BiCs, and VIPs (Bezaire & Soltesz, 2013)

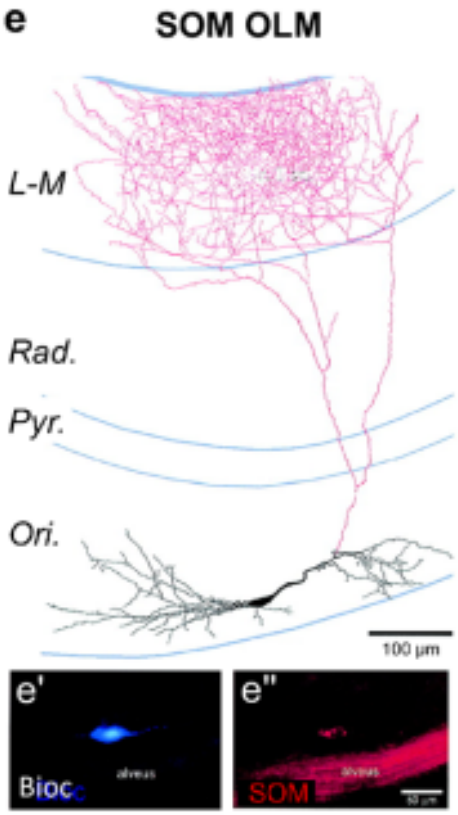

Figure 23. Example reconstruction of soM OLM. Soma and dendrites are shown as black, while the axon is shown as red. The reconstruction is shown with respect to CA1 layers: Ori, str. oriens; Pyr, str. pyramidale; Rad., str. radiatum; L-M, str. lacunosum-moleculare. (Adapted from Booker & Vida, 2018)

For the biophysical parameters of our CA network's OLMs model, we used the information from experimental works (Gloveli et al., 2005; Hilscher et al., 2019) and a database containing information about the biophysical characteristics of the hippocampal neurons (**http://hippocampome.org/php/index.php**). According to equations (**25**), (**2**), the resting membrane potential (E_L) is equal to -60 mV, the input resistance (R_{in}) is equal to ~333 MΩ, the membrane capacitance (C) is equal to 99 pF, the membrane time constant (τ_m) is equal to 33 ms, the threshold for action potential initiation (V_T) is equal to -46 mV, the reset value (V_R) is equal to -50 mV, the time-constant for the low-pass filtering of the noise (τ_{noise}) is equal to 10 ms, the noise standard deviation (σ_{noise}) is equal to 3 pA, the mean (μ_{noise}) is equal to 5 pA, and for

the adaptation of the soma the maximal subthreshold adaptation conductance ($\bar{g}_A$) is equal to -0.3 nS, the reversal potential of the adaptation conductance (E_A) is equal to -63 mV, the subthreshold adaptation activation voltage (V_A) is equal to -48mV, the slope of subthreshold adaptation (Δ_A) is equal to 5 mV, the time constant of adaptation (τ_A) is equal to 80 ms, and the quantal conductance (δg_A) is equal to 2.5 nS.

2.6.6 VIP cell

There is a big group of, calretinin (CR) and/or Vasoactive intestinal peptide (VIP) positive, interneurons whose main role is to inhibit other interneurons instead of principal cells (interneuron-specific interneurons (IS-INs)). In our model, we incorporated the IS-IN type III (VIP), which is CR^+/VIP^+ and innervates mostly, if not only, other interneurons. Their somata are located in the sp and sr, their dendrites expand in all layers forming a tuft in sl-m, and their axon ramifies exclusively in the so (**fig. 24**) (Booker & Vida, 2018).

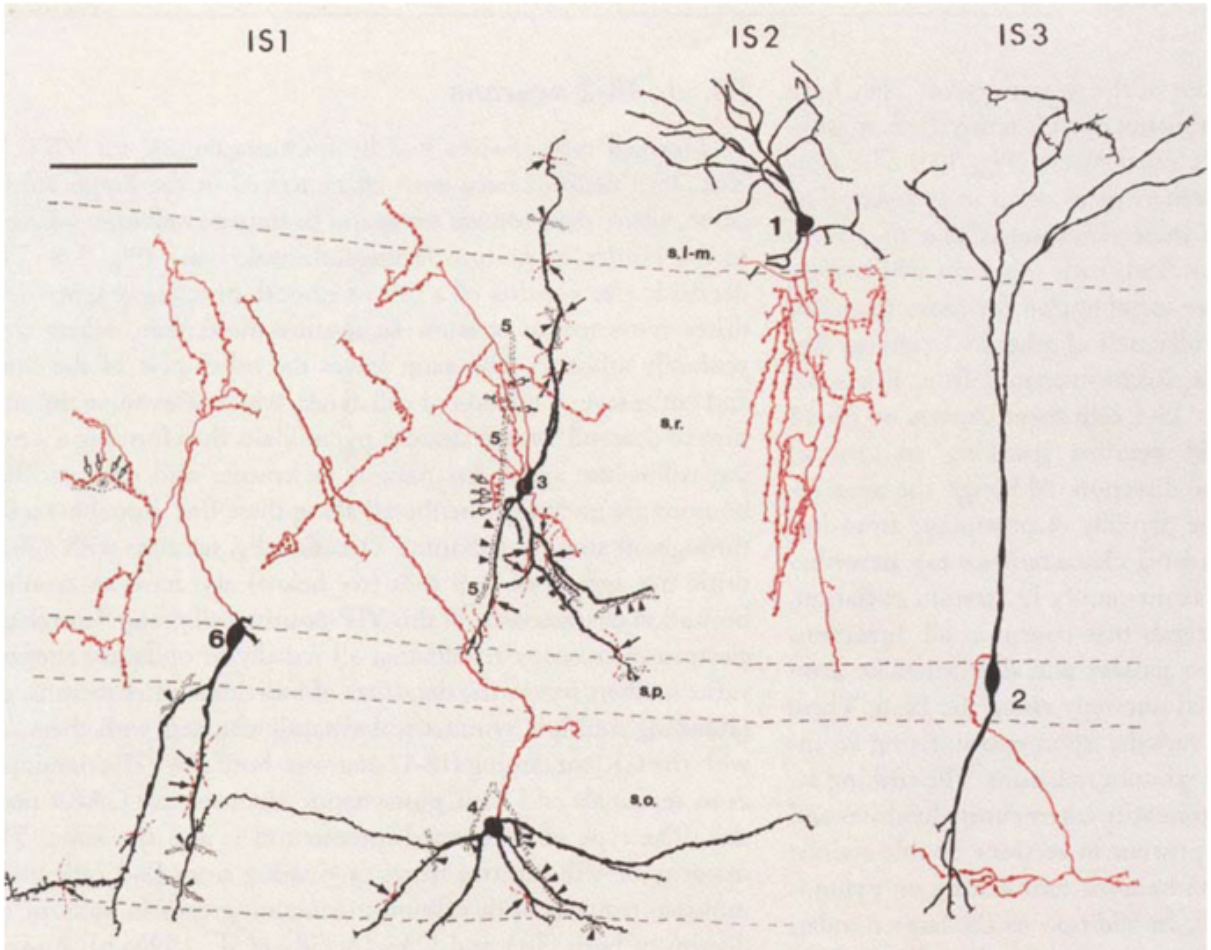

Figure 24. IN-specific INs of hippocampal subfield CA1: distribution of CR immunoreactive IS-INs with respect to the somatodendritic axis (black) and axonal arborization (red). (Source from Freund & Buzsáki, 1996)

For the biophysical parameters of our CA network's VIPs model, we used the information from experimental work (Francavilla et al., 2020) and a database containing information about the biophysical characteristics of the hippocampal neurons (**http://hippocampome.org/php/index.php**). According to equations (**25**), (**2**), the resting membrane potential (E_L) is equal to -58.1 mV, the input resistance (R_{in}) is equal to ~602 MΩ, the membrane capacitance (C) is equal to 50 pF, the membrane time constant (τ_m) is equal to 30.12 ms, the threshold for action potential initiation (V_T) is equal to -44.8 mV, the reset value (V_R) is equal to -55 mV, the time-constant for the low-pass filtering of the noise (τ_{noise}) is equal to 10 ms, the noise standard deviation (σ_{noise}) is equal to 3 pA, the mean (μ_{noise}) is equal to 5 pA, and for the adaptation of the soma the maximal subthreshold adaptation conductance ($\bar{g}_A$) is equal to -0.3 nS, the reversal potential of the adaptation conductance (E_A) is equal to -60 mV, the subthreshold adaptation activation voltage (V_A) is equal to -50mV, the slope of subthreshold adaptation (Δ_A) is equal to 10 mV, the time constant of adaptation (τ_A) is equal to 37.8 ms, and the quantal conductance (δg_A) is equal to 0.9 nS.

2.6.7 The CA1 network

In detail, 623 CA1 pyramidal cells, 66 BCs, 26 BiCs, 20 OLMs, and 15 VIPs are modeled without a specific topological organization. The CA1 pyramidals send excitatory synapses to other CA1 pyramidal's basal dendrites with a probability of 0.48%, to BCs with a probability of 5.6%, to BiCs with a probability of 4.97%, to OLMs with a probability of 31.8%, and VIPs with a probability of 18.4%. They receive inhibitory synapses to their somata from BCs with a probability of 4.6%, to their basal and oblique dendrites from BiCs with a probability of 7.68%, and their distal dendrites from OLMs with a probability of 10%. For the interconnections between the interneurons, BCs send synapses to other BCs, BiCs, and VIPs with a probability of 1.5%. BiCs inhibit other BiCs and BCs with a probability of 15.4%, OLMs with a probability of 42.3%, and VIPs with a probability of 3.84%. OLMs inhibit other OLMs with a probability of 10%, BiCs, and BCs with a probability of 15%, VIPs with a probability of 5%. Finally, VIPs inhibit BCs with a probability of 20%, and OLMs with a probability of 73.3% (Bezaire et al., 2016; Bezaire & Soltesz, 2013).

As for the input of the CA1 network, 400 EC layer III cells, to match the number of EC layer II cells, were modeled to fire with a rate of 10Hz, in the theta frequency band (López-Madrona & Canals, 2021). They contact CA1 pyramidal's distal dendrites with a probability of 18.5%, BCs with a probability of 0.75%, BiCs with a probability of 6%, and VIPs with a probability of 7.5% (Bezaire et al., 2016; Bezaire & Soltesz, 2013).

2.6.8 The CA3 network

In detail, 400 CA3 pyramidal cells are modeled into 10 lamellae of 40 cells per lamellae, to match the lamellar organization of the DG. Moreover, 44 BCs, 18 BiCs, 12 OLMs, and 10 VIPs are modeled freely in the space. The CA3 pyramidals contact other CA3 pyramidal's basal and oblique dendrites, inside the same cluster with a probability of 40%, and outside the cluster with a probability of 4% (Myers & Scharfman, 2011), BCs with a probability of 10%, BiCs with a probability of 8%, OLMs with a probability of 50%, and VIPs with a probability of 19%. They receive inhibitory synapses to their somata from BCs with a probability of 10%, to their basal and oblique dendrites from BiCs with a probability of 40%, and their distal dendrites from the OLMs that they contact (Maccaferri, 2005). For the interconnections between the interneurons, BCs send synapses to other BCs with a probability of 1.5%, BiCs with a probability of 3%, and VIPs with a probability of 2.5%. BiCs inhibit other BiCs and BCs with a probability of 16%, OLMs with a probability of 45%, and VIPs with a probability of 4%. OLMs inhibit other OLMs with a probability of 10%, BiCs, and BCs with a probability of 10%, VIPs with a probability of 8%. Finally, VIPs inhibit BCs with a probability of 20%, and OLMs with a probability of 75% (Bezaire et al., 2016; Bezaire & Soltesz, 2013).

As for the input of the CA3 network, it uses the same 400 EC layer II cells of the DG network. They contact CA3 pyramidal's distal dendrites with a probability of 4%, BCs with a probability of 1%, BiCs with a probability of 6.5%, and VIPs with a probability of 8% (Bezaire et al., 2016; Bezaire & Soltesz, 2013).

2.6.9 Networks interconnections

All the networks, except the inputs from the EC layers, connect and form the trisynaptic circuit. DG sends excitatory synapses, through the MF of GCs to the CA3 region, with one GC contacting only one pyramidal cell, and so five GCs from the same cluster will contact one pyramidal cell. Moreover, GCs contact CA3 region's BCs with a probability of 40%, BiCs with a probability of 2.5%, and OLMs with a probability of 4%. We incorporated backprojections from CA3 pyramidal neurons to MCs with a probability of 2% (Maccaferri, 2005), and each pyramidal contacts all the BCs from the same lamellae that excite it (Myers & Scharfman, 2011).

Afferents from CA3 pyramidals end up in the CA1 network exciting the pyramidal neurons but promoting the feedforward inhibition through the excitation of the interneurons. Therefore, CA3 pyramidals contacting the CA1 pyramidals with a probability of 85.5%, the CA1 BCs with a probability of 84%, the CA1 BiCs with a probability of 80.25%, the CA1 OLMs with a probability of 13.75%, and CA1 VIPs with a probability of 34.75% (Bezaire et al., 2016; Bezaire & Soltesz, 2013).

To model the distances that the signals have to travel, we incorporated synapse delays. The intraconnections of each network have a synaptic delay of 2.2 ms, while the interconnections have a synaptic delay of 6.6 ms. Synapses from EC to CA3 and CA1 have a latency of 5 ms, while EC inputs to DG have a latency of 5.5 ms (Leung et al., 1995).

2.7 LTP

According to a previous model (Myers & Scharfman, 2011), we modeled synaptic plasticity into the CA3 pyramidal neurons in the form of spike-timing-dependent plasticity (STDP) rule of a time window ± 100 ms (**fig. 25**) (Mishra et al., 2016), meaning that if there was a presynaptic spike and then during the next 100 ms a postsynaptic spike or first a postsynaptic spike and then during the next 100 ms a presynaptic spike, the synaptic strength between them increases. This leads to a bigger EPSP the next time the cell will receive input from the same source. Increasing the synaptic weight between pairs of coactive pyramidals and between coactive EC and pyramidal cells leads to the “storage mode” of the pattern. At the same time, synaptic strength decreases if these rules are not met.

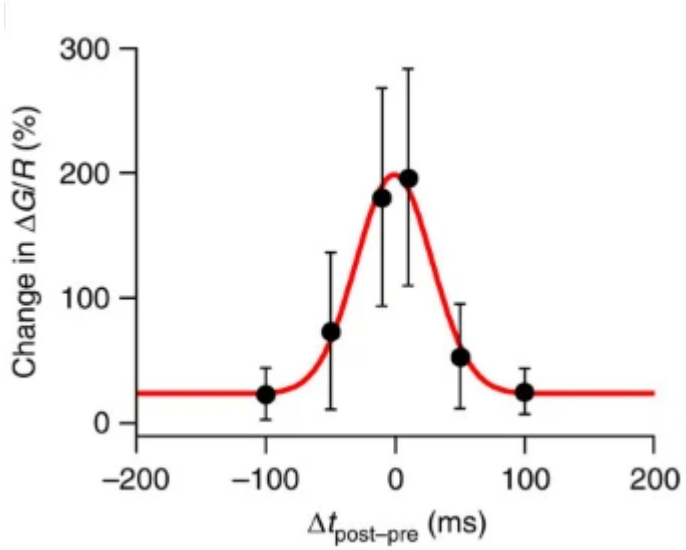

Figure 25. A broad and symmetric [Ca2+] transient summation curve in CA3 pyramidal neuron spines. Peak amplitude of [Ca2+] transients during combined pre–postsynaptic or post–presynaptic stimulation, normalized to that of isolated EPsps, was plotted against pairing time interval Δt (7 cells total). Red curve, Gaussian function with offset fit to the data points (best-fit value for offset, 23.7%). Note that the [Ca2+] transient amplitude versus pairing interval curve was broad and symmetric, similar to the STDP curve. (Adapted from Mishra et al., 2016)

3. Results

3.1 Validation of the neurons

To ensure the biological validity of our models we constrained their parameters using a broad range of mouse anatomical and electrophysiological data For the majority of modeled neurons, we successfully replicated the same experimental procedures for the Frequency-Current curves (F-I curves), Voltage-Current curves (V-I curves), or the Voltage traces after the injection of square current pulses. Furthermore, we replicated the essential dendritic properties of all principal cells.

3.1.1 Granule cell

For the GCs, we replicated in silico the experimental procedures from Mishra et al. (2020). For the V-I curve, we injected, at the soma, at resting membrane potential, square current pulses varying from -50 to +50 pA, with a 10 pA step (1000 ms duration), and recorded the voltage responses (ΔV) (**fig. 26A**). To observe the voltage trace, we injected, to the soma, a square current pulse of 250 pA for 1000 ms (**fig. 26B**), leading to a frequency of 19 Hz. For the F-I curve, we injected, to the soma, six square current pulses from 0 pA to 250 pA with a 50 pA step for 1000 ms (**fig. 26C**). All these procedures resulted in similar behavior of our model, compared with the experimental work.

GCs are characterized by their high attenuation, which is important for their sparsely firing (Krueppel et al., 2011). In our effort to replicate the experimental passive and active electrophysiological properties, we attained this feature (**fig. 27A**), however higher than the experimental (**fig. 27B & 27C**) (Kim et al., 2018). For example, we injected a current of +200 pA for 700 ms to the soma and traced the voltage responses of all the compartments. While all the other compartments felt the first spike with a time interval of 0.9 - 2.2 ms, from closer to distant compartments, the distal dendrites did not feel the first action potential of the soma (the first membrane spike of the distal dendrites was observed 26.5 ms after the first action potential).

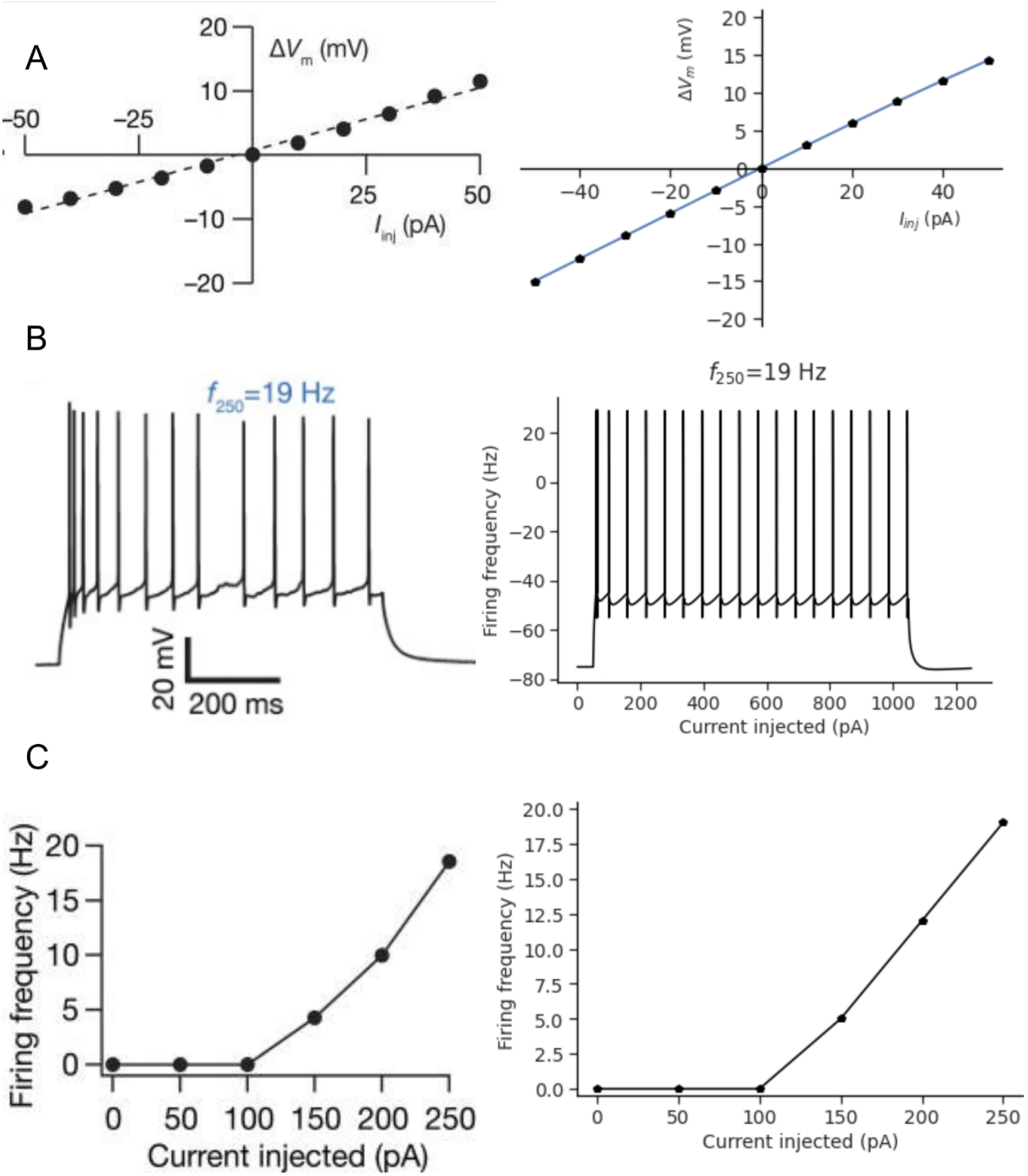

Figure 26. Active properties of GCs. A) V-I curve of a real GC(left) and our modeled GC (right). B) Voltage trace of a real GC (left) and our GC model (right) in response to somatic current injection (250 pA for 1 s). C) F-I curves of a real GC (left) and our GC model (right). (Experimental figures are adapted from Mishra & Narayanan, 2020))

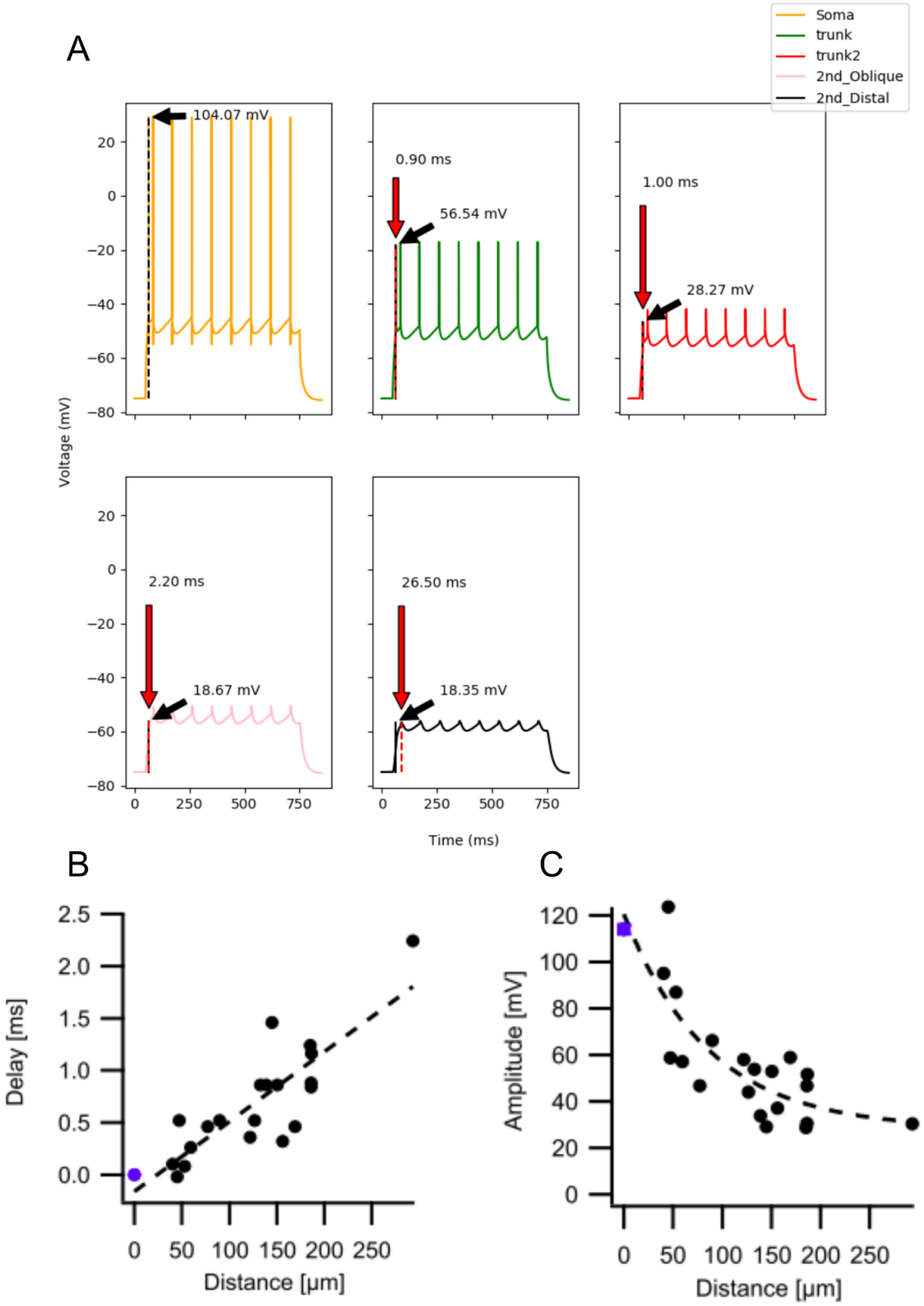

Figure 27. Attenuation of GCs. A) Backpropagation voltage traces of a GC after somatic current injection of +200 pA for 700 ms (the red arrows indicate the time of the first membrane spike, the black arrows indicate the maximum voltage of the spike from the resting membrane potential). (yellow: voltage trace of the soma, green: voltage trace of the first trunk (10 µm from the soma), red: voltage trace of the second trunk (30 µm from the soma), pink: voltage trace of one of the two oblique dendrites (100 µm from the soma), black: voltage trace of one of the two distal dendrites (200 µm from the soma)). B) Scatter plot of AP latency as a function of the distance from the soma (56 somatodendritic recordings) together with a linear regression (dashed line) to compute the average

conduction velocity of the AP into the dendrites; dendritic AP propagation velocity was 226 mm/ms.C) Scatter plot of the peak amplitude of the backpropagating AP against the absolute physical distance of the recording site from the soma (56 somatodendritic recordings). The dashed curve represents a mono-exponential fit to the data points between 0 and 212 µm. (Experimental figures adapted from (Kim et al., 2018))

3.1.2 DG basket cell

For the DG BCs, we used the experimental procedures from the work of Lübke et al. (1998). For the V-I curve, we performed a current injection of -100 to +220 pA with a step of 20 pA for 1000 ms, into a resting state BCs (**fig. 28A**). Due to limitations of the CAdEx model, while injecting +220 pA into a BC, we achieved the same firing frequency although the timing of spikes was not identical to the experimental trace(**fig. 28B**).

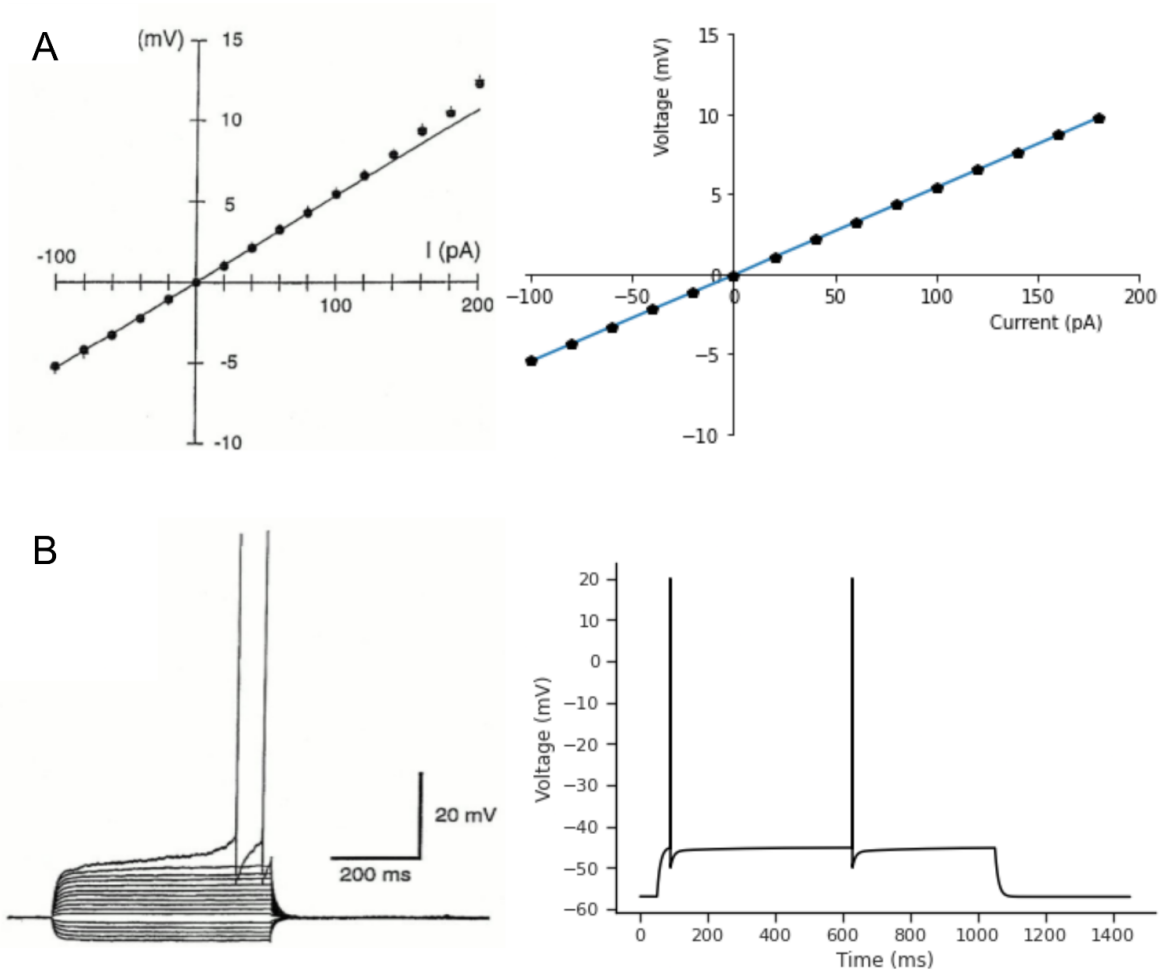

Figure 28. Active electrophysiological properties of DG BCs. A) V-I curve to current injections of −100 to +220 pA in 20-pA increments. B) Voltage response to +220 pA current injection. (real BC (left) and our model (right)). (Experimental figures adapted from Lübke et al., 1998)

3.1.3 HIPP cell

The validation of active properties for our HIPP model was based on the work of Yuan et al. (2017). We first injected a +300 pA square current pulse for 1000 ms into our HIPP model and observed similar activity with the experimental measurement (**fig. 29A**). After that, we injected square current pulses varying from 0 to +500 pA with 100 pA increments, to examine the max action potential frequency in each pulse, and found similar activity with real HIPP cells at +500 pA (**fig. 29B**).

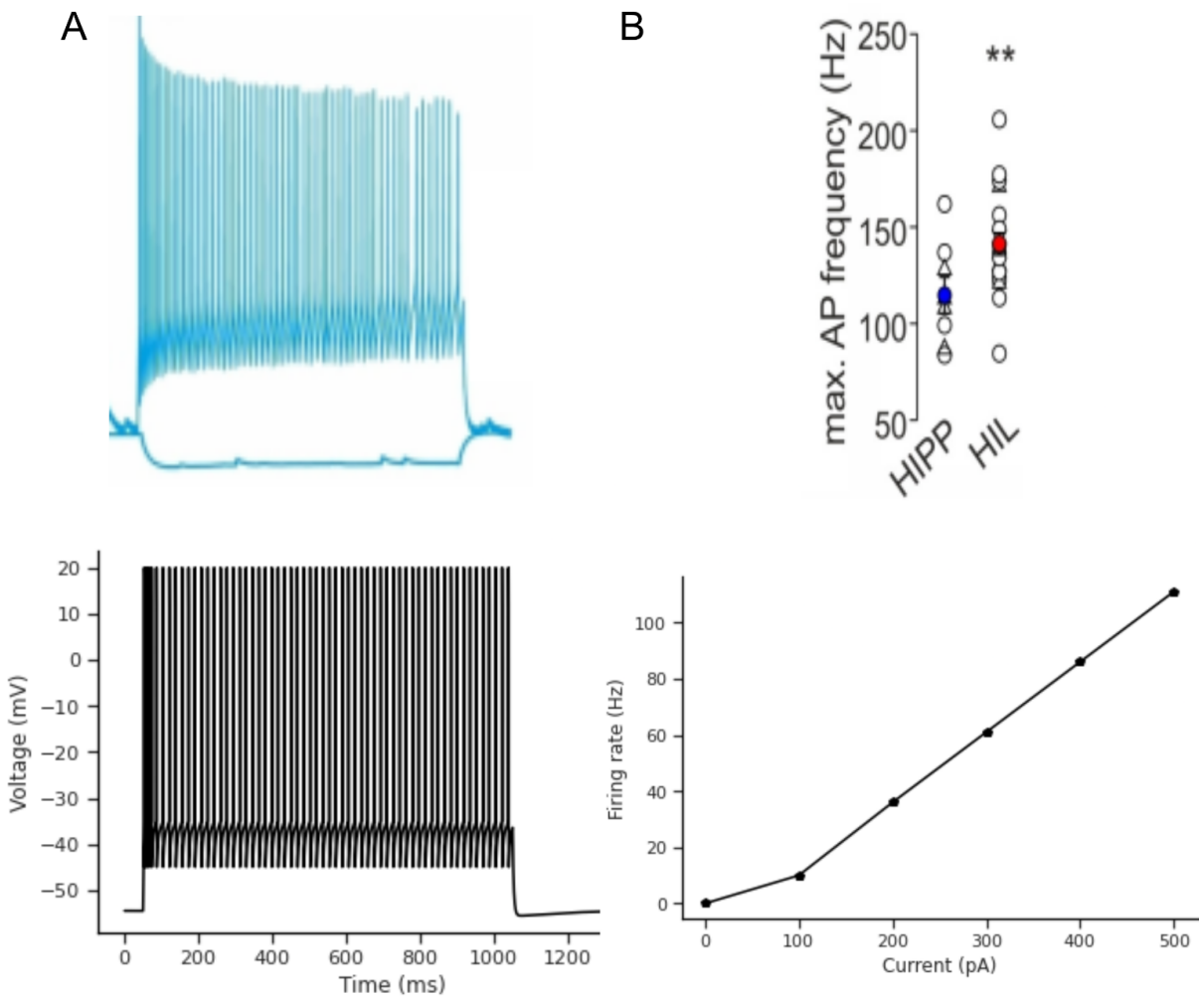

Figure 29. Validation of the active properties of our HIPP model. A) Voltage response at +300 pA current injection for 1 s. B) Max action potential (AP) frequency at +500 pA (top) and 0 to +500 pA with a 100 pA step (bottom) current injection. (Top a real HIPP cell and bottom our model). (Experimental figures adapted from Yuan et al., 2017)

3.1.4 Mossy cell

For our MC model, we used again the work of Lübke et al. (1998). Firstly, we injected -150 to +100 pA with a 5 pA increment square current pulses for 1000 ms and observed similar responses to real MCs (**fig. 30A**). Then, we injected a square current pulse of +150 pA for 1000 ms into a resting MC. We achieved the same

number of spikes (3 APs) as in the experimental results, but we experienced the same limitation of the CAdEx model in our DG BC model, we could not replicate the late response (**fig. 30B**). However, the MC model had a similar response to experimental results with a 1000 pA current injection (**fig. 30B**).

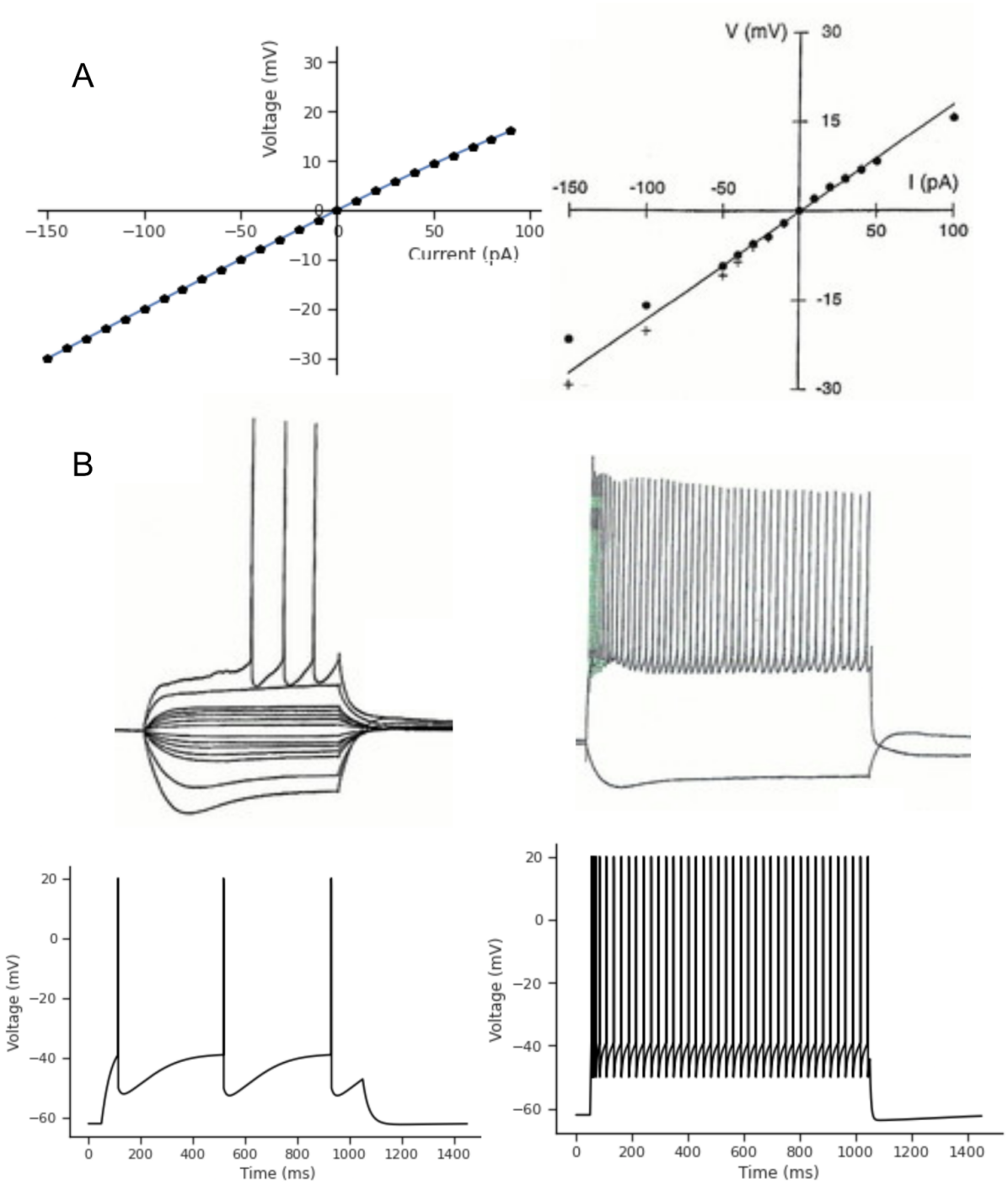

Figure 30. Validation of active properties for our mossy cell (MC) model. A) V-I curve to current injections of −100 to +220 pA in 20-pA increments for our model (left) and current injections of −150 to +150 pA in 50-pA increments and −40 to +40 pA in 10-pA increments for real MC (right). B) Voltage responses to current injection of +150 pA for real MC (top left) and our model (bottom left), and to current injection of +1000 pA for real MC (top right) and

our model (bottom right). The time of each current injection was 1 s. (Experimental figures adapted from Lübke et al., 1998)

3.1.5 CA basket cell

For our CA BC model, we replicated the experimental procedures from the work of Papp et al. (2013). We injected square current pulses of +100, +150, +200, and +600 pA to examine the max action potential frequency in each pulse, and found similar activity with real BCs at +600 pA (**fig. 31A**). We traced the voltage responses to current injections of +200 and +600 pA for 800 ms (**fig. 31B**). Again, the same limitation of the CAdEx model was observed. We could not replicate the late response of APs, which led our model to miss the accumulated APs at the end of the current injection.

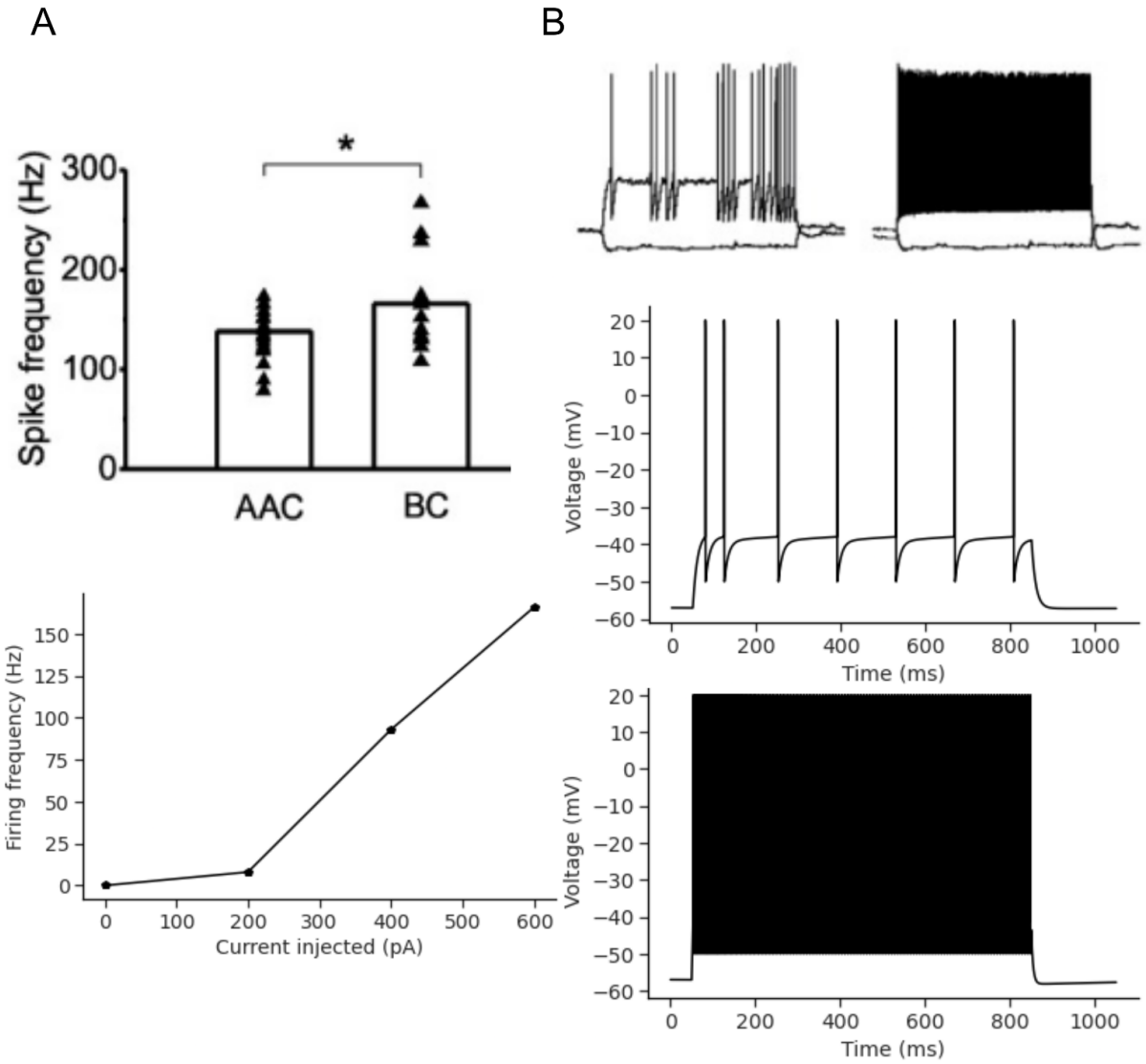

Figure 31. Validation of the active properties of our CA BC model. A) Max action potential (AP) frequency at +600 pA (top) and +100, +150, +200, and +600 pA (bottom) current injection. B) Voltage responses to current injection of +200 (top left) and +600 pA (top right),

for 800 ms. (Top a real CA BC cell and bottom our model). (Experimental figures adapted from Papp et al., 2013)

3.1.6 Bistratified cell

BiCs have a steep change to their maximum firing rates from their rheobase (**fig. 32A**). We observed that phenomenon trying to compare the maximum frequency of our model to real BiCs, using square current injections of 0 to +400 pA with 1 pA increment. Then, we injected +350 pA current for 1000 ms into a resting BiC and compared its voltage trace to another model and a real BiC (**fig. 32B**). For the comparisons, we used the results from the work of Bezaire et al. (2016).

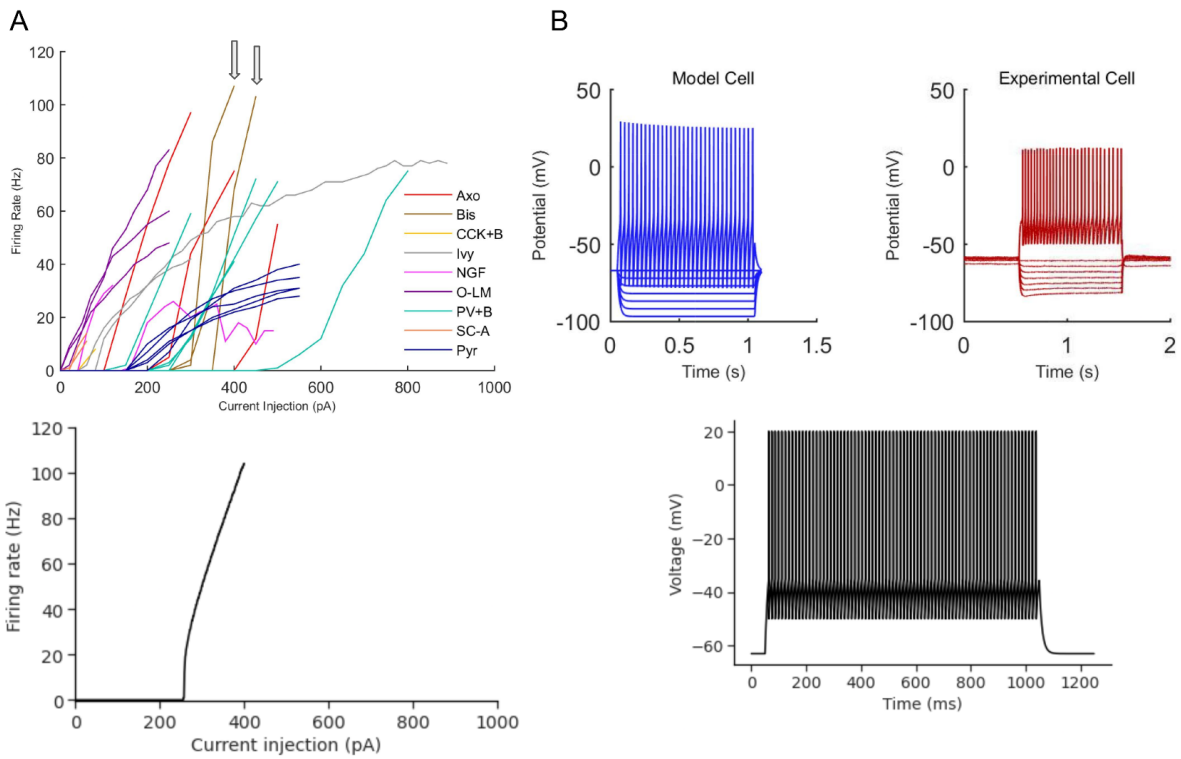

Figure 32. Validation of the active properties of our BiC model. A) Firing rate of experimental BiCs (top, indicated by the arrows) and our model (bottom). B) Voltage responses to current injection of +350 pA for 1 s, of another model (Bezaire et al., 2016) (top left), a real BiC (top right), and our model (bottom). (Experimental figures adapted from Bezaire et al., 2016)

3.1.7 OLM

For our OLM model, we replicated the experimental procedures from the work of Gloveli et al. (2005). First, we injected a +300 pA current for 500 ms and observed a similar bursting at the beginning of the injection (**fig. 33A**). Then, we evaluated the max firing rates for current injections of +100 to +600 pA with a 100 pA increment and got similar results (**fig. 33B**). Lastly, we made the V-I curve with current injections of -200 to +40 pA with a 20 pA increment for 800 ms (**fig. 33C**). For the

currents -140 pA and more positive we had similar activity, but for more negative currents than -140 pA, our model reached more negative membrane potentials.

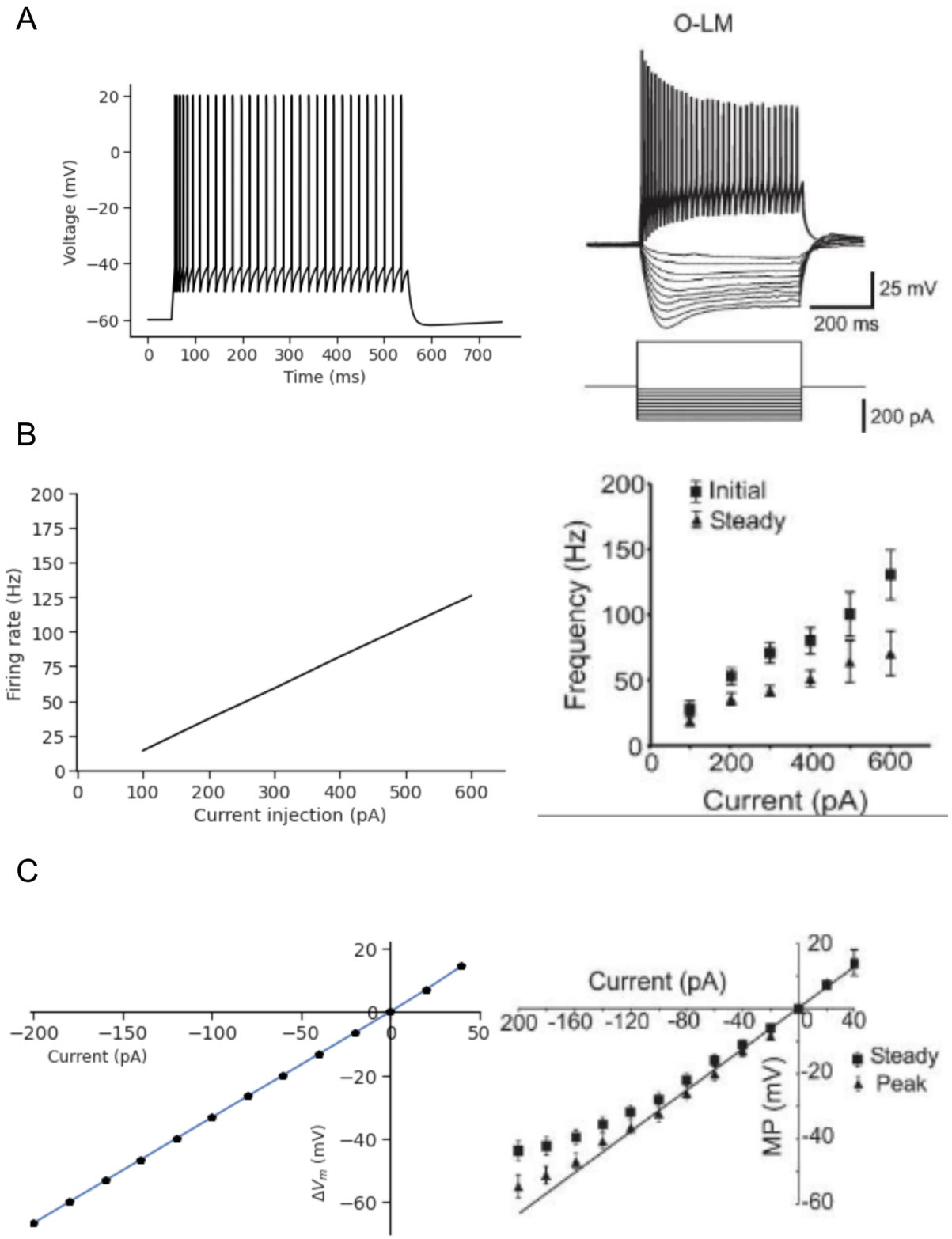

Figure 33. Validation of the active properties of our OLM model. A) Voltage responses to current injection of +300 pA for 500 ms. B) Max action potential (AP) frequency to current injections of +100 to +600 pA with a step of 100 pA. C) V-I curve of current injections of −200

to +40 pA in 20-pA increments. (Left are the results of our model; Right are the results of experimental OLMs) (Experimental figures adapted from Gloveli et al., 2005)

3.1.8 VIP

We tried to replicate the active properties of our VIP model according to experimental results for VIP cells from young mice from the work of Francavilla et al. (2020). First, we injected four currents of 19, 20, 40, and 140 pA to evaluate the rheobase current and the maximum frequency at 140 pA (**fig. 34A**). Then, we injected currents of 20 (rheobase) and 40 pA for 1000 ms to track the voltage traces (**fig. 34B**), and we got similar results to experimental.

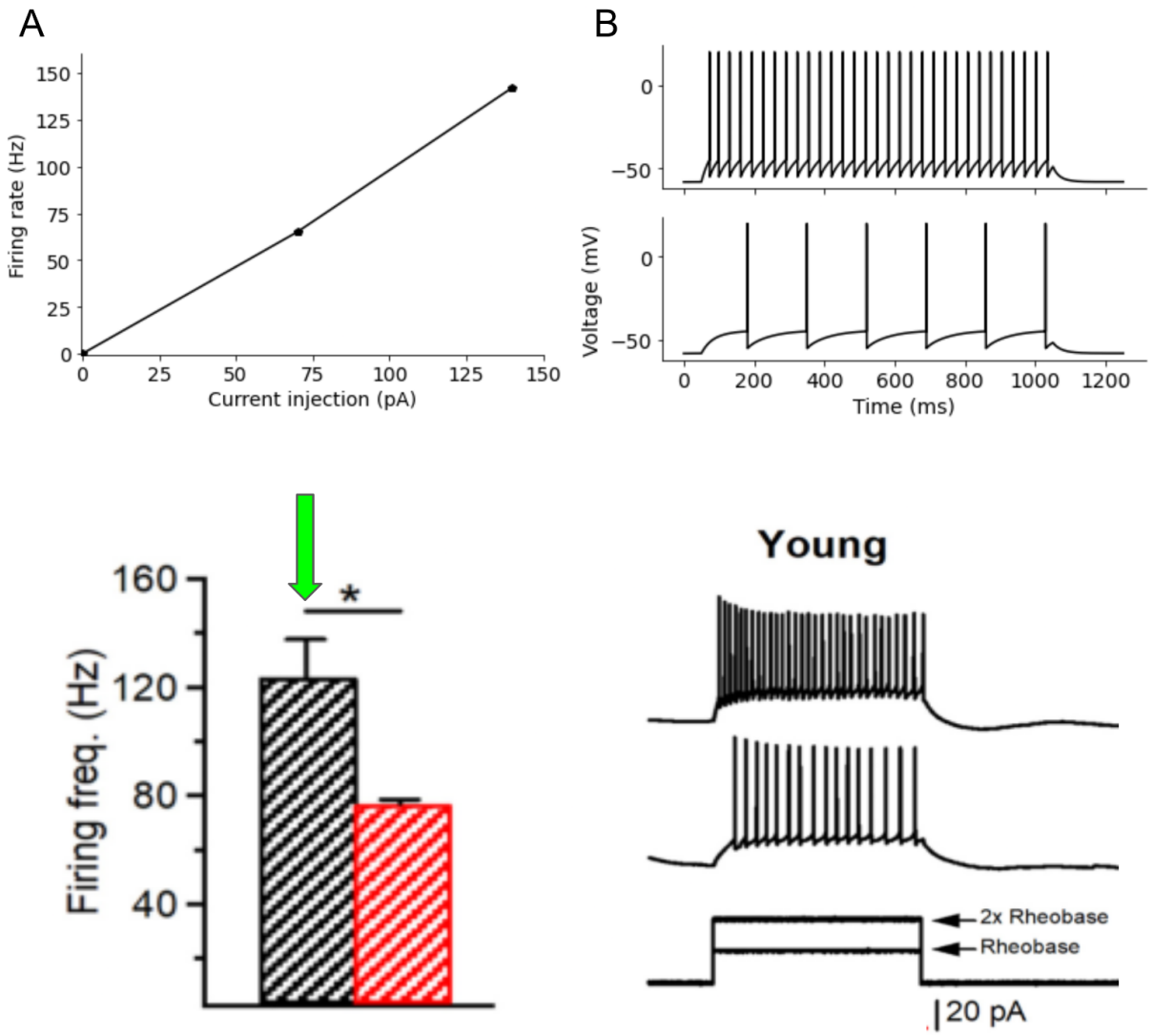

Figure 34. Validation of the active properties of our VIP model. A) F-I curve for current injections of +70 and +140 pA (top) and only +140 pA (bottom) (the green arrow indicates VIP neurons in young mice, while the red bar is for old mice). B) Representative voltage responses indicating the firing pattern of VIP cells in young mice in response to depolarizing (+20 pA and +40 pA) current injections corresponding to rheobase and 2x rheobase current, respectively. Scale bar: 20 pA (Top: our model; Bottom: real VIP) (Experimental figures adapted from Francavilla et al., 2020)

3.1.9 CA1 pyramidal cell

Masurkar et al. (2020) showed that CA1 pyramidal neurons have different electrophysiological properties depending on their position, deep or superficial, in the CA1 region. We tried to model an average of these properties because we did not incorporate topological details in our networks. Firstly, we injected +350 pA current for 1000 ms to get the voltage trace and it looked similar to the experimental one (**fig. 35A**). Then, we made a firing frequency-input current (F-I) curve by injecting currents from +100 to +350 pA with a step of 50 pA and we matched the F-I of the CA1b deep pyramidals (**fig. 35B**). Moreover, we validated the NMDA and AMPA channels to achieve the suprathreshold activity of the dendrites (**fig. 36**) (Harnett et al., 2012). For this reason, we simulated excitatory synapses, into the dendrites, varying from 0 to 25 synapses.

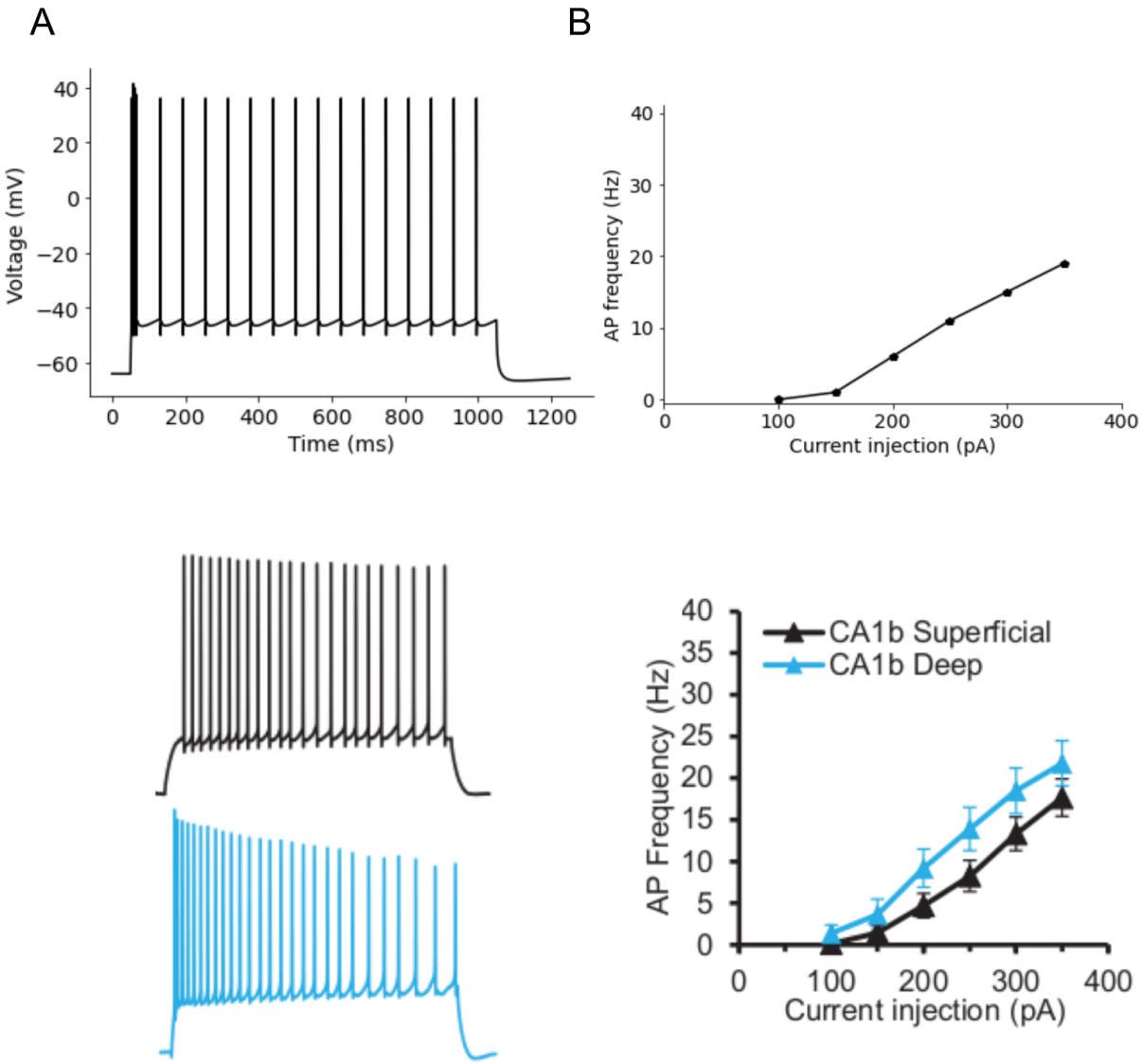

Figure 35. Validation of the active properties of our CA1 pyramidal model. A) Example of voltage trace by a +350 pA, 1 s current injection. B) Firing frequency-input current (F-I) curves by giving a range of current injections from +100 to +350 pA with 50 pA increments.

(Top: our model; Bottom: real CA1 pyramidal cell; In experimental figures with black is the superficial pyramidal and with blue the deep pyramidal cell) (Experimental figures adapted from Masurkar et al. 2020)

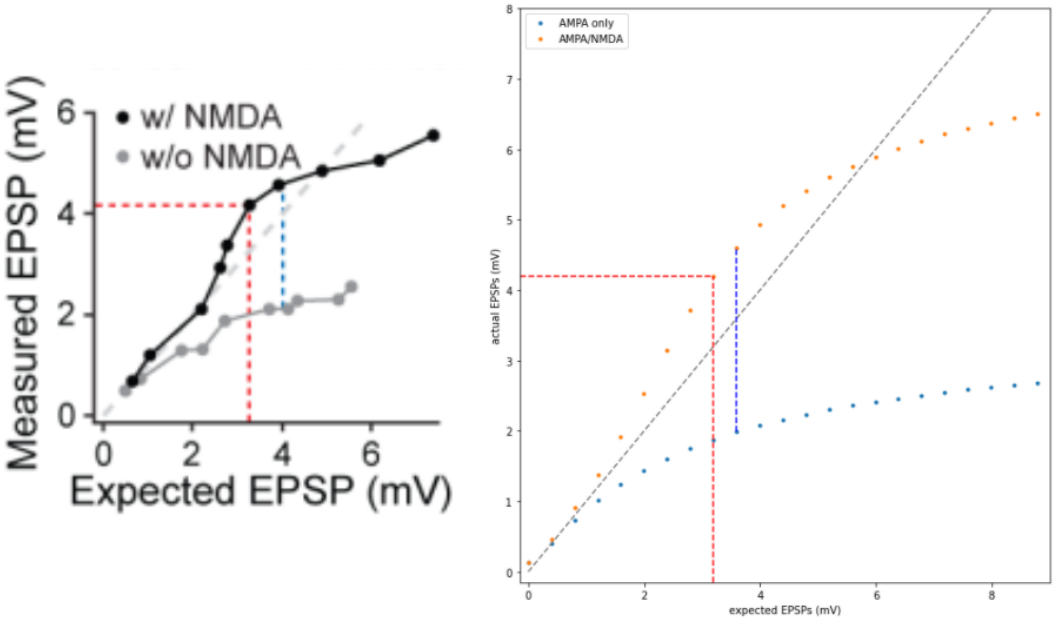

Figure 36. The effect of NMDARs on signal integration. Expected vs measured EPsp plot for increasing numbers of synapses under control conditions (black & orange) and without the NMDARs (grey & blue). The grey dashed lines indicate unity. (Left: experimental; Right: our model) (Experimental figure adapted from Harnettet al., 2012)

3.1.10 CA3 pyramidal cell

Similar to the CA1 region's pyramidal cells, Sun et al. (2017) and Sun et al. (2020) showed that across the transverse (proximodistal) and longitudinal (dorsoventral) axis of the hippocampus, CA3 pyramidal neurons differed from each other in their morphology and intrinsic membrane properties. Therefore, we tried to model a CA3 pyramidal neuron using the average of the passive and active biophysical properties. To compare our model with the experimental results, we injected four different currents into the somata of resting cells and observed similar behavior, especially the bursting in the beginning, to mid-CA3 region (CA3b) along the transverse axis (**fig. 37A**). Then, we injected currents to make a firing frequency-input current curve by injecting different current amplitudes, and, once again, we observed a similar curve to CA3b pyramidal neurons (**fig. 37B**).

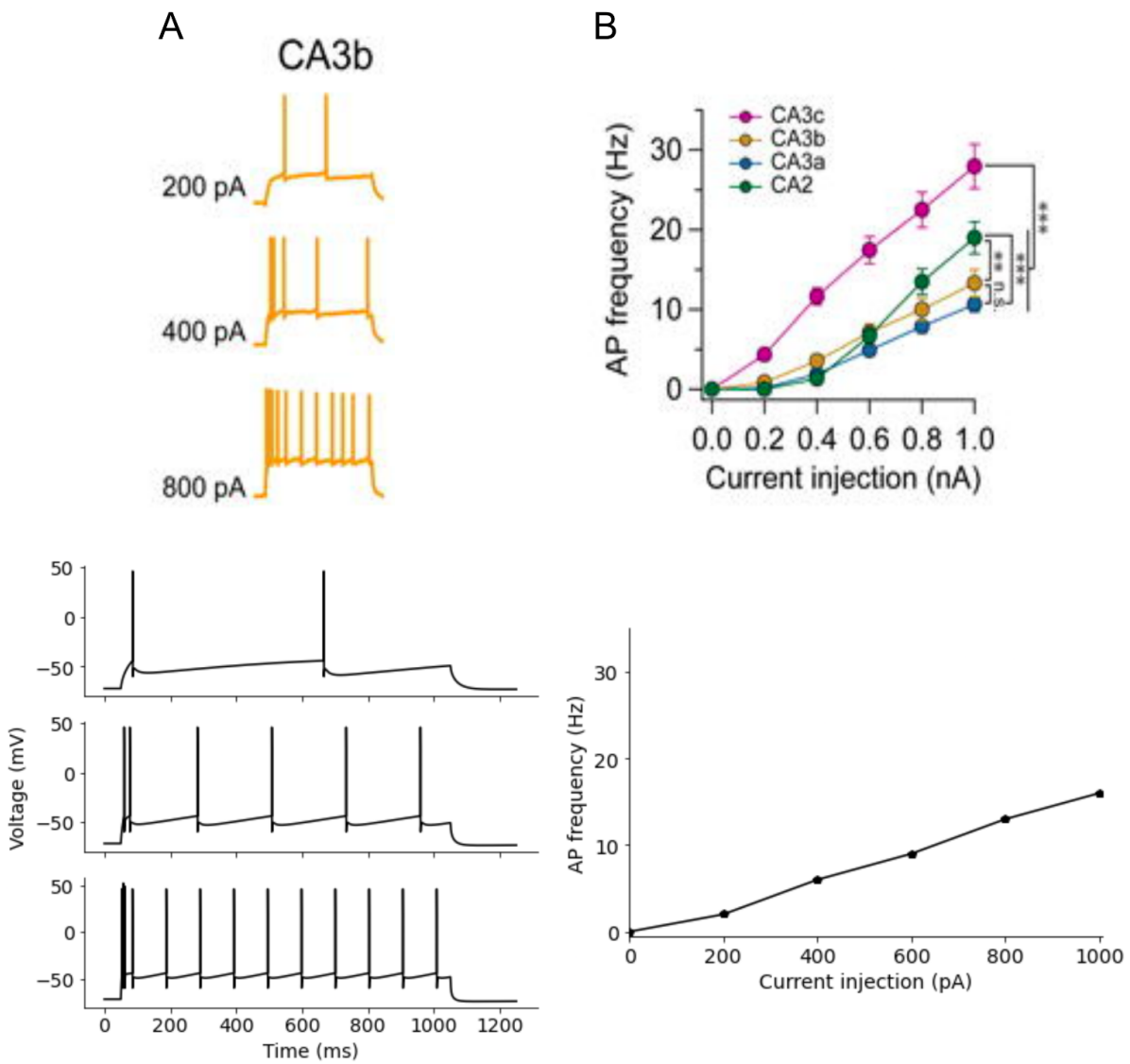

Figure 37. Validation of the active properties of our CA3 pyramidal model. A) Example of voltage traces by a +200 pA (top subplots), +400 pA (mid subplots), and +800 pA (bottom subplots), 1 s current injection. B) Firing frequency-input current (F-I) curves by giving a range of current injections from 0 to 1000 pA with 100-pA increments (top: real CA3 pyramidal cell; bottom: our model (Experimental figures adapted from Sun et al., 2017)

Then, we tried to validate, according to the computational work of Humphries et al. (2021), the NMDA and AMPA channels so the dendrites could acquire their supra- or sub-threshold activity (**fig. 38**). Lastly, we tried to validate the sodium (Na^+) spikes of the dendrites (**fig. 39**) (Kim et al., 2012) because they are necessary for signal transmission from the dendrites to soma and backpropagation properties of action potentials from the soma to dendrites.

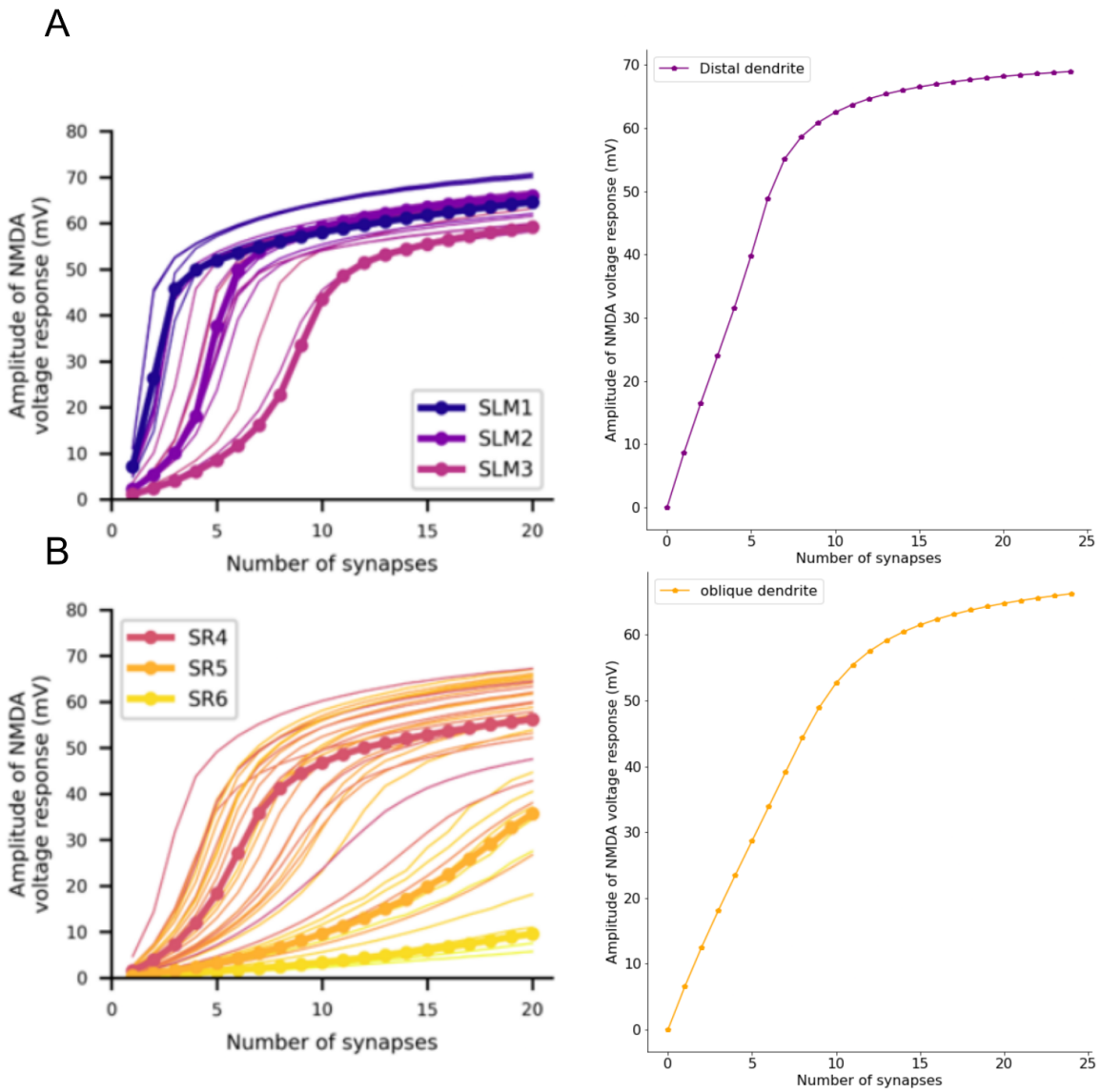

Figure 38. Nonlinearity plots from distal (sl-m) and oblique (sr) dendrites. The amplitude of NMDA voltage responses for different numbers of synapses. A) sl-m dendrites of the exemplar model (left) and our model (right). (B) sr dendrites of the exemplar model (left) and our model (right). (Experimental figures adapted from Humphries et al., 2021)

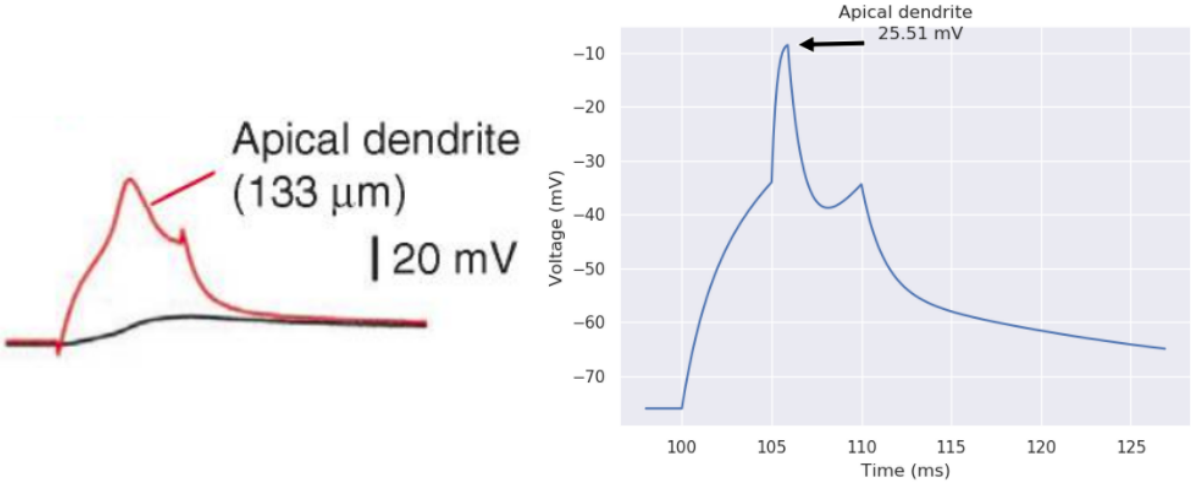

Figure 39. Examples of a dendritic spike in CA3 pyramidal neurons (left) and our model (right). The black arrow indicates the difference of membrane voltage from the spike threshold (-36 mV) (Experimental figure adapted from Kim et al., 2012)

3.2 Validation of the networks

3.2.1 Pattern separation and pattern completion

After all the validations for the passive and active properties of our neuron models, the next step was to build the sub-networks (DG, CA3, and CA1) and to validate them. As the initiator of the trisynaptic circuit, DG was the first network we tried to assemble. Using 5 different random connectivities and 50 different EC inputs (400 EC cells with only 40 cells active) for each, we saw that our model could be applied to empirical data from Leutgeb et al. (2007) and model data from Myers and Scharfman (2009). For each input, we performed 7 trials, with each trial having a 10% different input from the previous one (we changed 4 cells out of the active 40). Then, to assess pattern separation, we calculated the Hamming distance (HD) between the original input I_0 and one of the trials I_x. HD is a good metric to quantify the overlap of two output patterns. The HD between two input patterns, I_x and I_y, is defined as the number of mismatching elements in I_x versus I_y. We calculated the average HD, normalized as a percent of the total number of elements in each pattern E, across the entire set of N trials using the equation (**26**), so we could compare across pattern sets with different values for E.

$$\mathrm{HD} = \frac{\sum_{x \neq y} |I_x - I_y|}{E^* \left(\frac{N^*(N-1)}{2} \right)} \times 100 \quad (26)$$

For the DG network's output, we used the activity of the GCs. We observed a better pattern separation compared to the model of Myers and Scharfman (2009) (**fig. 40**).

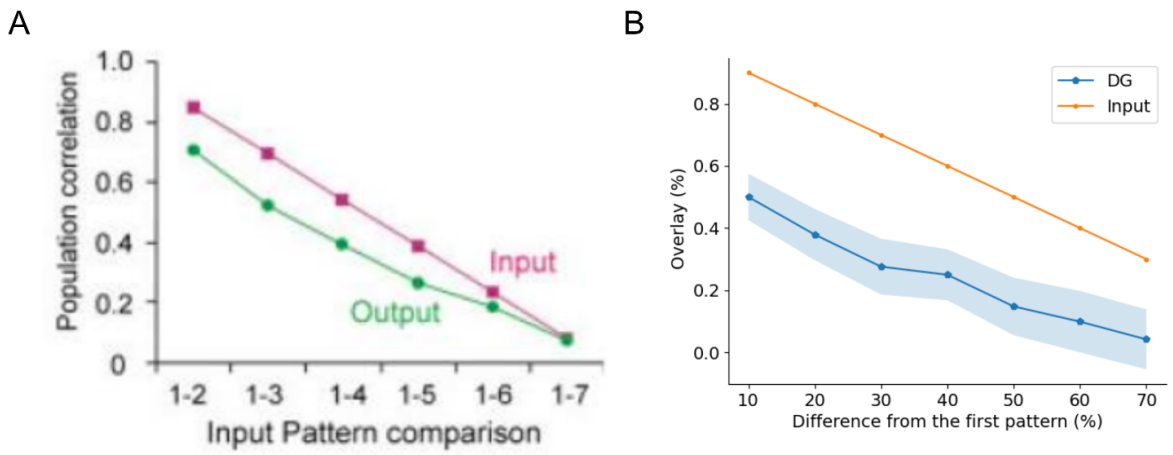

Figure 40. A) Population responses from dentate GCs in the Myers and Scharfman model ("Output") also show reduced correlation for neighboring stimuli, compared with correlations that exist in the input patterns ("Input") (Adapted from Myers & Scharfman, 2009). B) Comparison between input ("Input") and output ("DG") of our model. For the output, the dots are the mean from all 250 simulations and the shadow is the standard deviation

After we saw that our DG model can achieve pattern separation, we moved on to the CA3 network's modeling. We used the same references as DG, and we tried to assess the network's ability of separation and completion. We used the same EC inputs and our DG network's output for each one of these inputs. For the separation, we used the same protocol as in the DG, but for the pattern completion, instead of changing the input by 10%, we deleted randomly 10% of the total EC activity in each trial. Then we calculated the HD of the DG and CA3 output (GCs and CA3 pyramidals activity, respectively) in the same way as before. We even compared the effect of the presence (backprojection model) to the absence (standard model) of backprojection in our network. We observed that our CA3 model was able to perform pattern separation, but not to the same extent as in the experimental data or the Myers and Scharfman model (**fig. 41**). However, our model with backprojection caught the strong decrease in population correlation between the initial input and the next one with the 10% difference in activity (**fig. 41C**).

For the completion, we compared the activity of our standard and backprojection models to Myers and Scharfman model (**fig. 42**). At the same time, we assessed the effect of plasticity on the network's ability of pattern completion. In both standard and backprojection models, the presence of the LTP improved significantly the ability of pattern completion (**fig. 42B-C**). Backprojection improved our network's ability of pattern completion, following the Myers and Scharfman model (**fig. 43**)

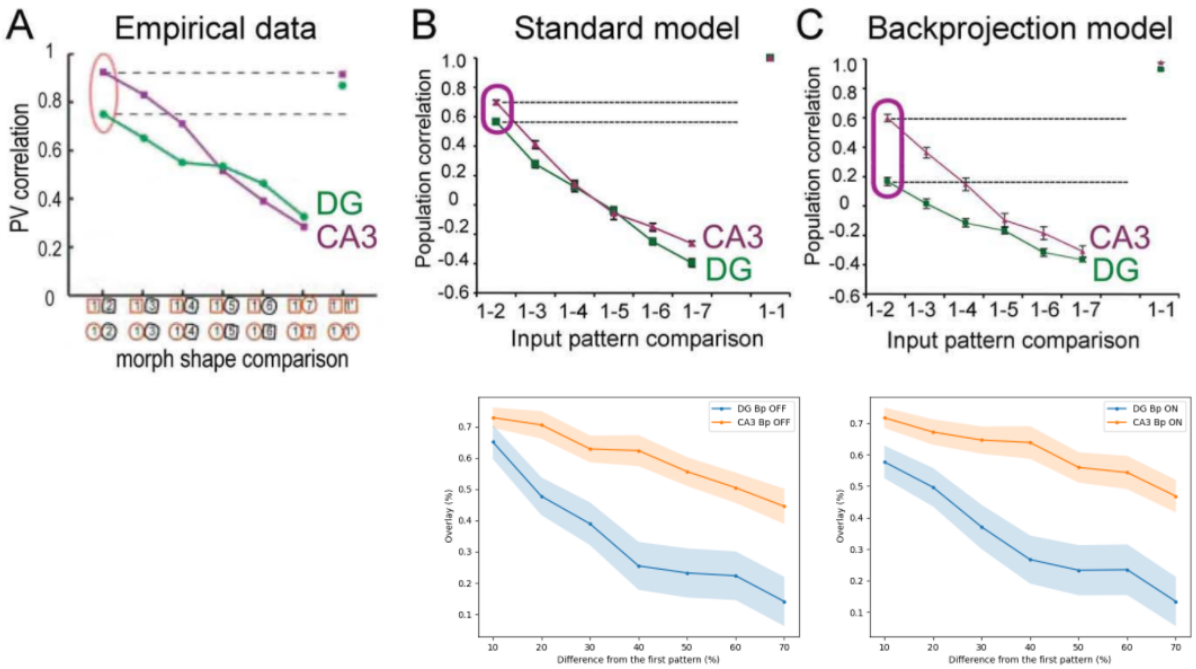

Figure 41. A) In vivo, rodents that were exposed to progressively ‘‘morphed’’ environments 1 to 7, as described in Figure 6, were evaluated with electrodes in CA3 or the DG. CA3 pyramidal neurons showed a smooth decline in population correlation as environments gradually changed. In contrast, there was a much lower population correlation for presumed dentate GCs for environments that were similar. (Adapted from Leutgeb et al., 2007) B) Pattern separation in the standard model, without backprojection. In both Myers and Scharfman model and our model the population correlation in the first trial is similar between CA3 and DG, which is inconsistent with the empirical data in A). C) In the backprojection models, the population correlation for the first trial decreased in DG, similar to empirical data in A). We had slight differences for the other trials. (B and C top figures are adapted from Myers and Scharfman, 2011)

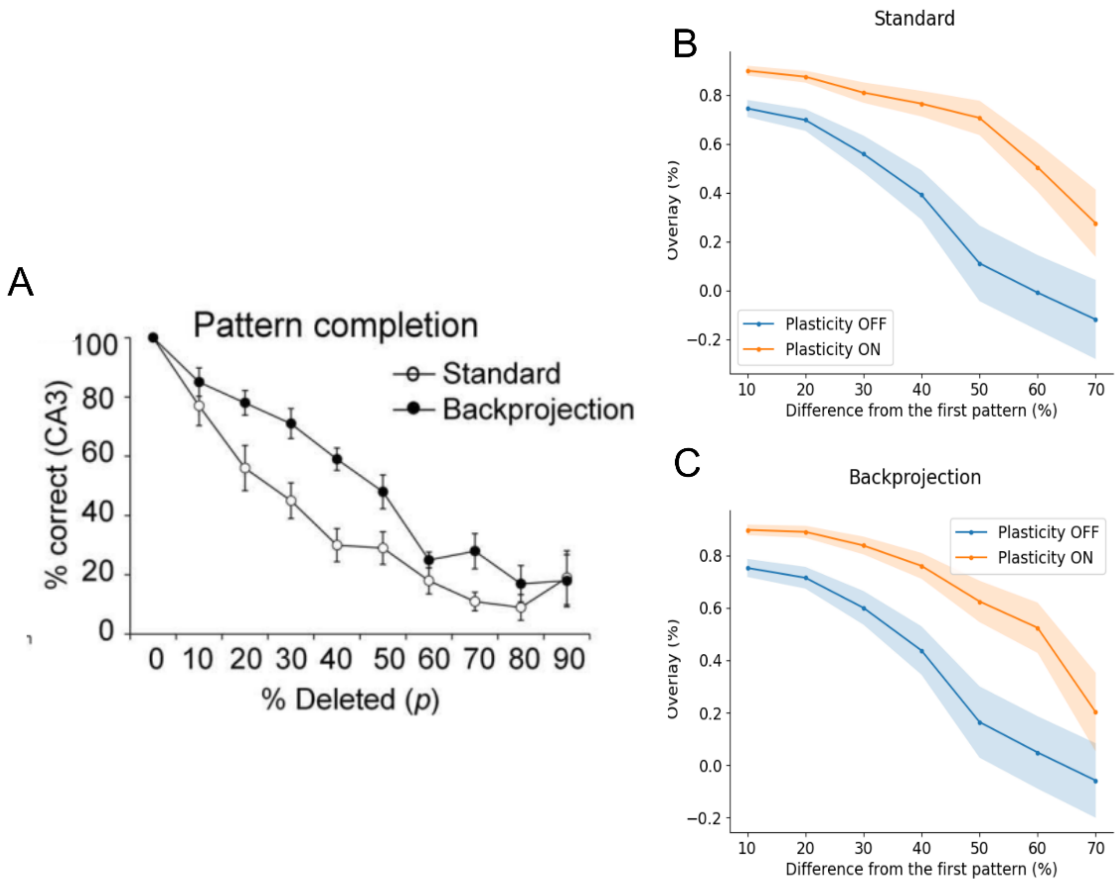

Figure 42. A)The backprojection model is better than the standard model at retrieving progressively more distorted versions of the inputs. (Adapted from Myers and Scharfman, 2011) B) & C) The presence of plasticity improved the pattern completion in both standard B) and backprojection C) model.

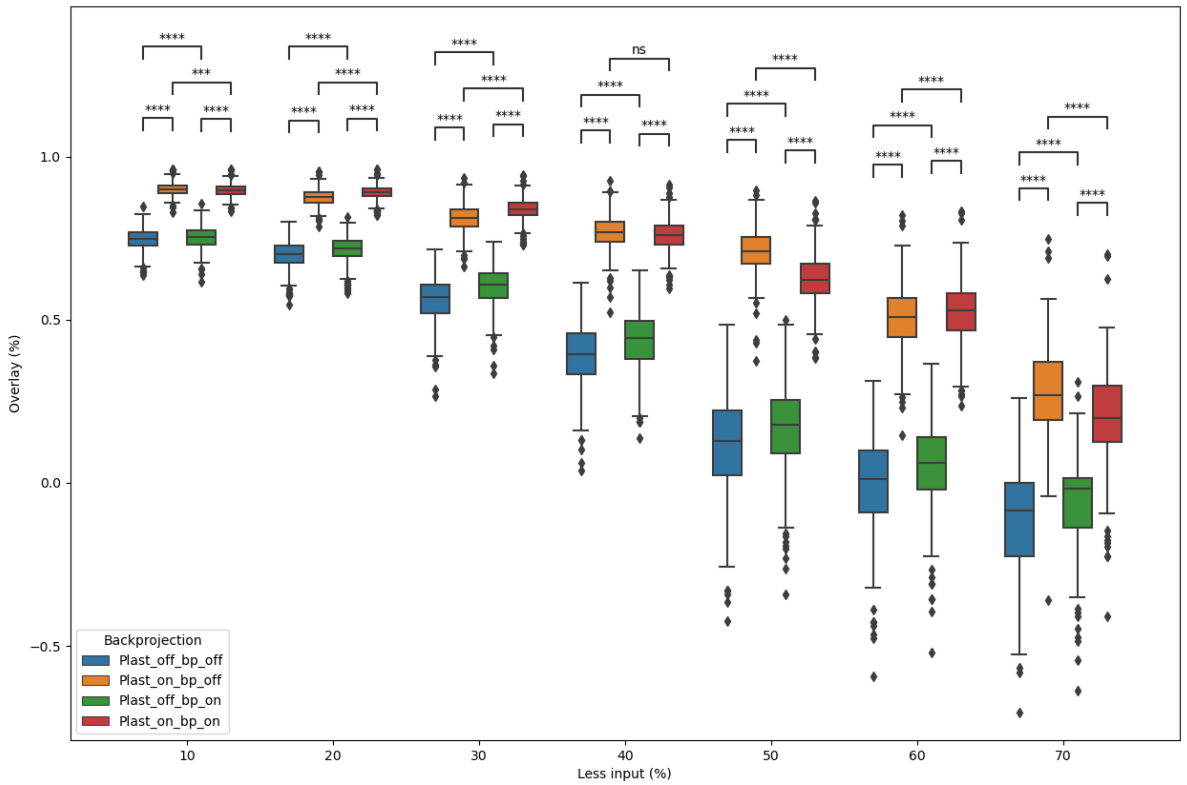

Figure 43. Comparison of our model's ability of pattern completion between different variations. The presence of plasticity and backprojection improve the pattern completion. (Blue color: no plasticity and no backprojection; Orange: with plasticity and no backprojection; Green: no plasticity and with backprojection; Red: with plasticity and with backprojection) For each comparison, we performed paired t-test with Bonferroni correction. All the 4-star are for p<<0.0001.

3.2.2 CA1 place cells

After we have built a good representative DG-CA3 model, that can accomplish pattern separation and pattern completion, we ought to model the CA1 network. We used the work of Turi et al. (2019) to compare our network's activity and ability to form place cells. For that, we simulated inputs from a mouse running in a linear track for 1 meter with constant speed, using octal of grid-like inputs from EC layer III and octal from CA3 pyramidal cells (here we did not use our CA3 model as input because we did not have the information to make EC layer II inputs so that our CA3 model would have grid-like output). We the inputs into a specific group of ~20% of the total pyramidals (120 cells), and to simulate network noise, we gave the whole input into a random 20% of the pyramidals. We observed place cells in our network, so we assessed the role of inhibition on its activity by simulating without (**fig. 44**) or with inhibition (**fig. 45**). The presence of inhibition decreased a lot the activity of non-place cells, "network noise", and the offset firings of the place cells. We got similar results to those of Turi et al. (2019), but not the same image because the inputs were designed for a smaller network (130 pyramidal cells) (**fig. 45**)

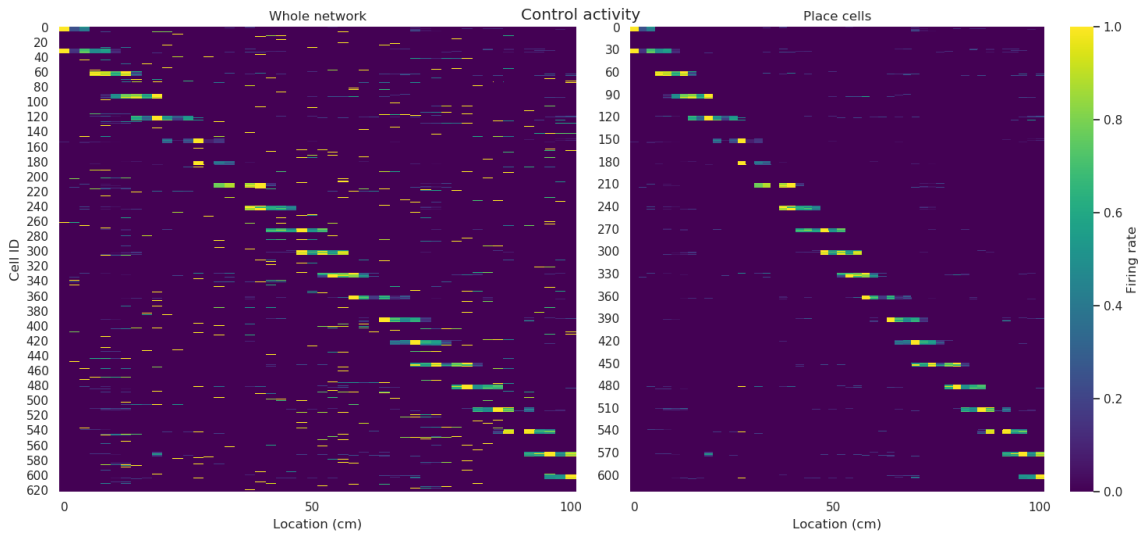

Figure 44. CA1 pyramidals activity without inhibition, for the whole network (left) and place cells (right), normalized.

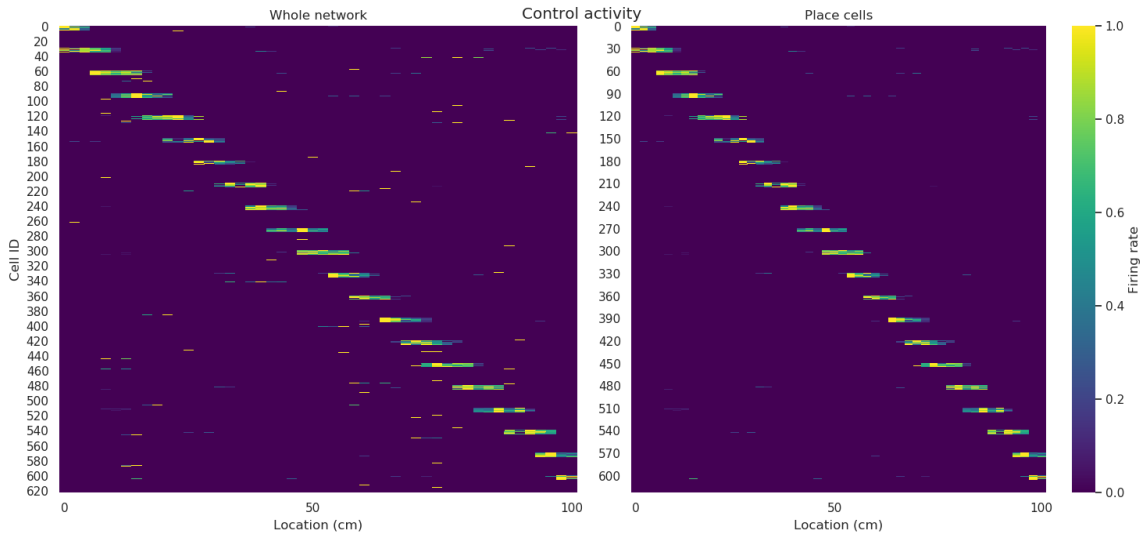

Figure 44. CA1 pyramidals activity with inhibition, for the whole network (left) and place cells (right), normalized

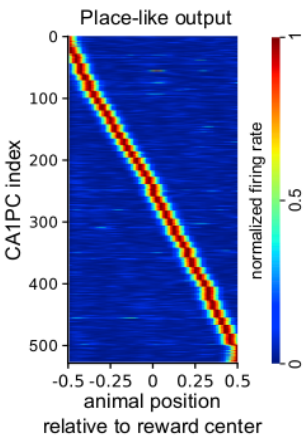

Figure 45. CA1PC activity before learning (Adapted from Turi et al., 2019)

3.2.3 The network

With all these validations done, we combined all three networks, DG, CA3, and CA1. We used the inputs as described in **Methods** and run each simulation for 1500 ms. We observed that despite the randomness and frequency of our inputs for both DG-CA3 (40 Hz) and CA1 (10 Hz) network, our hippocampus model transformed them into an activity in the theta (4-8 Hz) frequency band (**fig. 46**) (Buzsáki, 2002).

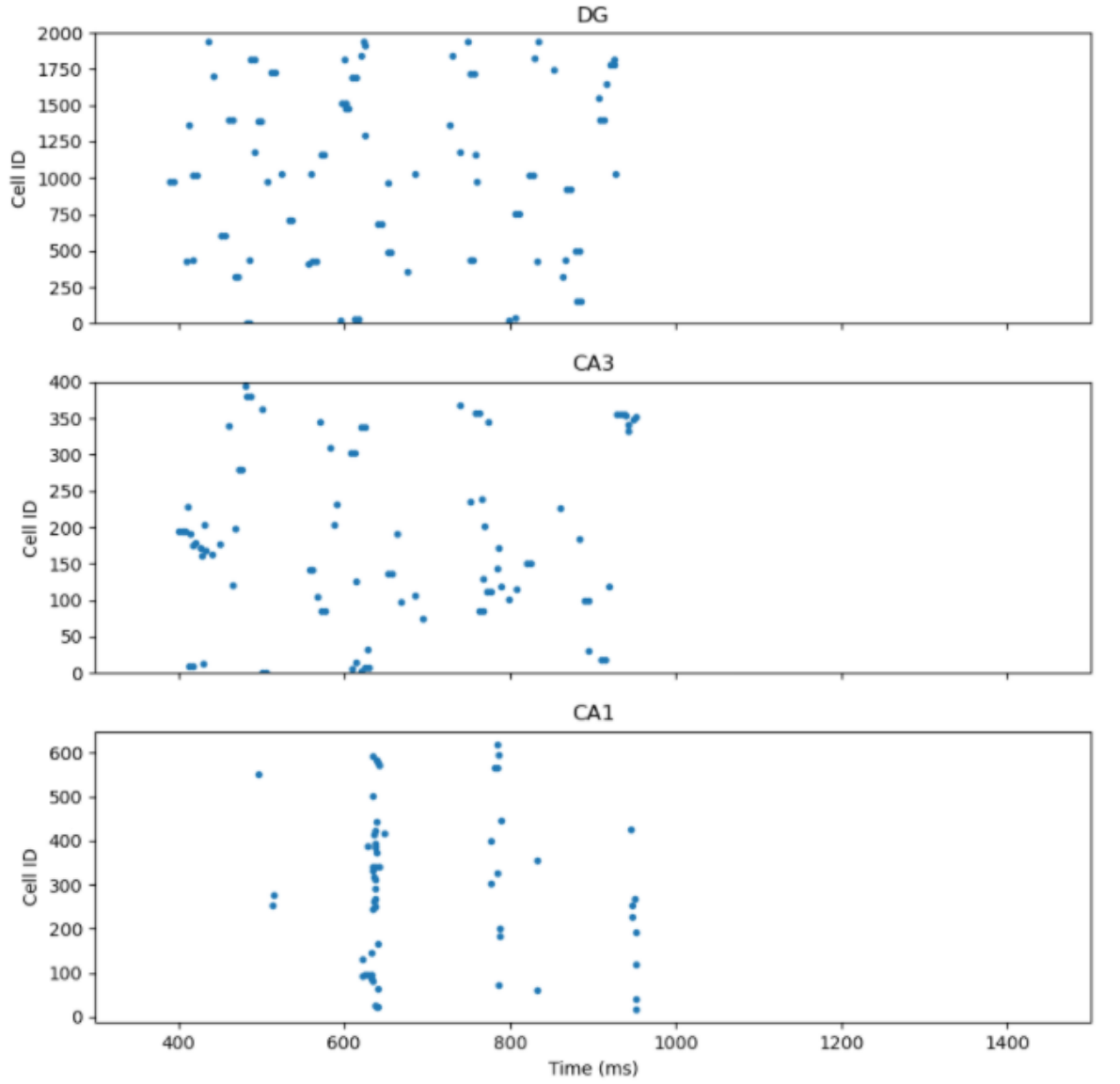

Figure 46. The activity of principal cells of our trisynaptic model. We observe theta oscillatory transformation of the sparse output from DG to a theta-like output from CA3 to theta oscillations from CA1. (Each dot represents an action potential from a single neuron; Theta oscillations: ~150 ms between the spikes)

4. Discussion

We presented a simplified yet biologically accurate model of the hippocampal circuitry consisting of three different subregions and multiple excitatory and inhibitory neuronal populations. All model features, ranging from single-cell electrophysiological properties to network connectivity patterns were constrained using a broad range of experimental data. For the principal neurons, we developed reduced compartmental neuron models with active dendrites, whereas INs were simulated as point neurons for the sake of simplicity. Apart from modeling the trisynaptic pathway, we also included 'non-canonical' synaptic pathways that have been generally overlooked by the majority of prior modeling studies. Furthermore, we modeled noise for the membrane potential to mimic the biological variability of the neurons.

Several hippocampal models are readily available in the literature. Some of them are quite abstract (e.g., rate models) and do not incorporate biophysical properties or dendrites (Neher et al., 2015; Pilly et al., 2018; Schapiro et al., 2017)Thus they are not suitable for studying how subcellular properties contribute to hippocampal memory functions. Conversely, other modeling approaches utilize models of higher biophysical complexity (Cutsuridis & Poirazi, 2015) however they are limited by their small network size and simplistic connectivity. In general, morphologically detailed models are impractical for large network simulations due to high computational cost Here comes our simplified, yet biological relevant, hippocampal network model, which can replicate biological behaviors from a single neuron to the whole network level, e.g., the F-I curve of the CA1 pyramidal cell and the pattern completion, respectively. By incorporating many passive properties of the neurons and dendritic mechanisms, we can study their role in the activity of the network. To summarize, our innovations were: 1) a data-driven approach that resulted in biological accurate single-cell properties, network connectivity, and network functions across three different hippocampal regions, 2) our principal neurons were modeled solely with phenomenological and event-driven mechanisms (not so detailed as Hodgkey and Huxley model), though they achieve high biological accuracy, and 3) we have a good balance between simulation performance and biological realism.

However, we have made abstractions, like not using many ion channels, e.g., CA^{2+} channels, and reduced population size, so we would have fewer free parameters to explore and validate, and our simulations could run faster without the need for high computational power. Nevertheless, we have the flexibility to add or remove specific neuronal/network parameters. Hence, we have built a hippocampal model that upon slight modifications, it can be used to answer various scientific questions. We have already proved that our model can replicate the pattern separation and pattern completion functions, so we set as our next goal to explore the role of dendritic mechanisms, i.e., Na^{+} and NMDA spikes, on signal integration from afferents and

efferents, and the effect of backpropagation of somatic action potentials. We can accomplish that by inhibiting one or both local spiking mechanisms, in one or multiple dendrites. Then, we wanted to assess how and which interneurons control and affect these behaviors. By removing the synapses of some interneuron groups to either other interneurons or principal cells, we could observe changes from a single neuron's membrane voltage to the whole network's firing rates.

It must be noted that our model comes with some limitations too. First, reduced compartmental models cannot compete with morphologically detailed models in terms of spatial resolution. More specifically, in detailed models, each dendrite consists of several segments used to ensure numerical simulation stability and allow more sophisticated and realistic synaptic placement. Second, the absence of biological information, such as different types of interneurons, may lead the experiments to miss unique behaviors. Another limitation comes straight from the neuronal model (CAdEx) we use, i.e., its loss of detailed biophysical explanations, like the description of a class of inactivating ionic channels (Górski et al., 2021).

With this work, we aim not only to inspire new hypotheses but also to provide the computational tools to explore them and promote the understanding of hippocampal memory processes. Some ideas for future research are the role of plasticity in DG and CA1 or the study of the mechanisms behind brain disorders. By introducing plasticity rules to GCs and CA1 pyramidal cells, our network model could predict their contribution to the pattern separation task and the formation of place cells, respectively. Additionally, we could explore epileptic behaviors by changing the connectivity between the neurons, the synaptic weights of specific pathways, or even the number of some neuronal populations. Moreover, as the technology evolves and the computational systems will be able to handle complex computations more efficiently, our model could be upgraded with larger neural populations, more types of interneurons, more dendritic compartments in the principal cells, or even to incorporate dendrites into the interneurons, leading to a more biologically relevant model.

5. References

Andersen, P., Morris, R., Amaral, D. (Eds.), & Bliss, T., & O'Keefe, J. (Ed.). (2007). The hippocampus book. Oxford University Press.

Amaral, D. G., Ishizuka, N., & Claiborne, B. (1990). Chapter 1 Chapter Neurons, numbers and the hippocampal network. In *Progress in Brain Research* (pp. 1–11). https://doi.org/10.1016/s0079-6123(08)61237-6

Amaral, D. G., Scharfman, H. E., & Lavenex, P. (2007). The dentate gyrus: fundamental neuroanatomical organization (dentate gyrus for dummies). *Progress in Brain Research*, *163*, 3–22.

Bassett, D. S., Cullen, K. E., Eickhoff, S. B., Farah, M. J., Goda, Y., Haggard, P., Hu, H., Hurd, Y. L., Josselyn, S. A., Khakh, B. S., Knoblich, J. A., Poirazi, P., Poldrack, R. A., Prinz, M., Roelfsema, P. R., Spires-Jones, T. L., Sur, M., & Ueda, H. R. (2020). Reflections on the past two decades of neuroscience. *Nature Reviews. Neuroscience*, *21*(10), 524–534.

Basu, J., & Siegelbaum, S. A. (2015). The Corticohippocampal Circuit, Synaptic Plasticity, and Memory. *Cold Spring Harbor Perspectives in Biology*, *7*(11). https://doi.org/10.1101/cshperspect.a021733

Becker, D., Willems, L. M., Vnencak, M., Zahn, N., Schuldt, G., Jedlicka, P., Maggio, N., Deller, T., & Vlachos, A. (2012). Functional and structural properties of dentate granule cells with hilar basal dendrites in mouse entorhino-hippocampal slice cultures. *PloS One*, *7*(11), e48500.

Benavides-Piccione, R., Regalado-Reyes, M., Fernaud-Espinosa, I., Kastanauskaite, A., Tapia-González, S., León-Espinosa, G., Rojo, C., Insausti, R., Segev, I., & DeFelipe, J. (2020). Differential Structure of Hippocampal CA1 Pyramidal

Neurons in the Human and Mouse. *Cerebral Cortex* , *30*(2), 730–752.

Bezaire, M. J., Raikov, I., Burk, K., Vyas, D., & Soltesz, I. (2016). Interneuronal mechanisms of hippocampal theta oscillations in a full-scale model of the rodent CA1 circuit. *eLife*, *5*. https://doi.org/10.7554/eLife.18566

Bezaire, M. J., & Soltesz, I. (2013). Quantitative assessment of CA1 local circuits: knowledge base for interneuron-pyramidal cell connectivity. *Hippocampus*, *23*(9), 751–785.

Bienkowski, M. S., Sepehrband, F., Kurniawan, N. D., Stanis, J., Korobkova, L., Khanjani, N., Clark, K., Hintiryan, H., Miller, C. A., & Dong, H. W. (2021). Homologous laminar organization of the mouse and human subiculum. Scientific reports, 11(1), 3729. https://doi.org/10.1038/s41598-021-81362-w

Bliss, T. V., & Lomo, T. (1973). Long-lasting potentiation of synaptic transmission in the dentate area of the anaesthetized rabbit following stimulation of the perforant path. *The Journal of Physiology*, *232*(2), 331–356.

Bono, J., & Clopath, C. (2017). Modeling somatic and dendritic spike mediated plasticity at the single neuron and network level. *Nature Communications*, *8*(1), 706.

Booker, S. A., & Vida, I. (2018). Morphological diversity and connectivity of hippocampal interneurons. *Cell and Tissue Research*, *373*(3), 619–641.

Brette, R., & Gerstner, W. (2005). Adaptive exponential integrate-and-fire model as an effective description of neuronal activity. *Journal of Neurophysiology*, *94*(5), 3637–3642.

Buckmaster, P. S., & Jongen-Rêlo, A. L. (1999). Highly specific neuron loss preserves lateral inhibitory circuits in the dentate gyrus of kainate-induced epileptic rats. *The Journal of Neuroscience: The Official Journal of the Society*

for Neuroscience, *19*(21), 9519–9529.

Buzsáki, G. (2002). Theta Oscillations in the Hippocampus. In *Neuron* (Vol. 33, Issue 3, pp. 325–340). https://doi.org/10.1016/s0896-6273(02)00586-x

Chavlis, S., Petrantonakis, P. C., & Poirazi, P. (2017). Dendrites of dentate gyrus granule cells contribute to pattern separation by controlling sparsity. *Hippocampus*, *27*(1), 89–110.

Christian, K. M., Ming, G.-L., & Song, H. (2020). Adult neurogenesis and the dentate gyrus: Predicting function from form. *Behavioural Brain Research*, *379*, 112346.

Claiborne, B. J., Amaral, D. G., & Maxwell Cowan, W. (1990). Quantitative, three-dimensional analysis of granule cell dendrites in the rat dentate gyrus. In *The Journal of Comparative Neurology* (Vol. 302, Issue 2, pp. 206–219). https://doi.org/10.1002/cne.903020203

Coultrip, R., Granger, R., & Lynch, G. (1992). A cortical model of winner-take-all competition via lateral inhibition. In *Neural Networks* (Vol. 5, Issue 1, pp. 47–54). https://doi.org/10.1016/s0893-6080(05)80006-1

Cutsuridis, V., Graham, B., Cobb, S., & Vida, I. (2010). *Hippocampal Microcircuits: A Computational Modeler's Resource Book*. Springer Science & Business Media.

Cutsuridis, V., & Poirazi, P. (2015). A computational study on how theta modulated inhibition can account for the long temporal windows in the entorhinal-hippocampal loop. *Neurobiology of Learning and Memory*, *120*, 69–83.

Drew, L. J., Kheirbek, M. A., Luna, V. M., Denny, C. A., Cloidt, M. A., Wu, M. V., Jain, S., Scharfman, H. E., & Hen, R. (2016). Activation of local inhibitory circuits in the dentate gyrus by adult-born neurons. *Hippocampus*, *26*(6), 763–778.

Dyhrfjeld-Johnsen, J., Santhakumar, V., Morgan, R. J., Huerta, R., Tsimring, L., &

Soltesz, I. (2007). Topological determinants of epileptogenesis in large-scale structural and functional models of the dentate gyrus derived from experimental data. *Journal of Neurophysiology*, *97*(2), 1566–1587.

Ermentrout G.B., Terman D.H. (2010) Dendrites. In: Mathematical Foundations of Neuroscience. Interdisciplinary Applied Mathematics, vol 35. Springer, New York, NY. https://doi.org/10.1007/978-0-387-87708-2_2

Francavilla, R., Guet-McCreight, A., Amalyan, S., Hui, C. W., Topolnik, D., Michaud, F., Marino, B., Tremblay, M.-È., Skinner, F. K., & Topolnik, L. (2020). Alterations in Intrinsic and Synaptic Properties of Hippocampal CA1 VIP Interneurons During Aging. *Frontiers in Cellular Neuroscience*, *14*, 554405.

Freund, T. and Buzsáki, G. (1996), Interneurons of the hippocampus. Hippocampus, 6: 347-470. https://doi.org/10.1002/(SICI)1098-1063(1996)6:4<347::AID-HIPO1>3.0.CO;2-I

Gloveli, T., Dugladze, T., Saha, S., Monyer, H., Heinemann, U., Traub, R. D., Whittington, M. A., & Buhl, E. H. (2005). Differential involvement of oriens/pyramidale interneurones in hippocampal network oscillations in vitro. *The Journal of Physiology*, *562*(Pt 1), 131–147.

Górski, T., Depannemaecker, D., & Destexhe, A. (2021). Conductance-Based Adaptive Exponential Integrate-and-Fire Model. *Neural Computation*, *33*(1), 41–66.

Gould, E., Woolley, C. S., Frankfurt, M., & McEwen, B. S. (1990). Gonadal steroids regulate dendritic spine density in hippocampal pyramidal cells in adulthood. The Journal of neuroscience: the official journal of the Society for Neuroscience, 10(4), 1286–1291. https://doi.org/10.1523/JNEUROSCI.10-04-01286.1990

Hafting, T., Fyhn, M., Molden, S., Moser, M.-B., & Moser, E. I. (2005). Microstructure

of a spatial map in the entorhinal cortex. *Nature*, *436*(7052), 801–806.

Harnett, M. T., Makara, J. K., Spruston, N., Kath, W. L., & Magee, J. C. (2012). Synaptic amplification by dendritic spines enhances input cooperativity. *Nature*, *491*(7425), 599–602.

Hedrick, T. P., Nobis, W. P., Foote, K. M., Ishii, T., Chetkovich, D. M., & Swanson, G. T. (2017). Excitatory Synaptic Input to Hilar Mossy Cells under Basal and Hyperexcitable Conditions. *eNeuro*, *4*(6). https://doi.org/10.1523/ENEURO.0364-17.2017

Hilscher, M. M., Nogueira, I., Mikulovic, S., Kullander, K., Leão, R. N., & Leão, K. E. (2019). Chrna2-OLM interneurons display different membrane properties and h-current magnitude depending on dorsoventral location. *Hippocampus*, *29*(12), 1224–1237.

Hodgkin, A. L., & Huxley, A. F. (1952). A quantitative description of membrane current and its application to conduction and excitation in nerve. The Journal of Physiology, 117(4), 500–544. https://doi.org/10.1113/jphysiol.1952.sp004764

Honoré, E., Khlaifia, A., Bosson, A., & Lacaille, J.-C. (2021). Hippocampal Somatostatin Interneurons, Long-Term Synaptic Plasticity and Memory. *Frontiers in Neural Circuits*, *15*, 687558.

Hosseini-Sharifabad, M., & Nyengaard, J. R. (2007). Design-based estimation of neuronal number and individual neuronal volume in the rat hippocampus. *Journal of Neuroscience Methods*, *162*(1-2), 206–214.

Humphries, R., Mellor, J. R., & O'Donnell, C. (2021). Acetylcholine Boosts Dendritic NMDA Spikes in a CA3 Pyramidal Neuron Model. Neuroscience, S0306-4522(21)00574-1. Advance online publication. https://doi.org/10.1016/j.neuroscience.2021.11.014

Johnston, D., Magee, J. C., Colbert, C. M., & Cristie, B. R. (1996). Active properties of neuronal dendrites. Annual review of neuroscience, 19, 165–186. https://doi.org/10.1146/annurev.ne.19.030196.001121

Kaifosh, P., & Losonczy, A. (2016). Mnemonic Functions for Nonlinear Dendritic Integration in Hippocampal Pyramidal Circuits. *Neuron*, *90*(3), 622–634.

Kassab, R., & Alexandre, F. (2018). Pattern separation in the hippocampus: distinct circuits under different conditions. *Brain Structure & Function*, *223*(6), 2785–2808.

Kastellakis, G., Cai, D. J., Mednick, S. C., Silva, A. J., & Poirazi, P. (2015). Synaptic clustering within dendrites: an emerging theory of memory formation. *Progress in Neurobiology*, *126*, 19–35.

Kelly, T., & Beck, H. (2017). Functional properties of granule cells with hilar basal dendrites in the epileptic dentate gyrus. *Epilepsia*, *58*(1), 160–171.

Kim, S., Guzman, S. J., Hu, H., & Jonas, P. (2012). Active dendrites support efficient initiation of dendritic spikes in hippocampal CA3 pyramidal neurons. *Nature Neuroscience*, *15*(4), 600–606.

Kim, S., Kim, Y., Lee, S.-H., & Ho, W.-K. (2018). Dendritic spikes in hippocampal granule cells are necessary for long-term potentiation at the perforant path synapse. *eLife*, *7*. https://doi.org/10.7554/eLife.35269

Kowalski, J., Gan, J., Jonas, P., & Pernía-Andrade, A. J. (2016). Intrinsic membrane properties determine hippocampal differential firing pattern in vivo in anesthetized rats. Hippocampus, 26(5), 668–682. https://doi.org/10.1002/hipo.22550

Kraushaar, U., & Jonas, P. (2000). Efficacy and Stability of Quantal GABA Release at a Hippocampal Interneuron–Principal Neuron Synapse. In *The Journal of*

Neuroscience (Vol. 20, Issue 15, pp. 5594–5607). https://doi.org/10.1523/jneurosci.20-15-05594.2000

Krueppel, R., Remy, S., & Beck, H. (2011). Dendritic Integration in Hippocampal Dentate Granule Cells. In *Neuron* (Vol. 71, Issue 3, pp. 512–528). https://doi.org/10.1016/j.neuron.2011.05.043

Lee, H., Wang, C., Deshmukh, S. S., & Knierim, J. J. (2015). Neural Population Evidence of Functional Heterogeneity along the CA3 Transverse Axis: Pattern Completion versus Pattern Separation. *Neuron*, *87*(5), 1093–1105.

Leung, L. S., Roth, L., & Canning, K. J. (1995). Entorhinal inputs to hippocampal CA1 and dentate gyrus in the rat: a current-source-density study. Journal of Neurophysiology, 73(6), 2392–2403. https://doi.org/10.1152/jn.1995.73.6.2392

López-Madrona, V. J., & Canals, S. (2021). Functional Interactions between Entorhinal Cortical Pathways Modulate Theta Activity in the Hippocampus. *Biology*, *10*(8). https://doi.org/10.3390/biology10080692

Lübke, J., Frotscher, M., & Spruston, N. (1998). Specialized Electrophysiological Properties of Anatomically Identified Neurons in the Hilar Region of the Rat Fascia Dentata. In *Journal of Neurophysiology* (Vol. 79, Issue 3, pp. 1518–1534). https://doi.org/10.1152/jn.1998.79.3.1518

Maccaferri, G. (2005). Stratum oriens horizontal interneurone diversity and hippocampal network dynamics. *The Journal of Physiology*, *562*(Pt 1), 73–80.

Malezieux, M., Kees, A. L., & Mulle, C. (2020). Theta Oscillations Coincide with Sustained Hyperpolarization in CA3 Pyramidal Cells, Underlying Decreased Firing. *Cell Reports*, *32*(1), 107868.

Mao, D., Kandler, S., McNaughton, B. L., & Bonin, V. (2017). Sparse orthogonal population representation of spatial context in the retrosplenial cortex. *Nature*

Communications, *8*(1), 243.

Masurkar, A. V., Tian, C., Warren, R., Reyes, I., Lowes, D. C., Brann, D. H., & Siegelbaum, S. A. (2020). Postsynaptic integrative properties of dorsal CA1 pyramidal neuron subpopulations. *Journal of Neurophysiology*, *123*(3), 980–992.

McNaughton BL, Barnes CA, Mizumori SJY, Green EJ, Sharp PE. 1991. Contribution of granule cells to spatial representations in hippocampal circuits: A puzzle In: Morrell F, editor. Kindling and Synaptic Plasticity: The Legacy of Graham Goddar. Boston: Springer-Verlag; pp 110–123.

Mishra, P., & Narayanan, R. (2020). Heterogeneities in intrinsic excitability and frequency-dependent response properties of granule cells across the blades of the rat dentate gyrus. *Journal of Neurophysiology*, *123*(2), 755–772.

Mishra, R. K., Kim, S., Guzman, S. J., & Jonas, P. (2016). Symmetric spike timing-dependent plasticity at CA3-CA3 synapses optimizes storage and recall in autoassociative networks. *Nature Communications*, *7*, 11552.

Morgan, R. J., Santhakumar, V., & Soltesz, I. (2007). Modeling the dentate gyrus. *Progress in Brain Research*, *163*, 639–658.

Myers, C. E., & Scharfman, H. E. (2009). A role for hilar cells in pattern separation in the dentate gyrus: a computational approach. *Hippocampus*, *19*(4), 321–337.

Myers, C. E., & Scharfman, H. E. (2011). Pattern separation in the dentate gyrus: a role for the CA3 backprojection. *Hippocampus*, *21*(11), 1190–1215.

Neher, T., Cheng, S., & Wiskott, L. (2015). Memory storage fidelity in the hippocampal circuit: the role of subregions and input statistics. *PLoS Computational Biology*, *11*(5), e1004250.

O'Keefe, J., & Dostrovsky, J. (1971). The hippocampus as a spatial map. Preliminary evidence from unit activity in the freely-moving rat. *Brain Research*, *34*(1),

171–175.

Oulé, M., Atucha, E., Wells, T. M., Macharadze, T., Sauvage, M. M., Kreutz, M. R., & Lopez-Rojas, J. (2021). Dendritic Kv4.2 potassium channels selectively mediate spatial pattern separation in the dentate gyrus. *iScience*, *24*(8), 102876.

Owen, B., Bichler, E., & Benveniste, M. (2021). Excitatory synaptic transmission in hippocampal area CA1 is enhanced then reduced as chronic epilepsy progresses. *Neurobiology of Disease*, *154*, 105343.

Papoutsi, A., Kastellakis, G., Psarrou, M., Anastasakis, S., & Poirazi, P. (2014). Coding and decoding with dendrites. *Journal of Physiology, Paris*, *108*(1), 18–27.

Papoutsi, A., Sidiropoulou, K., & Poirazi, P. (2014). Dendritic Nonlinearities Reduce Network Size Requirements and Mediate ON and OFF States of Persistent Activity in a PFC Microcircuit Model. In *PLoS Computational Biology* (Vol. 10, Issue 7, p. e1003764). https://doi.org/10.1371/journal.pcbi.1003764

Papp, O. I., Karlócai, M. R., Tóth, I. E., Freund, T. F., & Hájos, N. (2013). Different input and output properties characterize parvalbumin-positive basket and Axo-axonic cells in the hippocampal CA3 subfield. *Hippocampus*, *23*(10), 903–918.

Pilly, P. K., Howard, M. D., & Bhattacharyya, R. (2018). Modeling Contextual Modulation of Memory Associations in the Hippocampus. *Frontiers in Human Neuroscience*, *12*, 442.

Poirazi, P., & Papoutsi, A. (2020). Illuminating dendritic function with computational models. Nature reviews. Neuroscience, 21(6), 303–321. https://doi.org/10.1038/s41583-020-0301-7

Rall, W. (1957). Membrane time constant of motoneurons. Science, 126(3271), 454.

https://doi.org/10.1126/science.126.3271.454

Rebola, N., Carta, M., & Mulle, C. (2017). Operation and plasticity of hippocampal CA3 circuits: implications for memory encoding. *Nature Reviews. Neuroscience*, *18*(4), 208–220.

Robert, B. J. A., Moreau, M. M., Dos Santos Carvalho, S., Barthet, G., Racca, C., Bhouri, M., Quiedeville, A., Garret, M., Atchama, B., Al Abed, A. S., Guette, C., Henderson, D. J., Desmedt, A., Mulle, C., Marighetto, A., Montcouquiol, M., & Sans, N. (2020). Vangl2 in the Dentate Network Modulates Pattern Separation and Pattern Completion. *Cell Reports*, *31*(10), 107743.

Savanthrapadian, S., Meyer, T., Elgueta, C., Booker, S. A., Vida, I., & Bartos, M. (2014). Synaptic properties of SOM- and CCK-expressing cells in dentate gyrus interneuron networks. *The Journal of Neuroscience: The Official Journal of the Society for Neuroscience*, *34*(24), 8197–8209.

Schapiro, A. C., Turk-Browne, N. B., Botvinick, M. M., & Norman, K. A. (2017). Complementary learning systems within the hippocampus: a neural network modelling approach to reconciling episodic memory with statistical learning. *Philosophical Transactions of the Royal Society of London. Series B, Biological Sciences*, *372*(1711). https://doi.org/10.1098/rstb.2016.0049

Scharfman, H. E. (2016). The enigmatic mossy cell of the dentate gyrus. *Nature Reviews. Neuroscience*, *17*(9), 562–575.

Scoville, W. B., & Milner, B. (1957). Loss of recent memory after bilateral hippocampal lesions. *Journal of Neurology, Neurosurgery, and Psychiatry*, *20*(1), 11–21.

Seress, L., & Mrzljak, L. (1987). Basal dendrites of granule cells are normal features of the fetal and adult dentate gyrus of both monkey and human hippocampal

formations. *Brain Research*, *405*(1), 169–174.

Seress, L., & Ribak, C. E. (1990). The synaptic connections of basket cell axons in the developing rat hippocampal formation. *Experimental Brain Research. Experimentelle Hirnforschung. Experimentation Cerebrale*, *81*(3), 500–508.

Sloviter, R. S., & Lømo, T. (2012). Updating the lamellar hypothesis of hippocampal organization. *Frontiers in Neural Circuits*, *6*, 102.

Spruston, N., Stuart, G., & Häusser, M. (2016-03-01). Principles of dendritic integration. In Dendrites.: Oxford University Press. Retrieved 16 Feb. 2022, from https://oxford.universitypressscholarship.com/view/10.1093/acprof:oso/9780198745273.001.0001/acprof-9780198745273-chapter-12.

Stimberg, M., Brette, R., & Goodman, D. F. (2019). Brian 2, an intuitive and efficient neural simulator. *eLife*, *8*. https://doi.org/10.7554/eLife.47314

Stuart, G. J., & Spruston, N. (2015). Dendritic integration: 60 years of progress. Nature neuroscience, 18(12), 1713–1721. https://doi.org/10.1038/nn.4157

Sun, Q., Sotayo, A., Cazzulino, A. S., Snyder, A. M., Denny, C. A., & Siegelbaum, S. A. (2017). Proximodistal Heterogeneity of Hippocampal CA3 Pyramidal Neuron Intrinsic Properties, Connectivity, and Reactivation during Memory Recall. *Neuron*, *95*(3), 656–672.e3.

Treves, A., Tashiro, A., Witter, M. P., & Moser, E. I. (2008). What is the mammalian dentate gyrus good for? In *Neuroscience* (Vol. 154, Issue 4, pp. 1155–1172). https://doi.org/10.1016/j.neuroscience.2008.04.073

Vida, I., Bartos, M., & Jonas, P. (2006). Shunting inhibition improves robustness of gamma oscillations in hippocampal interneuron networks by homogenizing firing rates. *Neuron*, *49*(1), 107–117.

Vida, I., Degro, C. E., & Booker, S. A. (2018). Morphology of Hippocampal Neurons.

In *Springer Series in Computational Neuroscience* (pp. 29–90). https://doi.org/10.1007/978-3-319-99103-0_2

West, M. J., Slomianka, L., & Gundersen, H. J. (1991). Unbiased stereological estimation of the total number of neurons in the subdivisions of the rat hippocampus using the optical fractionator. *The Anatomical Record*, *231*(4), 482–497.

Xu, X., Sun, Y., Holmes, T. C., & López, A. J. (2016). Noncanonical connections between the subiculum and hippocampal CA1. *The Journal of Comparative Neurology*, *524*(17), 3666–3673.

Yang, S., Yang, S., Moreira, T., Hoffman, G., Carlson, G. C., Bender, K. J., Alger, B. E., & Tang, C.-M. (2014). Interlamellar CA1 network in the hippocampus. *Proceedings of the National Academy of Sciences of the United States of America*, *111*(35), 12919–12924.

Yassa, M. A., & Stark, C. E. (2011). Pattern separation in the hippocampus. Trends in neurosciences, 34(10), 515–525. https://doi.org/10.1016/j.tins.2011.06.006

Yuan, M., Meyer, T., Benkowitz, C., Savanthrapadian, S., Ansel-Bollepalli, L., Foggetti, A., Wulff, P., Alcami, P., Elgueta, C., & Bartos, M. (2017). Somatostatin-positive interneurons in the dentate gyrus of mice provide local- and long-range septal synaptic inhibition. *eLife*, *6*. https://doi.org/10.7554/eLife.21105